Optimizing Tracking Windows Timing for Improved Cislunar Inter-Satellite Autonomous Navigation

Thesis Report

Graduation Thesis

Thomas Bosboom

Delft University of Technology

TU Delft

This page is left blank intentionally.

Optimizing Tracking Windows Timing for Improved Cislunar Inter-Satellite Autonomous Navigation

Thesis Report

by

Thomas Bosboom

In partial fulfillment of the requirements for the degree of

Master of Science
in Aerospace Engineering
at Delft University of Technology

Student number:	4787196	
Project duration:	09-2023 until 10-2024	
Thesis committee:	Prof. Dr. ir. S. Gehly:	TU Delft, Examiner
	Prof. Dr. ir. J. Bouwmeester:	TU Delft, Chair
Supervisors	Prof. Dr. ir. S. Speretta:	TU Delft, daily supervisor
	Dr. ir. E. Turan:	TU Delft, daily supervisor

An electronic version of this thesis is available at `http://repository.tudelft.nl/`.
For reproducibility purposes, please visit: `https://github.com/ThomasBosboom/ThesisSpace`

Cover image: courtesy Bill Anders.

TU Delft

Preface

The field of autonomous navigation has seen significant developments in recent years, driven by the growing demand for innovative technological solutions in the growing smallsat market in combination with the future lunar economy. In this context, my research work aims to address some of the critical challenges faced in this field. In this report, I provide insights into the theoretical and practical aspects of my research, including an overview of the study design, methodology and analysis of a special subset or lunar orbiters that are familiar to previous work performed by my supervisors. The report also presents a detailed discussion of the findings to interpret the benefits and limitations of the work. I hope that this report is a useful resource for future students or any other person who is working in this field.

This thesis report represents the culmination of my studies at Delft University of Technology. As a graduate student, I have been fortunate to work with experts in the field and to have access to exceptional resources at the university. First and foremost, I would like to thank my two very kind supervisors Stefano Speretta and Erdem Turan. Their patience and understanding of my thesis-related struggles have been very helpful in my success in this endeavor. Last but not least I would like to thank friends and family for their support during the year that I spent working on this work.

Thomas Bosboom
Delft, October 2024

Contents

List of Symbols

Symbol	Definition	Unit
A	Effective spacecraft area	$[m^2]$
$A(t)$	Linear dynamics matrix	$[-]$
c	Speed of light	$[m/s]$
C_R	Spacecraft reflectivity	$[-]$
C_j	Jacobi constant	$[-]$
$\boldsymbol{b}_i$	Position deviation from target point i	$[-]$
$\boldsymbol{f}$	(Non)-linear dynamics function	$[-]$
$\boldsymbol{h}$	(Non)-linear measurement function	$[-]$
$\tilde{\boldsymbol{H}}$	Measurement Jacobian	$[-]$
i	Measurement i in a batch fit span	$[-]$
k	Measurement batch number k	$[-]$
L_s	Luminosity of the Sun	$[W]$
m	Mass of a satellite or celestial body	$[kg]$
$\boldsymbol{N}$	Information state vector	$[-]$
$\boldsymbol{N}_{pt}$	Number of target points	$[-]$
$\boldsymbol{P}$	State error covariance matrix	$[-]$
$P_{n,m}(x)$	Lagrange polynomial of order n and degree m	$[-]$
$\boldsymbol{Q}$	Station keeping cost weighing matrix	$[-]$
R	Reference radius	$[m]$
$\boldsymbol{R}$	Measurement noise covariance matrix	$[-]$
$\boldsymbol{R}_i$	Station keeping weighing matrix of target point i	$[-]$
$\boldsymbol{r}$	Position vector	$[m]$
S	Measurement sensitivity	$[-]$
t_c	Cut-off epoch	$[s]$
t_i	Target point epoch or measurement epoch	$[s]$
t_v	Correction epoch	$[s]$
U	Gravitational potential	$[J/kg]$
$\boldsymbol{v}$	Velocity vector	$[m]$
$\Delta\boldsymbol{V}$	Orbit correction cost	$[m/s]$
$\boldsymbol{W}$	Measurement weighing matrix	$[-]$
$\boldsymbol{x}$	State vector	$[-]$
$\Delta\boldsymbol{x}$	State deviation vector	$[-]$
$\Delta\boldsymbol{y}$	Measurement deviation vector	$[-]$
λ	Eigenvalue	$[-]$
Λ	Geographic longitude	$[rad]$
μ	Standard gravitational parameter of a body	$[m^3 s^{-2}]$
ρ	Range observable	$[m]$
$\boldsymbol{\Lambda}$	Information matrix	$[-]$
$\boldsymbol{\Phi}$	State transition matrix	$[-]$
ϕ	Geocentric latitude	$[rad]$
σ	Standard deviation	$[-]$

Acronym	Meaning
(A)OD	(Autonomous) Orbit Determination
BLS	Batch Least Squares
BFP	Bicircular Four-body Problem
COTS	Commercially-Of-The-Shelf
CRTBP	Circular Restricted Three-Body Problem
DNS	Deep Space Network
DTE	Direct-to-Earth connection
ECI	Earth-Centered Inertial
EKF	Extended Kalman Filter
EM	Earth-Moon
ELO	Elliptical Lunar Orbit
EOM	Equation Of Motion
EPS	Electrical Power System
ERTBP	Elliptical Restricted Three-Body Problem
ESA	European Space Agency
FF	Full Fidelity
DAGDOP	Dynamic And Geometric Dilution Of Precision
GNSS	Global Navigation Satellite System
HF	High Fidelity
IAU	International Astronomical Union
ISL	Inter-Satellite Link
LF	Low Fidelity
LOS	Line-Of-Sight
LPO	Lagrange Point Orbit
LPF	Lunar Pathfinder
LSA	Lunar Surface Assets
LUMIO	Lunar Meteoroid Impact Observer
LiAISON	Linked Autonomous Interplanetary Satellite Orbit Navigation
MC	Monte Carlo
MJD	Modified Julian Date
NAIF	Navigation and Ancillary Information Facility
NRHO	Near Rectilinear Halo Orbit
OBC	On-Board Computer
ODE	Ordinary Differential Equation
OI	Orbit Insertion
PN	Pseudo Noise
PM	Point Mass
PSO	Particle Swarm Optimization
RSME	Root Mean Squared Error
RSS	Root Sum Squared
S/C	Spacecraft
S/K	Station-keeping
SSTL	Surrey Satellite Technology Ltd.
SH	Spherical Harmonics
SKM	Station-Keeping Maneuver
SPICE	Spacecraft Planet Instrument C-matrix Events
SST	Satellite-to-Satellite Tracking
STM	State Transition Matrix
SRP	Solar Radiation Pressure
TUDAT	TU Delft Astrodynamics Toolbox
TPM	Target Point Method
UHF	Ultra High Frequency

List of Figures

List of Tables

Summary

With the projected expansion of the small satellite market and the rise of the lunar economy, the development of cost efficient and reliable navigation in cislunar space—defined as the region of space between Earth and Moon including the region around the surface of the Moon—has become increasingly important. However, the increase in the number of satellites is a stressing factor on the existing communication networks in terms of availability, which exerts pressure on orbit determination quality and the financial budget of a small satellite mission. One way to release the pressure from the existing ground station communications is through the concept of Autonomous Orbit Determination (AOD). Specifically, state estimation is done through the use of inter-satellite radio links between at least two satellites of which one orbit has a unique size, shape, and orientation for sufficient observability in the estimation process. This occurs strongly for certain regions in the three-body problem, in particular Lagrange-point orbits, which makes cislunar space-the most common region for small satellite deep space missions-an ideal environment to perform AOD in. With the aid of state estimates from the AOD process, a spacecraft can also autonomously navigate itself towards its pre-defined target orbit, defined by station keeping maneuvers. The topic of inter-satellite based OD and the topic of orbit navigation has previously been studied extensively in literature but has thus-far covered the two topics separately. Previous literature also has not clearly linked AOD with mission and spacecraft design related parameters, and is primarily focused on the orbit estimation aspect rather than including navigation as well. This thesis aims to combine these knowledge gaps, by researching the potential of improving cislunar missions using autonomous navigation by exploring the strategic adjustment of the timing of inter-satellite tracking sessions by optimizing for annual station keeping cost of a satellite, defined in ΔV. Since the accuracy of the maneuvers relies on the magnitude of estimation errors from the OD process, which in turn depends on the state observability during a tracking arc, solving for lowest ΔV is a complex optimization problem.

Methodology

The analysis of this work is based on a case study in which an L_2 Lagrange point orbiter (LPO), called LUMIO, and an elliptical lunar orbiter (ELO), called LPF (based on the SSTL Lunar Pathfinder), perform AOD based on two-way inter-satellite ranging with a Gaussian noise level of 2.98m 1σ, observed at a 300 s interval. The choice for this particular constellation is based on the notion that an orbit with a small period bodes well in terms of observational geometry when combined with a Lagrange point orbit, leading to good state observability. The orbit corrections are assumed to occur at the end of an estimation arc that uses the Batch-Least Squares estimator with no observation bias or dynamic model errors. The goal of this study is to reduce ΔV for the planned 1-year operational lifetime of LUMIO. An initial tracking window configuration is defined as a set of tracking arcs with a length of 1 day combined with a 3-day interval between each arc, which equates to a station keeping frequency of 4 days. The simulation starts at MJD60390 and runs for 28 days. The choice for this timing configuration is based on a suggestion in literature which states that performing 3 to 4 corrections per orbital period is the best for ΔV in LPOs. A simulation of 28 days instead of 365 days is chosen due to memory and run time limitations. The 28-day duration covers two full LUMIO orbital periods which was deemed sufficient to represent costs for the full mission duration. In order to remove effects coming from orbit insertion and to have a stable nominal navigation scenario, only the corrections after 14 days since the mission start epoch are counted towards the annual cost approximation. Costs are of a stochastic nature due to varying measurement noise histories in the estimation process, so ΔV is always based on 10 Monte Carlo runs of the orbit estimation and navigation process. This scenario forms the baseline for a comparative analysis on observation windows and other model settings to evaluate the influence of those parameters.

Main findings

First, a choice was made on the on-board dynamic model that is used to simulate the trajectory of the spacecraft. A point mass model of the Earth, Moon and Sun plus cannonball solar radiation pressure, named PMSRP01, proved to be the best environment setup due to its best combination of short run time and relatively close alignment with the reference orbit, or dispersion, that is provided by the LUMIO team at Politecnico di

Milano. The total time to calculate a maneuver-using the Target Point Method with one target point of 3 days downstream with LUMIO's current on-board computer-equated to approximately 528s. This is small compared to the orbital period of LUMIO, tracking arc or the cut-off duration of 12h that is currently considered for LUMIO. The total run time value shows that this 12h time window is not required in the context of AOD, making corrections potentially more accurate due to small correction delays. Point mass (PM) and spherical harmonics (SH) models showed a 14-day RMSE position dispersion around $1 \cdot 10^5$ m, and adding SRP reduced this to around $8 \cdot 10^3$ m. This shows that adding SRP is more relevant than using more complex gravity models. In terms of design considerations, it shows that the on-board processor itself will not be a limitation for performing the calculations associated with AOD and thus no design change has to be made in this regard.

The baseline configuration yields an annual ΔV of 0.613$\pm$0.0066 1σ m/s. Next, a comparative analysis explored timing configurations of constant tracking arc intervals and arc durations, ranging between 0.1-4.0 days and 0.1-2.0 days, respectively. Of these configurations, the best option is a configuration with an arc duration of 0.5 day and a 0.5 day interval between the arcs, yielding an annual ΔV of 0.375$\pm$0.0020 1σ m/s or a reduction of 38.597$\pm$0.228 1σ % with respect to the baseline scenario. Orbit-specific tracking schemes were also tested, based on the knowledge that faster (perilune) and slower (apolune) dynamics can influence the observability of position or velocity states during the estimation process. Tracking specifically at one of these two regions did show improvements over the baseline configuration but not over the best result of the constant arc category. The best annual ΔV yields 0.498$\pm$0.0082 1σ m/s (18.760$\pm$1.337 1σ %) for apolune and 0.505$\pm$0.0124 1σ m/s (17.618$\pm$2.023 1σ %) for perilune. Both have a tracking time of 0.15 days, but the best for perilune is for a scheme that tracks every 6 passes and every 4 for the apolune case. The short total tracking times is a beneficial aspect of the orbit-based solution.

Then, a sensitivity analysis was done on two categories of parameters: observation window settings and auxiliary settings. The former refers to the parameters that define the structure of the tracking timing and the latter refers to other parameters that are used in the simulation that might affect the ΔV outcome. In each sensitivity case, only one parameter is varied, with the rest of the settings, as shown in Appendix A, held constant. Firstly, there is a strong trend that shows that a shorter arc interval yields lower costs with means ranging from 0.4518 to 0.9784 m/s in the range of 1.0-4.0 days. For different arc durations (0.1-2.0 days), using a duration of 0.5 days proved to be best in combination with the default interval of 3 days at 0.5290 m/s. Results show that annual ΔV can be sensitive to the mission start epoch (varied MJD60390 to MJD60405), suggesting that the cost results vary slightly depending on when the simulation starts. However, the variation in the sensitivity cases is three times smaller than the variation due to the choice of tracking arcs and intervals (0.1117 m/s versus 0.339 m/s and 0.5274 m/s respectively). A similar analysis over a longer simulation duration of 56 days showed that the dependency of start epoch is even smaller, which indicates that the ΔV results from the analysis is likely similar in scenarios in which LUMIO is inserted in its operational orbit later. Regarding the auxiliary parameters, the largest sensitivity comes from the choice of the minimal ΔV threshold, indicating that the ΔV specifications of a propulsion subsystem could have a drastic influence in the cost budget. Next to this, the choice of target points is also important. These target points represent how many days the correction algorithm aims in the future to target the reference trajectory. Aiming too short or too far downstream might lead to exhaustive overcompensation if a next correction aims too far away from the next correction point. While 3 days downstream offer a mean annual ΔV of 0.6131 m/s (the default setting), this increases to 2.2105 m/s for 5 days. Initial orbit insertion and estimation errors do not alter the long-term costs approximation as these effects stabilize after 14 days.

Regarding the optimization analysis, the heuristic PSO and Nelder-Mead optimization algorithms indicated that further reductions in annual ΔV can be achieved by dynamically adjusting individual tracking arcs. The best case, coming from the PSO algorithm, reduces the annual cost to 0.280$\pm$0.0134 1σ m/s, or a 54.323$\pm$2.186 1σ % reduction with respect to the baseline value. Multiple test runs of the optimization algorithms are done, yielding different solutions for different optimization algorithms, model fidelities and model durations. For a given optimization setting, a total of 5 different configuration solution are found, so there is not one common optimal solution. Moreover, most tracking configuration solutions showed improvement in ΔV over the baseline. Pleas visit Appendix Cfor the exact outcomes.

Nonetheless, there are some caveats to the results. For example, it is questionable whether simulating for 28 days is sufficient to represent the operational lifetime of 1 year. Running optimization routines based on

larger simulation durations, such as a two-fold of 56 days, shows that costs are generally larger than the 28 days where the best mean ΔV for the 28- and 56-day case is 0.32 m/s and 0.45 m/s, respectively. Additionally, including a minimal ΔV threshold, defined by LUMIO's propulsion subsystem specifications, creates more spread in the ΔV optimization outcomes, indicating that subsystem imperfections add more uncertainty to the expected costs. The standard deviation reduces when a larger simulation duration of 56 days was used. Regardless, most optimization solutions have shown to be better than the baseline.

	Configuration	Annual ΔV [m/s]	Reduction [%]
Constant arcs			
Default	Arc length: 1.0 day Arc interval: 3.0 day	0.613 $\pm$ 0.0066 1σ	-00.000 $\pm$ 1.077 1σ
Best	Arc length: 0.5 day Arc interval: 0.5 day	0.375 $\pm$ 0.0020 1σ	-38.597 $\pm$ 0.228 1σ
Orbit based			
Perilune	Arc length: 0.15 day Arc interval: Every 6 passes	0.505 $\pm$ 0.0124 1σ	-17.618 $\pm$ 2.023 1σ
Apolune	Arc length: 0.15 day Arc interval: Every 4 passes	0.498 $\pm$ 0.0082 1σ	-18.760 $\pm$ 1.337 1σ
Optimized	[1.62, 1.13, 1.17, 0.10, ...0.23, 0.10, 0.10] and other See Appendix C for more	0.280 $\pm$ 0.0134 1σ	-54.323 $\pm$ 2.186 1σ

Concluding remarks

All in all, from a mission design perspective, it means that it pays to adapt to a more complex tracking scheme, but employing a constant-type tracking arc timing scheme can also already yield ΔV improvements. The benefit of constant timing configurations is that it is easier to implement due to its better predictability over the more complex schemes derived from the optimization routines. Concerning the consequences of lower station keeping costs as a result of the improved tracking schedule, advances can be made that are related to the reduction in power and fuel budgets. First and foremost, the fuel budget is logically linked to a reduction in fuel consumption, allowing the mission to be operated for a longer period of time. Another contribution to mission operations and spacecraft design comes as a result of the reduction in total tracking time that was observed in the orbit-based and optimized tracking timing configurations. This implies that less power has to be allocated to transmitting ranging signals which means that more power can be budgeted for the payload or assigned to other subsystems. This can increase a mission's scientific contribution by allowing more scientific data to be generated as there is more time to do observations. Lastly, this work has shown that the currently used subsystems of LUMIO can be used in the optimized settings as well. While the lower limit of the propulsion system has some effect on the total costs, improvements over a baseline can still be made. In other words, no major design alterations have to be made to ensure the station keep cost improvements.

Lastly, this thesis provides recommendations for future research. Firstly, it is suggested to increase model realism by incorporating mission planning aspects, such as each spacecraft's science objectives that prevent the spacecrafts from performing inter-satellite links. This can be an important aspect as this constraint can lead to larger dispersion growth and can therefore significantly influence the ΔV requirement. Secondly, it is recommended to use longer simulation durations for cost analyses to reduce cost estimation uncertainty and to improve optimization results. It is also proposed to include spacecraft constraints. For example, more constraints could be introduced based on mission design, such as those accounting for antenna pointing and signal strength. Regarding estimation, a more advanced set of parameters could be added to the estimation model, such as parameters like range bias and dynamic model parameters. Evaluating other orbit geometries beyond the current case study is also advised, as these may present different challenges and opportunities in terms of AOD and navigation. Finally, incorporating automatic on-board decision-making, in which tracking is not pre-planned but decided based on real-time mission needs, is an interesting topic for future research as it adapts to unexpected mission scenarios which pre-planned solutions do not consider.

1 Introduction

This section aims to introduce the topic that will be discussed throughout this thesis work. The scientific context is elaborated upon in Section 1.1. Based on this context, Section 1.2 explains the steps that this work will provide in terms of scientific value. Then, Section 1.3 shows the research questions. Finally, a short overview of the whole document is provided in Section 1.4.

1.1. Scientific context

Small satellites have become increasingly popular for a variety of space applications due to their low cost, compact size, and versatility. Although the exact definition of what constitutes ”small” is ambiguous, it can be referred to satellites that are most often categorized with masses of at most 500 kg [1, 2]. With developments in the miniaturization of spacecraft systems and availability of lower cost launchers, such type of satellite paves the way for increased academic and educational interest [1]. In particular, recent developments show that there is a technical and economic interest for missions in cislunar space [3]. Examples of these missions are the Lunar Meteoroid Impact Observer (LUMIO) [4], Cislunar Autonomous Positioning System Technology Operations and Navigation Experiment (CAPSTONE) [5] and EQUilibriUm Lunar-Earth point Spacecraft (EQUULEUS) [6]. For a mission to be successful, these satellites must perform estimation of their position and velocity in space (orbit determination) and have to determine where the spacecraft has to go and perform the required corrections (navigation). However, the increasing number of satellites poses a stressing factor on existing ground communication networks in terms of tracking availability, such as the Deep Space Network (DSN) [7, 8, 9]. To alleviate this issue, new developments exist that can eliminate the need for Direct-to-Earth (DTE) orbit determination. While it will always be required for telemetry, the orbit determination process can be adjusted. One way to accommodate this challenge is by exploring the concept of autonomous orbit determination (AOD) through inter-satellite links. This enables satellites to obtain their trajectory state information without the direct need for a beacon, such as a ground station [8, 10]. It is desirable to know the state of one or more spacecraft with respect to an inertial reference frame (such as the Earth center). Typically, the state estimation process through ground stations provides this absolute information, because the exact location of the ground station is known with respect to the inertial reference frame. Omitting the ground station removes this knowledge and the process of obtaining state estimation between satellites then has to rely only on relative inter-satellite links. A great benefit of this type of orbit determination is that it can be used with existing radio technologies [11]. Another benefit is that AOD could be used for missions beyond the Earth-Moon system [12] and as such omitting ground stations can also lead to potential benefits related to spacecraft communication power requirements [8, 13], reduced operational costs [14], longer visibility durations [15] and improvements on viewing geometry due to occultation durations [16]. Furthermore, future lunar missions could be located at sites on the Moon where direct communication with Earth is not possible [8, 17, 18, 19].

In the context of AOD, only relative observations, such as range, range-rate or relative viewing angles, should be sufficient to infer the absolute states. In literature, the technique that enables this is known as Linked Autonomous Interplanetary Satellite Orbit Navigation (LiAISON) [20]. To enable satellites to autonomously navigate through space, LiAISON utilizes at least one satellite-to-satellite (SST) observable type, such as range or Doppler, to obtain the absolute states of at least two satellites. To allow for proper estimation using these

inter-satellite links (ISLs), at least one of the satellite orbits has to have a unique size, shape, and orientation due to an asymmetric gravity field [21]. What this means it that only one solution of the initial state could come from the OD estimation process, given a series of SST observables. A benefit of this technique is that it benefits from the fact that existing methods to perform tracking can be used [22, 10].

To demonstrate the capabilities of LiAISON, this work considers a case study in which range-only measurements are performed between the LUMIO L2 Lagrange-point orbiter and the Lunar Pathfinder (LPF) elliptical orbiter [23]. The LUMIO mission is chosen because of the close relation between LUMIO and TU Delft. LPF was chosen because the specific relative geometries between both satellites are known to be favorable to perform inter-satellite navigation [21]. Both satellites are missions in cislunar space, and this case study aims to provide insights into the usage of AOD for satellites in this realm of space and may benefit from incorporating LiAISON in the future. While LiAISON can provide accurate state estimates, the complexity of the dynamic model considered on-board the spacecraft and estimation settings influence this accuracy [21, 24, 11].

Thus far, Turan et al. have modeled the AOD operations of this mission for one LUMIO halo orbit period of 14 days instead of the full 1-year mission timeline [25]. Additionally, this research considered a near continuous stream of observations over this period, which is not feasible due to the scientific objectives and the requirements from the payload or other subsystems. Lastly, the dynamics of LUMIO and LPF based on the simplified circular restricted three-body problem (CRTBP) [25]. One can use an approximated model as long as that is sufficient enough for the position accuracy requirements of a mission. Varying fidelities of the dynamical environment have not been considered in previous studies related to AOD. In reality, there are various force terms that affect the trajectory and in turn also the outcomes of the state estimation. The latest state knowledge is used to perform station keeping maneuvers where the correction depends on the latest position and velocity deviations from the target trajectory. As such, station keeping corrections rely on the latest estimate of the true trajectory. Required corrective maneuvers are based on the accuracy of the state estimate and the dispersion which builds up differently under varying fidelity of dynamic models [26]. This uncertainty can affect the accuracy and timing of such maneuvers [27, 8]. The degree to which the satellite states can be estimated is dependent on the concept of observability, which in turn depends on the relative dynamics between the satellites. Knowledge of this allows us to more effectively time the estimation arcs to match the regions of larger observational effectiveness [25, 21]. This thesis study will investigate the effects that the model fidelity has on the AOD operations. Most importantly, it aims to explore the improvements in the timing of tracking windows that serve the AOD operations for the LUMIO-LPF case study. This knowledge might be generalized and applicable to other orbit scenarios.

1.2. Scientific contribution

This section aims to provide an overview of possible research topics to improve the current body of knowledge of autonomous inter-satellite navigation, with the focus on the timing of satellite-to-satellite links by exploring the envelope of tracking window configurations. Below, one can find the aspects that are considered of relevance for the research based on the performed literature study.

- **Optimized tracking timing**
  The optimization of tracking windows based on observational geometry was done in the past, but it was either applied in context of ground operations [28] or based on a highly simplified dynamical model [25]. Additionally, it appears that most literature considered a continuous tracking scenario which is obviously unfeasible in real scenarios [21, 29]. From an operational and technical perspective, this constant connection with the other satellite might not be feasible [30]. Operational considerations such as time windows dedicated to performing science and the required ADCS of the satellites, or physical limitations such as occultations, caused by the Moon, play a role [31]. Most importantly for this work, it is stated that there exist blackout periods that influence the effectiveness of the OD [21]. Once such a blackout occurs, the most beneficial observations are effectively lost and better moments in time could have been utilized. Knowledge on when those periods occur can be used to concentrate measurements within specific periods [21]. The improved timing of SST sessions could allow for increased state accuracy and thereby alter S/K strategies and ΔV [32].

- **Autonomous navigation assessment for more than one orbital period**
  Turan et al. [11] simulated the orbit determination of LUMIO-LPF over one LUMIO period of 14 days. This

work does not provide a full insight of the fully autonomous behavior of the LPF-LUMIO system over the planned 1-year mission duration. The process of OD, uncertainty propagation and station keeping are all connected but were not brought into one coherent picture. The effect of S/K maneuvers on LiAISON's performance was recommended in literature [8]. Strategies should be implemented to assess the effect of adjusting tracking windows. Without ground station planning, tracking and S/K strategies could be adjusted, while still taking into account constraints on availability between satellites due to ongoing science operational priorities [33, 6], power and accuracy requirements [34, 11], body occultations [6], etc.

- **Improved fidelity of the dynamical model**
  An aspect to consider is that most research was done based on the CRTBP. Hill [21] did an extensive analysis by comparing a large range of orbit combinations using CRTBP. A high-fidelity environment might give a more accurate description of the dynamics which can allow for a smaller error between the predetermined orbit and actual orbit during OD sessions. This might lead to the option to start and/or end the estimation process later and earlier respectively. Additionally, it can be analyzed how the increased computational cost of running increasingly complex dynamic models weighs against the improved state uncertainty and dispersion. This can show to what extend simplified models can be used instead of more complex models.

- **Use of batch least squares estimation for orbit determination**
  Turan et al. [11] incorporated the Extended Kalman Filter (EKF) for the estimation process of the LUMIO-LPF study case. The Batch Least Squares (BLS) estimator has been used in the context of AOD, but for a DRO-HALO scenario [35]. Additionally, this is considered a case of long continuous tracking without breaks. The type of utilized estimation filter affects the state estimation, which also results in an alteration of the state uncertainty [36, 37]. The BLS is used instead of the EKF for its easy implementation and availability within Tudatpy. Generally, the BLS technique is more robust against outliers and requires less stringent selection of a priori covariance, process noise and measurement weighting and to deflect the influence of bad points [38]. Furthermore, one does not need real time solutions as there will be time for processing the full data.

- **Combining orbit determination with navigation**
  While previous research was done on optimizing tracking windows but only includes the OD aspect [25]. Recommendations were made that suggested that a similar approach could be applied to the minimization of the station-keeping maneuver costs, which relies on not just the principle associated with orbit determination/estimation, but also the execution of corrective maneuvers. This work aims to combine those two factors to provide improvements to such OD-only based tracking window optimization.

In short, this work will predominantly combine a set of three main research topics. The aim is to define an exploratory study to see what happens when the mentioned field of knowledge is applied to the context of the LPF-LUMIO orbit configuration.

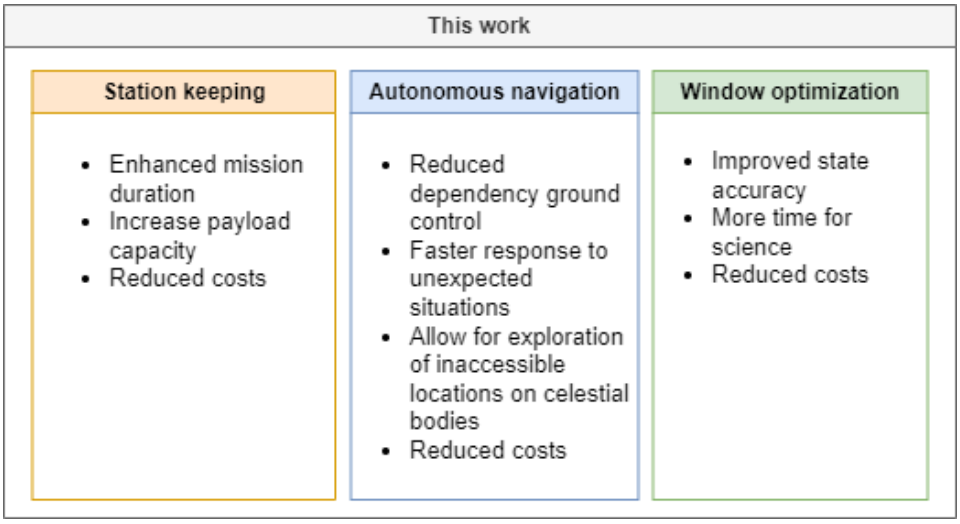

Figure 1.1: Overview of scientific contribution

Operational implications
This work helps in the decision making for future spacecraft. Consider a baseline scenario in which no consideration is made with regards to optimization and a fixed frequency of arcs and duration is always used. The potential research outcomes can be split into two scenarios with corresponding implication from the operational perspective of a mission:

- **Significant improvement over baseline**
  This scenario evidently improves the requirements and design implications associated with maneuver costs. It will allow for an additional degree of freedom that can be considered in the design to improve overall mission quality. In addition, if the total arc length is reduced as well, this could improve power consumption due to fewer observations.

- **No significant improvement over baseline**
  The advantage of this result is the ease of mission design. This is because no additional design constraints are added that could affect the scientific goals as a result of varying availability of the payload. Additionally, the consistency and thus also predictability is preferred for scientists and other stakeholders associated with a mission. The advantage is that there is potentially no weight reduction due to lower correction needs.

1.3. Research questions

Considering the current state-of-the-art, the thesis aims to conduct research concerning the following research objective and questions:

Research objective

This work will consider a case study in which LUMIO and LPF orbits are used to perform numerical simulations with the aim to find the optimal timing of tracking arcs to perform inter-satellite tracking. While this work considers this case study only, the work aims to provide insights for inter-satellite tracking in general. As such, the research objective reads:

"To improve inter-satellite measurement-based autonomous navigation for cislunar orbiters by finding improved tracking timing strategies."

Research question

With the research objective in mind, the main research question is formulated as:

"What is an optimal satellite-to-satellite tracking timing configuration for cislunar orbiters?"

Sub questions

In the research question formulation process, a number of second order questions were identified:

1. *What are the working principles of inter-satellite based autonomous navigation?*
2. *How is the geometry of autonomous navigation observations related to improved system performance?*
3. *What techniques are there to improve the timing of tracking windows?*
4. *How does the fidelity of the on-board dynamic model influence the system performance?*
5. *What parameters have a noticeable influence on the improvement of inter-satellite based autonomous navigation?*
6. *What are operational limitations and benefits associated with improved autonomous navigation performance?*

1.4. Report structure

This report is split up into three main parts. Part I captures the state-of-the-art of autonomous cross-link navigation and discusses in more detail the LPF and LUMIO missions and how they are relevant in the context of autonomous inter-satellite navigation. The layout of this literature study starts by addressing the current trends and challenges in Chapter 2. From this follow the fundamentals related to orbit determination and navigation in Chapter 3. Part II stats with an explanation of the global research setup and the simulation setup in Chapter 4. The resulting findings are touched upon in Chapter 5. The subsequent concluding remarks and recommendations are followed in Part III.

Part I

Literature Research

2

Trends in cislunar missions

A new era of small satellites for space exploration comes with a growing demand for AOD. This reduces dependency on ground-based tracking and provides a significant reduction in operational costs due to overcrowded communication networks [10]. First, a general overview of existing cislunar smallsat missions is given in Section 2.1. Then, introductions of the LUMIO and LPF mission are given in Section 2.3 and Section 2.2, respectively. This is followed by an explanation of the workings of LiAISON in Section 2.4.

2.1. Current cislunar missions

The availability of low-cost and low-volume commercially-of-the-shelf (COTS) spacecraft subsystems has enabled miniaturization in the space sector and commercial viability for missions using small-scale products with applications that we considered impossible before [1]. With the current developments in the field of spacecraft miniaturization, more players have entered the satellite industry [39]. This statement is also true for small satellites. As such, Turan et al. [10] found a total of 64 deep-space missions using small satellites of which the majority of the 64 missions aim to characterize the surface or atmosphere of a body. Furthermore, 34 out of the 64 missions incorporate inter-satellite links for telemetry, telecommand, or navigation purposes. A reason for this large fraction is due to the fact that small satellites lack the power for deep-space communications as most of those satellites rely on a mother-spacecraft that handles the deep-space communication. Of these 34, 22 operate in cislunar space, showing the most relevance for cislunar space (with the purpose of surface mapping and characterization). Of the 22 missions, 5 are planned to be able to perform autonomous radiometric navigation solely based on inter-satellite communication. An overview of the smallsat cislunar missions is provided in Table 2.1 [10].

	Inter-Satellite Link (ISL)	**Direct-to-Earth Link (DTE)**	**Inter-Satellite Link (ISL) + Direct-to-Earth Link (DTE)**
Cislunar Missions	LUMIO, VMMO, CLE*, MoonCare*, NanoSWARM	Lunar Flight Light, Lunar Ice Cube, LunaH-Map, LunIR, ArgoMoon, OMOTENASHI, Cislunar Explorers*, EQUULUES, HALO, WATER, IMPEL, CubeX	MiLuV, BOLAS*, OLFAR**, DSL**, CAPSTONE
Total	5	12	5

Table 2.1: Overview of communication link configurations for different cislunar smallsat missions. (*) = constellation of two satellites and (**) = constellation of more than two satellites. Source: [10].

The majority of the issues related to the use of satellite navigation are:

- **Limited on-board power for communications**
  Only a limited on-board power is budgeted to communication in general [10]. This naturally leads to limited power availability for navigation. Since there is limited on-board power, operators might plan telemetry, telecommand and tracking sessions separately as those can not be done at the simultaneously. Another advantage, yet small, is that Earth-based navigation is prone to atmospheric effects that

can play a role in the effectiveness of radiometric Earth-satellite communication [40, 41]. Additionally, SST tracking happens over smaller distances than contact with Earth, yielding an overall lower free-space loss [8].

- **Congestion of Earth-based navigation**
  Since there will be more spacecraft, conventional Earth-based navigation could lead to congestion of the navigation network, which could yield a shorter contact time for tracking [42]. This is related to the ground station "visibility problem" which is about the communication conflicts that occur when multiple satellites try to communicate with ground stations in the visible range. As the number of satellites increases, the more challenging the visibility problem becomes. How long a spacecraft can have with Earth depends on the altitude and antenna parameters [43]. The communication time could affect the degree to which a spacecraft is at its intended location and thus the accuracy of station-keeping maneuvers (SKMs) [33].

Spacecraft autonomy can lead to decreased costs if ground control operations or hardware are reduced or eliminated [21, 14]. This benefit can also be beneficial to larger spacecraft as the operations cost does not scale with satellite size [10]. Since most navigation is based on a radiometric Earth-satellite link, there is a possibility to use this existing technology to automate the navigation aspect by performing satellite-to-satellite tracking (SST) [10].

2.2. Lunar Pathfinder

The Lunar Pathfinder (LPF), developed by Surrey Satellite Technology Ltd (SSTL), aims to provide solutions to the current problems related to the future of science and exploration in cislunar space. It is part of the ESA Moonlight project to develop a European lunar telecommunications and navigation infrastructure consisting of a network of communications, navigation, and data relay satellites [44]. This is desired in case a data link should be established between Earth and assets on the far side or polar regions of the Moon, such as rovers. Currently, DTE communications require direct line of sign with lunar assets, which means that information to and from those assets can only be sent at a limiting pace and quality [42]. In addition to proving the possibility of utilizing current navigation satellites for lunar positioning, the satellite seeks to monitor space weather in order to gain insight into radiation levels near the Moon, which is critical for human exploration. Lunar Pathfinder is supported by UK Space Agency funding via the European Space Agency [23].

Lunar Pathfinder will operate in an ELFO, for an operational lifetime of over 8 years [23]. The ELFO is both stable and can provide good coverage of the Moon's poles, which is traditionally challenging to cover by Earth ground station networks [45]. Through its two simultaneous channels in S-band and UHF, a X-band DTE link, and its favorable orbit configuration, Lunar Pathfinder allows faster data transfer over a long visibility period between the satellite and Earth [42]. This is promising as it reduces the burden on deep space ground stations currently used for cislunar applications through the autonomous navigation process it can offer. Furthermore, its secondary objective is to test a payload, an ESA GNSS receiver, to perform a weak signal detection experiment from lunar orbit [42].

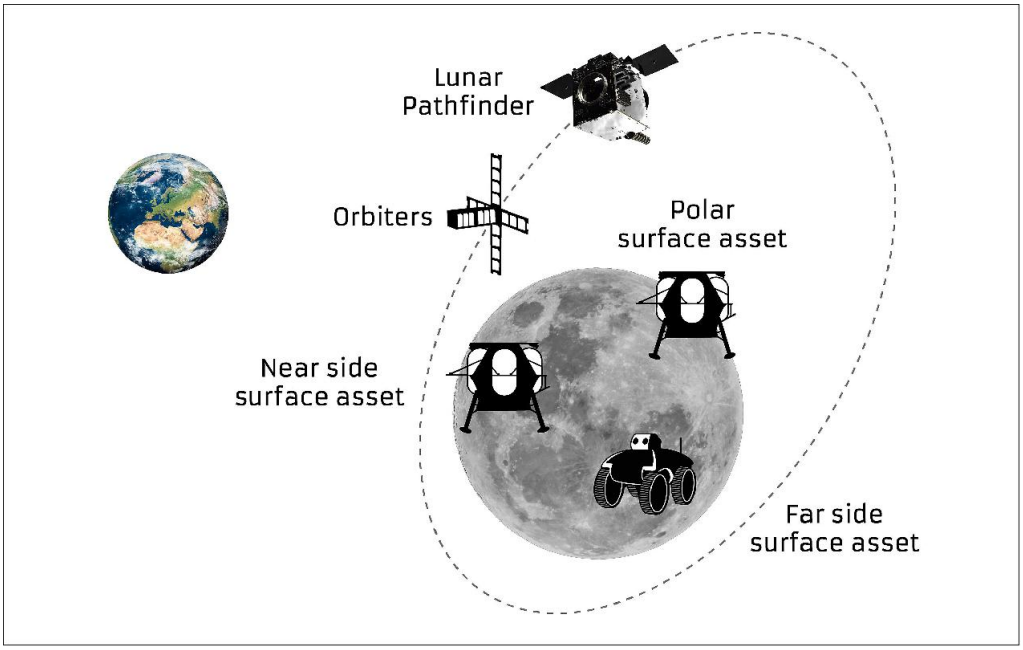

Figure 2.1: Lunar Pathfinder Communications Services diagram. Source: [23]

2.3. Lunar Meteoroid Impact Observer

Earth-based lunar observations are limited by weather, geometry, and lighting circumstances, but a lunar orbiter can enhance the detection rate of lunar meteoroid impact flashes by allowing for extended monitoring periods [46]. The Lunar Meteoroid Impact Observer (LUMIO) is a 12U CubeSat this aims to detect micrometeorite impacts on the far side of the moon. The reason for this is to fill the knowledge gap on the thus far unobserved impact events in the 10^{-4} to 10^{-1} kT TNT equivalent kinetic energy range while also testing the hypothesis of asteroid impact asymmetry between the lunar nearside and far side [4].

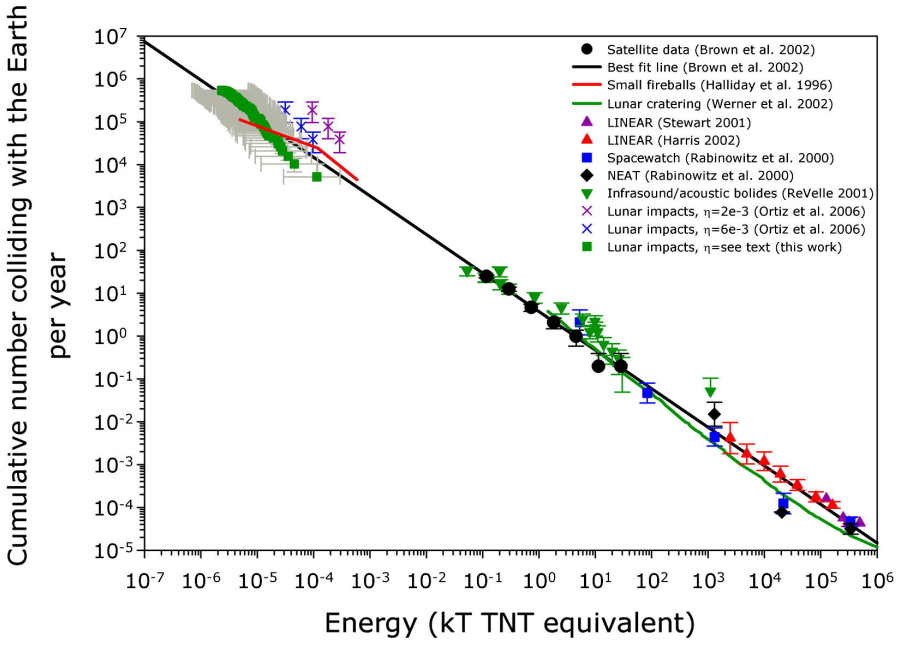

Figure 2.2: Scientific knowledge gap of meteorite impact events for a 10^{-4} to 10^{-1} kT TNT equivalent kinetic energy range. Source: [47]

Its payload, the LUMIO-cam, allows for the detection of flashes on the lunar surface. A consistent image of the lunar far side is ensured by orbiting in a southern quasi-periodic orbit around the Earth-Moon L_2 Lagrange

point. The advantage compared to ground observations is that the observations are not prone to atmospheric effects and the spacecraft can provide a complete view of the lunar full-disk at once [46]. While the navigation primarily is conducted through DTE networks, the mission aims to demonstrate the option for navigation through of small satellites through inter-satellite links. [46]. LUMIO will also show the ability to provide useful scientific data from interplanetary missions using COTS smallsat technologies [4]. Payload data is not transmitted through the LUMIO-LPF link, but through the primary Earth connection. The ISLs between two satellites serves as a redundant commanding link [11]. During the operational lifetime of 1 year, LUMIO's operations are split into two phases: the science cycle, and the navigation and engineering cycle. It involves the orbit determination and subsequent station-keeping maneuvers required to maintain the right conditions during the science cycle [4]. The scheduling between navigation and the science orbits is shown in Figure 2.3.

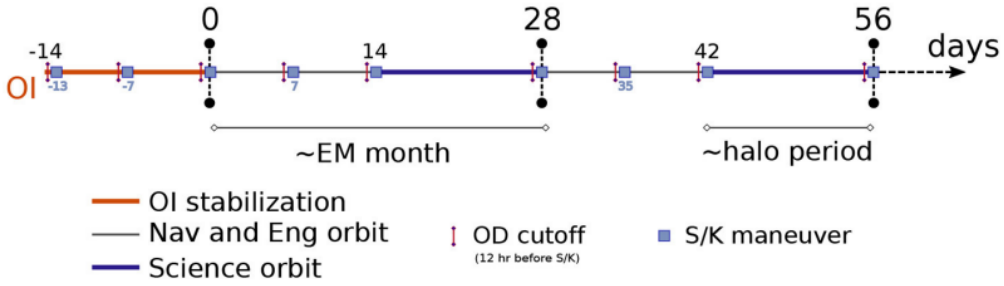

Figure 2.3: Timing strategy employed for station-keeping maneuvers. Source: [46]

LUMIO has been a thesis topic on the past, highlighting different aspects of the spacecraft. De Smaele [48] and Gelmi [49] conducted research on fault detection. Nett [50] focused on the propulsion system. Cipriano [46] and Sirani [46] focused on the design of LUMIO's orbit. Tanis [29] focused on antenna requirements in relation to performing AOD.

2.4. Inter-satellite based navigation

This section aims to provide clarity of the main topic of this work. In fact, multiple different processes are required to accurately simulate a spacecraft that maneuvers through space. Section 2.4.1 explains the differences in the concepts of orbit determination and navigation. Section 2.4.2 elaborates on the differences in the way that the trajectory can be defined.

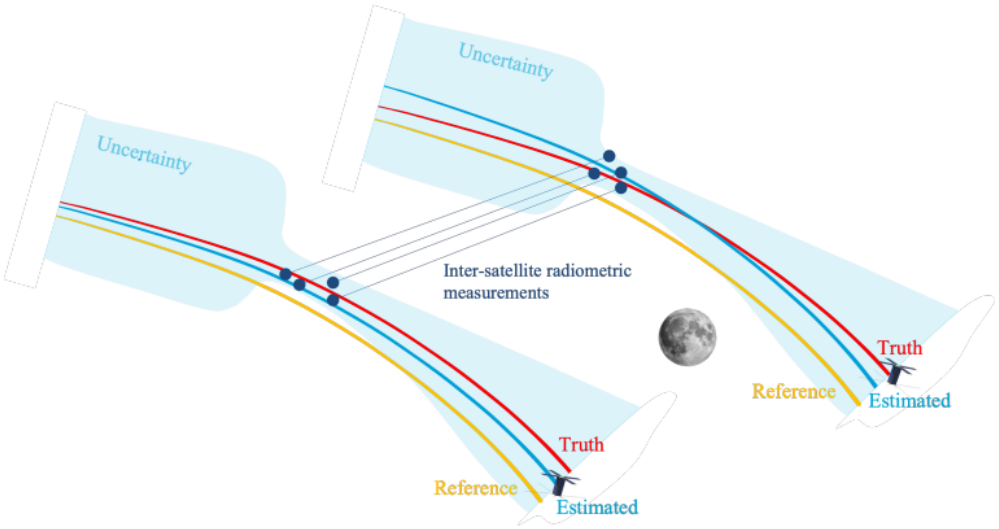

Figure 2.4: Relationship between inter-satellite links and state uncertainty. Source: [25]

2.4.1. Orbit determination versus navigation

Since both terms will be used extensively throughout this work, a distinction is made between the concept of *orbit determination* and *navigation*.

- **Orbit determination**: The process of calculating an object's orbit using observational data [40]. Its primary purpose is to determine the current position and velocity of the object and to predict its future trajectory. In the context of SST, the OD process relies entirely on an initial guess of the state (with an *a-priori* covariance), the inter-satellite observables, the estimator and the dynamic model on-board used to predict the states.
- **Navigation**: The concept of navigation, on the other hand, involves controlling a spacecraft's trajectory. The main goal of navigation is to ensure that the spacecraft reaches its desired destination. This includes making course corrections, which are in turn dependent on the accuracy of the state estimates found from the orbit determination process.

2.4.2. Absolute versus relative states

The trajectories can be defined in multiple ways. There are two ways in which the state of a spacecraft can be represented [51]:

- **Absolute**: Information on the orbit states is known with respect to an inertial reference.
- **Relative**: Information on the orbit states is defined with respect to a moving reference point such as another satellite. To obtain the absolute information one needs knowledge of the absolute position of the moving reference point.

Relative measurements, in a two-body problem, do not provide the absolute orientation of the orbits, but only the relative orientation because the orbits cannot provide a fully unique solution [13]. That is, the absolute states of one spacecraft cannot be known, as there can be more than one solution coming from the estimation process. In such a case, at least one beacon must be added to produce a reference to the inertial frame to add a condition to uniquely solve the rank deficiency problem [51, 52]. Examples of this are introducing GPS [53, 54], measuring with respect to known stars [55], lunar landmarks [56, 57] or incorporating a third satellite with an orbit that is optimized for observability [58]. These examples are based on a two-body problem, so for example an Earth-satellite or a Moon-satellite system.

However, it is possible to obtain absolute state information, so solving the rank deficiency problem, without the need for an additional beacon. Under certain circumstances, LiAISON provides that solution by simultaneously obtaining the absolute states of at least two objects [21]. Hence the name "liaison", which stands for "mutual understanding". The effectiveness of this method depends on the asymmetry of the gravity field in the spacecraft's environment. A region in three body systems where the force due to a perturbing third body is relatively large would be a good candidate for LiAISON as this leads to uniqueness in the respective orbit [21, 59]. In that case, at least one of the satellite orbits has a unique size, shape, and orientation [21, 11]. The relative strength of an particular force term can be quantified by means of a scaling factor defined by Equation 2.1 [21].

$$\alpha_j(\boldsymbol{r}) = \frac{||\boldsymbol{a}_j(\boldsymbol{r})||}{\sum_{i=1}^{n} ||\boldsymbol{a}_i(\boldsymbol{r})||} \tag{2.1}$$

Here, j refers to a particular acceleration term, so $\boldsymbol{a}_j$ denotes the acceleration owing to acceleration source j. A bigger value of α_j for asymmetric acceleration indicates that a spacecraft can employ SST for absolute positioning more effectively. That means that the unique time history of SST observations and thus absolute states are known when the initial conditions are given [8]. The impact of the asymmetric acceleration field on the spacecraft's trajectory must outweigh the noise from observations and the impacts of unmodeled accelerations [21]. Figure 2.5a shows the heat maps of α for acceleration due to the third body in the Earth-Moon system. It indicates that LPOs are good candidates for LiAISON, because of the strong relative strength of the third body in the region where those orbits reside. Halo-Moon constellations are able to retrieve orbit information more quickly than Halo-Halo constellations because a Moon orbit allows the system to acquire observations from many vantage points quickly [21]. For that reason, libration points are a good choice, especially unstable collinear Langrange points (L_1, L_2 and L_3) [60, 8]. In general, radiometric autonomous

navigation would be most beneficial for topologies that have short orbital periods and large inter-satellite distances [61, 21]. For that reason, the LUMIO-LPF system promises very beneficial orbit determination results.

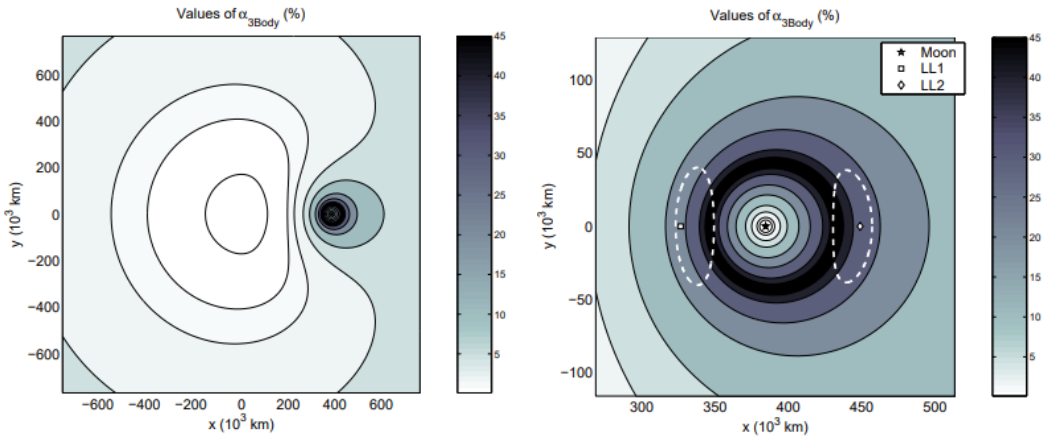

(a) Full Earth-Moon system

(b) Scaled to Moon vicinity

Figure 2.5: Heat map of α for acceleration due to the third body in the Earth-Moon system. Source: [21]

2.4.3. Applications of inter-satellite navigation

An advantage of cross-link radiometric navigation is that it can be used by existing systems [62, 63]. A large benefit comes from the fact that it can circumvent the limits of conventional navigation with regards to the visibility between the ground stations and satellites [21, 63]. Omitting this factor allows the spacecrafts to choose tracking time in a less constrained way, due to the limited ground station visibility [64]. Another benefit is that the inter-satellite navigation can not only be done with spacecraft that are in-orbit, but also with lunar surface assets (LSA) that are not visible from earth [8] or manned missions, such as in the Artemis program [65], where limited tracking with Earth is especially undesired due to increased state uncertainty [35]. Research has been done on two-satellite constellations, but it can be extended to navigation systems of more than two satellites [22, 17, 18, 27, 66]. Other work was done on Lagrange point-geosynchronous constellations [67] or inter-planetary spacecraft [15, 63]. Additionally, supplementing inter-satellite measurements with ground-based measurements can improve tracking performance [8, 15, 63]. The application of inter-satellite based navigation in crewed missions, have also previously been investigated [68].

2.5. Tracking window optimization strategies

There are a variety of options for forecasting the optimal timing for estimation arcs throughout a mission, and this section provides an overview of the available options. Note that all methods are subjected to mission constraints from the individual satellites, such as Station Keeping Maneuvers (SKMs), pointing the antenna beams, the maximum possible range limited by power budgets and planned science phases.

- **Windows at a fixed predefined frequency**
  This is the easiest to implement operationally but does not make use of efficient observational geometries. The estimation arcs occur at fixed intervals, thereby ignoring the observability characteristics of the dynamics at those epochs. This leads to sub-optimal results for the estimator and could yield larger station-keeping costs.

- **Minimizing for global uncertainty**
  An example of optimizing the tracking windows is based on an objective function that aims to minimize the average length of the largest axis of the error ellipsoid for both satellites over a predefined duration [61]. E. Turan [25] used a particle swarm optimization (PSO) technique, often used to tackle complex/large-scale optimization problems [69]. This defines a global best fit in terms of uncertainty but does not necessarily define the most optimal solutions for certain mission specific constraints, such as total power or ΔV costs.

- **Closest angle of observation geometry with unstable uncertainty manifold**
  A scheduler is used to schedule cross-link measurements in a system such that the observation direction, or line-of-sight vector, aligns as closely as possible with the direction of the greatest axis of the instantaneous uncertainty ellipsoid [31, 21]. This aligns with the concepts of observability and the blackout periods explained in Section 3.4. The more the observation direction aligns with the direction of the largest uncertainty, the more beneficial the information in that direction is.

- **Optimizing for a particular mission budget**
  It is beneficial for any spacecraft mission to reduce its consumption of resources as much as possible (within reason). For example, minimizing the total required ΔV could benefit a mission, as it could extend operations for a longer duration. Such cost depends on the state estimate uncertainty before a maneuver [70], which in turn depends on the observation geometry of each spacecraft's location during a tracking arc, thereby suggesting that an optimal set of tracking windows exists that minimizes such cost. Additionally, noise in such maneuvers affects the future states. The degree to which that affect propagates also depends on the location of the maneuver and the time until the next estimate. Another option might be an observation geometry that minimized the total observation time, such that the payload can perform its scientific targets for longer.

- **Combining scheduling of Earth and SST tracking**
  Inter-satellite tracking is accompanied by direct-to-Earth tracking windows. Both types of tracking are taken from different vantage points to the satellite, with benefits and downsides at particular geometries. As such, one can find optimal interval combinations at which the collective effort of Earth-based and LiAISON-based occurs best. This was done by McGranaghan et al. [15] for a GEO and L_1 Lagrange point orbiter configuration.

3

Fundamentals of satellite navigation

Orbit determination is the process of estimating the orbit parameters of an object in space, based on observations. Keplerian or Cartesian states are the most common ways used to describe the position and velocity of a spacecraft in space. In order to establish this process, it requires the modeling of orbit trajectories by using *dynamic models*, generating the incoming measurements using *measurement models*, and estimating the true trajectories given these inter-satellite measurements using *estimation models*. Once the states of the spacecrafts are established, the navigation aspect is initiated. Navigation entails directing an object's path to the desired pre-planned trajectory [38]. For this, one requires a *correction model* to calculate the right magnitude and direction of a station keeping maneuver and to guide the spacecraft in the right direction.

Because this work relies heavily on orbit determination and navigation principles, this chapter aims to provide an overview of all the mathematical models used. One should note that the following content does not only strictly apply to the concept of LiAISON-based navigation, although the measurement model concerns inter-satellite observables rather than the ground-based observables. The intricacies of the dynamical models are explained in Section 3.1. The measurement and estimation models are shown in Section 3.2 and Section 3.3, respectively. With the goal of improving autonomous orbit determination, it is important to define a metric to compare the effectiveness of measurements in the estimation process. This will be touched upon in Section 3.4. The details associated with the correction model are touched upon in Section 3.5. The mechanisms behind the propagation of state uncertainty are touched upon in Section 3.6.

3.1. Dynamic model

The dynamical model in the context of OD entails refers to the state propagation of a satellite in a predefined dynamical environment, depicted by a variety of forces from celestial bodies that exert on a spacecraft. The degree of the fidelity of the dynamical model depends on the number and type of forces that one takes into consideration. Section 3.1.1 introduces the reader with the types of orbits that exists in cislunar space. Then, Section 3.1.2 and Section 3.1.3 will elaborate on the equations of motions (EOMs) associated with varying fidelities of the dynamic models.

3.1.1. Cislunar orbit types

The Earth-Moon system offers a variety of orbits for cross-link radiometric navigation. Next to Lunar and Earth orbits such as LEO, GEO, polar and Elliptical Lunar Frozen Orbit (ELFO), there are also halo orbits [59, 71]. Libration Point Orbits (LPOs) are located around five libration points, of which three are collinear with respect to the axis of the two primaries (L_1, L_2 and L_3), or also known as halo orbits [71]. One of the advantages of L_2 halo orbits is that these can provide great coverage of the lunar far-side and polar regions without blocking the visibility to Earth [72]. Additionally, orbits around the L_2 libration points are appropriate for inter-satellite navigation because they are locally unique and consistently stay in locations with a high degree of asymmetry in the third-body perturbation of the Moon [21]. When a halo orbit is derived from the CRTBP, the orbit can be called periodic for a reasonable length of time. For more details on the CRTBP, go to Section 3.1.2. However, high-fidelity models (n-body dynamical systems) allow such an orbit to deviate from the periodic case in a relatively short time frame motion due to perturbations of external bodies. For that reason, it is called "quasi-

periodic" [21, 33]. The geometry of a halo orbit depends on the Jacobi energy of the spacecraft, C_j [71]. The smaller C_j, the larger the orbit [46].
Equation 3.1 is related to Equation 3.2 and represents the total energy of the tertiary mass (the spacecraft) relative to the non-dimensional rotating reference frame.

$$C_j = 2\left(\frac{1-\mu}{r_1} + \frac{\mu}{r_2}\right) + x^2 + y^2 - \left(\dot{x}^2 + \dot{y}^2 + \dot{z}^2\right) \tag{3.1}$$

Near Rectilinear Halo Orbits (NRHOs) are a subset of the halo families that make close approaches to the smaller body (the Moon) [33]. For example, the CAPSTONE mission makes use of such an orbit [6]. The stability index is smaller for a NRHO compared to that of the nominal halos, so NRHOs are more stable and thus require less fuel for station keeping [46]. There are also orbits that placed around the L_1 and L_2 Lagrangian points but lie entirely in the rotational plane of the Moon around Earth, such as the distant retrograde and Lyapunov orbits [73]. Turan et al. performed analysis specific to the an L_2 LPO-ELFO constellation and showed that the best position observability occurs at moments when LPF is in the high-velocity region, so at the perilune of its ELFO [11]. K. A. Hill simulated a large variety of constellation geometries and concluded that Halo-Moon orbiter constellations provide the best observability effectiveness under the conditions shown below [21]. With regards to inter-satellite navigation using two LPOs, the following statements can be made [21]:

- Spacecraft should have relatively large separation distances.
- Not all the spacecraft can remain in the same plane for their entire trajectories.
- Libration orbits with shorter periods lead to faster convergence. This was found by Turan et al. too [61].

3.1.2. Circular-Restricted Three-Body Problem

In cislunar space, the Earth and the Moon are the two bodies that are the dominant gravitational forces. A large number of dynamic models exist that aim to approximate the full-ephemeris model for varying levels of complexity for the space environment. For example, the Bi-circular Four-body Problem (BFP) considers the Earth and Moon as the two primaries and a third gravitational perturbation such as the Sun [74]. An even more simplified option is to only include the Earth and Moon, but to approximate the mutual elliptical behavior of the orbits of the two primaries. The latter is known as the Elliptical Restricted Three-Body Problem (ERTBP) [74]. The easiest, and most commonly employed model is the Circular-Restricted Three-Body Problem (CRTBP), which is used most often in literature in the context of inter-satellite based navigation [21, 27, 12, 59, 11, 71, 75]. The CRTBP is defined by the following equations of motion:

$$\begin{aligned}
\ddot{x} &= x + 2\dot{y} - \frac{(1-\mu)(x+\mu)}{r_1^3} - \frac{\mu(x+\mu-1)}{r_2^3} \\
\ddot{y} &= y - 2\dot{x} - \frac{(1-\mu)y}{r_1^3} - \frac{\mu y}{r_2^3} \\
\ddot{z} &= -\frac{(1-\mu)z}{r_1^3} - \frac{\mu z}{r_2^3}
\end{aligned} \tag{3.2}$$

$$\begin{aligned}
r_2 &= \sqrt{(x+\mu-1)^2 + y^2 + z^2} \\
r_1 &= \sqrt{(x+\mu)^2 + y^2 + z^2} \\
\mu &= \frac{m_2}{m_1 + m_2}
\end{aligned} \tag{3.3}$$

Here, x, y, and z represent the spacecraft states with respect to the Earth-Moon barycenter in a rotating reference system or synodic frame. These three states define $\boldsymbol{r}$ in Figure 3.1. The system contains three bodies, assigned the following properties: Earth (P_1 and $m_1 = m_E$), Moon (P_2 and $m_2 = m_M$), and spacecraft (P_3, $m_3 = 0$). Equation 3.2 makes use to dimensionless parameters: μ represents the dimensionless mass distribution, r_1 is the distance between P_3 and P_1, and r_2 is the distance between the P_3 and P_2. This model assumes no perturbations from bodies other than the primary and secondary bodies, zero spacecraft mass, and a time-invariant Earth-Moon distance. The CRTBP can generate a family of LPOs, ranging in size. Under the idealized environment of the CRTBP, these solutions can be perfectly periodic. This is not the case when orbital perturbations exist in the environment as is explained in Section 3.1.3.

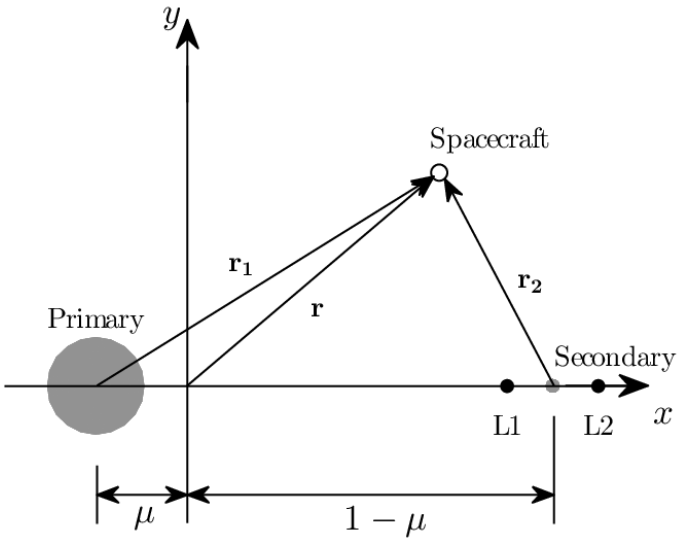

Figure 3.1: The xy-plane of the CRTBP Earth-Moon synodic frame. Source: [76]

3.1.3. Full ephemeris models

In reality, the dynamical system is complex because it includes a large variety of perturbing forces on the spacecraft. Because planets and moons aren't orbiting in purely circular, co-planar orbits in the real solar system have no longer any periodic solutions. The same primary locations do not reoccur in any acceptable amount of time [77]. The best representation would be a "full-ephemeris" model that includes accurate time-dependent positions of all celestial bodies. The dynamics of spacecrafts is represented by a set of equations of motion like in Equation 3.10, yielding a nonlinear first-order ordinary differential equation represented in the form shown in Equation 3.4. Here, $\boldsymbol{f}$ is a summation of the force terms defined in terms of the state $\boldsymbol{x}$.

$$\dot{\boldsymbol{x}} = \boldsymbol{f}(\boldsymbol{x}, t) \tag{3.4}$$

Acceleration modeling

As was mentioned in Section 2.1, the largest demand for small satellites is for missions that operate in cislunar space. For this reason, this environment will be of our concern in this section. In this region of space, forces acting on a spacecraft include gravitational influences from the Earth, Moon, and Sun, and solar radiation pressure. Gravitational influences can be modeled as a coming from a point mass or based on an irregular mass distribution of a celestial body, also known as *spherical harmonics*). Gravitational influences can come from Earth and the moon, but also from other bodies in the solar system. Among these, the most relevant terms are the gravity terms of the Earth and Moon and the solar radiation pressure [21]. Orbit trajectories of a close distance near the celestial body, such as a very low Moon orbit, make the trajectory more susceptible to the order and degree of spherical harmonics of the celestial body, while satellites further away from the body have a larger sensitivity to solar radiation pressure coming from solar radiation. A visual representation of all acceleration terms can be found in Figure 5.4 and Figure 5.5.

In the list below, more detail is provided regarding force terms.

- **Point mass gravity**

  In the point mass model, one considers the gravitational attraction between a spacecraft and other celestial bodies treated as point masses. This model accounts for the gravitational influence from planets, moons, and other significant bodies in the solar system [38].

$$\boldsymbol{f}_{PM} = -\frac{\mu_t}{\|\boldsymbol{r}\|^3}\boldsymbol{r} - \sum_i \mu_i \left(\frac{\boldsymbol{r}_i}{\|\boldsymbol{r}_i\|^3} + \frac{\boldsymbol{r} - \boldsymbol{r}_i}{\|\boldsymbol{r} - \boldsymbol{r}_i\|^3} \right) \tag{3.5}$$

The first term is the force on a spacecraft defined with respect to the origin of an inertial reference system in with a target body in defined, such as the Earth-centered J2000 frame. The first term of the sum describes the forces exerted by the target body on other bodies. It is important to note that all bodies are gravitationally attracted towards each other as well, which is defined in the second part of the sum.

- **Solar radiation pressure**

  There are various ways in which solar radiation pressure (SRP) can be simulated, but this study assumes the cannonball radiation method [38]. In this model, one assumes that the spacecraft's effective area A remains constant and unaffected by its orientation. This is a valid assumption because the largest area of a spacecraft, most likely the extended solar arrays, is typically pointed towards the Sun.

$$\boldsymbol{f}_{SRP} = \frac{C_R L_S}{4\pi c} \frac{A}{m} \frac{\boldsymbol{r} - \boldsymbol{r}_s}{\|\boldsymbol{r} - \boldsymbol{r}_s\|^3} \tag{3.6}$$

  It should be noted that there might be moments when the irradiation from the Sun does not occur and thus no solar radiation pressure is exerted on a spacecraft. One such aspects is the effect of occultations [78, 79]. In such case, the Moon can block the sunlight reaching a satellite and consequently Equation 3.6 does not occur in the EOMs. Literature shows that for EM L2 Lagrange point orbits, Earth and Moon induced shadows occur biannually and monthly respectively and increasing a Lagrange point orbit's amplitude decreases the total shadow times [78, 77].

- **Spherical harmonics**

  The spherical harmonics relies on the gravitational potential, which is defined for a given body of arbitrary geometry and mass distribution, at a point outside the planet itself by the following equation [38]:

$$U = \frac{\mu}{r}\left[1 - \sum_{n=2}^{\infty} J_n \left(\frac{R}{r}\right)^n P_n(\sin\phi) + \sum_{n=2}^{\infty}\sum_{m=1}^{n} J_{n,m}\left(\frac{R}{r}\right)^n P_{n,m}(\sin\phi)\cos m\left(\Lambda - \Lambda_{n,m}\right)\right] \tag{3.7}$$

  This potential includes Legendre polynomials, depending on the order m and degree n.

$$P_n(x) = \frac{1}{(-2)^n n!}\frac{d^n}{dx^n}\left(1 - x^2\right)^n \quad P_{n,m}(x) = \left(1 - x^2\right)^{m/2}\frac{d^m P_n(x)}{dx^m} \tag{3.8}$$

  For the spherical harmonics acceleration terms, the relationship between potential and force is fundamental: forces in a conservative field can be derived as the negative gradient of a potential function [38]. In that case, the total force from spherical harmonics of any order and degree can be defined as

$$\boldsymbol{f}_{SH} = -\nabla U \tag{3.9}$$

The net acceleration of the spacecraft is the vector sum of all these forces. Combining the contributions from the spherical harmonics model, the SRP model, and the point mass model gives the total acceleration. To cover all other forces that exists $\boldsymbol{f}_{others}$ is added.

$$\boldsymbol{f}_{net} = \boldsymbol{f}_{PM} + \boldsymbol{f}_{SRP} + \boldsymbol{f}_{SH} + \boldsymbol{f}_{others} \tag{3.10}$$

3.1.4. Differential shooting technique

An important aspect to mention is that some trajectories, such as the L2 Lagrange point orbit, are not perfectly periodic in a high-fidelity environment in contrast to the CRTBP as discussed in Section 3.1.2. In the case of perturbations other than a point mass from Earth and Moon, LPOs are inherently unstable. Numerical simulations in higher-fidelity dynamical models yield a state history in which the Lagrange point orbiter departs from the ideal periodic solution after one to two revolutions [80]. For LUMIO one revolution equates to approximately 14 to 28 days [11]. For longer time periods, periodic-like solutions can be found, commonly referred to as quasi-periodic orbits, which can be used as a multi-revolution reference solution that the spacecraft should follow. These orbits are generated by means of the *multiple differential shooting* technique [80]. This method aims to generate adjustments to the velocity element of the state vector at the start of so-called *patch points*,

given constraints on position and velocity continuous between the patch points [77]. In this work, such reference trajectory is provided by an external party as will be touched upon in Section 4.1.

3.2. Measurement model

When observation data histories do not exist, one has to simulate observations based on the expected spacecraft state, which is done using the *measurement model*. The most common satellite observation types are range and range-rate [40] but line-of-sight (LOS) angles are also used [22]. To enable inter-satellite based navigation, radio-frequency LOS data is sometimes paired with range measurements [62]. For the LUMIO mission it was shown that range-only measurements provide better accuracy than range-rate only measurements [11]. For that reason, range is chosen to be the only observable type under consideration, which is defined by the a geometrical distance between the two spacecraft plus noise and bias terms that arise from imperfections in the measurements as shown in Equation 3.11. ρ_{bias} depends on the delay in round-trip light time caused by the satellite clock states, and the signal line and transponding delays [11].

$$\rho = \sqrt{(x_1 - x_2)^2 + (y_1 - y_2)^2 + (z_1 - z_2)^2} \quad + \rho_{bias} + \rho_{noise} \tag{3.11}$$

3.3. Estimation model

Equation 3.11 serves as the foundation for developing an *estimation model* for which the goal is to estimate spacecraft states that best match the inter-satellite range observations [36]. This section is split up into three subsections. Section 3.3.1 elaborates on the estimation techniques that can be used and explains the estimator choice for this work. Section 3.3.2 touches upon how linearization techniques are used to estimate states in non-linear dynamical systems. Lastly, the last steps to solve for estimate solutions are explained in Section 3.3.3.

3.3.1. Types of estimators

There is a variety of algorithms that can be used to estimate spacecraft states based on incoming observations from the *measurement model* of Section 3.2. These are divided into two main groups: sequential estimation and batch estimation [40, 38, 81]. Both methods are similar in that they aim to decrease the uncertainty between the estimated state and true state and [82, 83]. The difference between these types is that the sequential estimator updates the estimate with every incoming measurement. The batch estimator, however, processes an entire observation set, also known as a batch, at once for a given *tracking arc* or *fit span*. As such, it collects one or more observations before estimating the next state as shown in Figure 3.2. A commonly used batch estimator is the Batch Least Squares estimator (BLS) which finds the best state estimate based on minimizing the sum of squared residuals between the estimated trajectory and the trajectory obtained through measurements [40]. BLS estimators are mostly used for offline processing purposes, driven by operational scenarios in which data can only be downloaded within certain time windows and processed later (such as ground stations) [21]. Regardless, the BLS estimator generally offers the benefit of producing state estimates with lower error-covariance than sequential estimation techniques [40]. Other benefits with respect to sequential estimation algorithms are that BLS is less susceptible to initial estimation errors than sequential estimators and that it is better a handling observation outliers [38]. Because of these benefits, this work only considers a BLS estimator. While sequential estimators are more common in literature in the context of AOD, BLS has been applied to this context before [21, 56, 36] and it is integrated neatly within the architecture of the Tudatpy package [84].

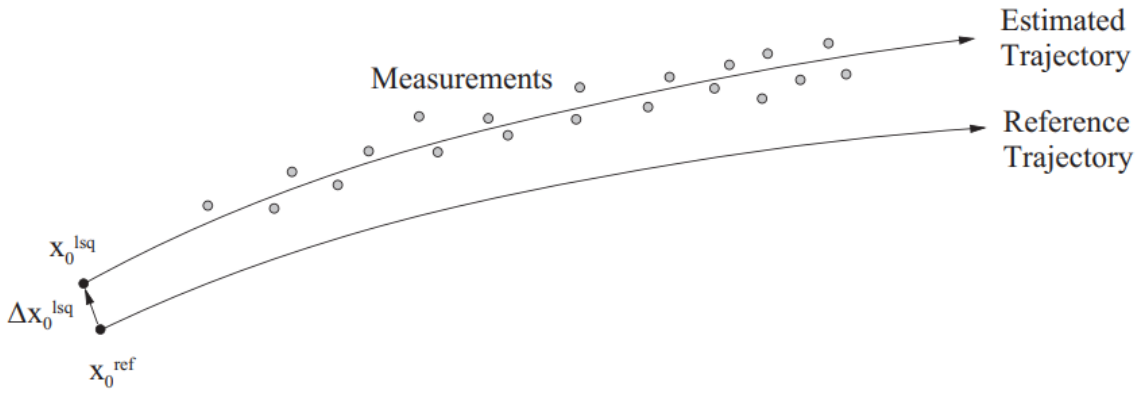

Figure 3.2: Batch Least Squares filter. Source: [40]

3.3.2. System linearization

Typically, as can be seen by the equations in Section 4.3 and Section 3.2, the dynamics and measurements are described by non-linear equations with respect to the state variables. The BLS approximates the state estimate by linearizing the non-linear dynamics and measurement equations with respect to a reference point because the least squares approach works best with linear relationships [40]. Linearization refers in essence to using the first term of the Taylor series of an otherwise non-linear function. As a caveat, linearization discards higher-order terms in the system dynamics, which may be significant in certain scenarios such as perilune in lunar elliptical orbits [16, 70]. The Taylor series approximation of the dynamics and measurement equations could be extended to higher order terms to capture some of the effects caused by non-linearities in more advanced methods [85]. For the same of simplicity, this will not be considered in this work.

In the context of a system with two satellites, the state vector is defined as shown in Equation 3.12. Here, the subscripts 1 and 2 refer to LPF and LUMIO respectively. This notation will be used extensively throughout this document.

$$\boldsymbol{x} = [\boldsymbol{r}_1, \boldsymbol{v}_1, \boldsymbol{r}_2, \boldsymbol{v}_2] \tag{3.12}$$

In the linearized least squares algorithm, instead of estimating the absolute state, $\boldsymbol{x}$, the deviations along a reference point $\boldsymbol{x}^*$, $\Delta\boldsymbol{x}$, are used as indicated in Equation 3.16 and Equation 3.17 [40]. An asterisk (*) indicates that the values of $\boldsymbol{x}$ and $\boldsymbol{y}$ are from the reference path from Equation 3.4 with the initial conditions $\boldsymbol{x}^*(t_0) = \boldsymbol{x}(t_0)$. Note that the same parameter is indicated as $\boldsymbol{x}_0^{ref}$ in Figure 3.2. The measurement residuals $\Delta\boldsymbol{y}$ are defined as the difference between the true observations and the observations derived from the linearized observation-state relationship with respect to the reference point $\boldsymbol{x}^*$.

$$\Delta\boldsymbol{x} = \boldsymbol{x} - \boldsymbol{x}^* \tag{3.13}$$

$$\Delta\boldsymbol{y} = \boldsymbol{y} - \boldsymbol{y}^* \tag{3.14}$$

The propagation of $\Delta\boldsymbol{x}$ is done by the State Transition Matrix (STM), indicated as $\boldsymbol{\Phi}(t, t_0)$. The STM describes how a state evolves from an initial time t_0 to a later time t. An initial deviation $\Delta\boldsymbol{x}(t_0)$ is mapped onto epoch another epoch, giving $\Delta\boldsymbol{x}(t)$. $\boldsymbol{\Phi}(t, t_k)$ [40]. The STM will be used extensively throughout this work and is calculated as shown in Equation 3.15 [38]. Besides deriving the STM from numerical integration, it should be noted that the same STM can be approximated using a Taylor series as well [86, 87, 88, 89].

$$\dot{\boldsymbol{\Phi}}(t, t_0) = \left.\frac{\partial \boldsymbol{f}}{\partial \boldsymbol{x}}\right|_{\boldsymbol{x}=\boldsymbol{x}^*} \boldsymbol{\Phi}(t, t_0) \tag{3.15}$$

Once $\dot{\boldsymbol{\Phi}}(t, t_0)$ is defined, the future values of $\Delta\boldsymbol{x}(t)$, based on the to be estimated $\Delta\boldsymbol{x}(t_0)$ can be defined using Equation 3.16. The same method done is used for the propagation of the measurement residuals of Equation 3.14 as shown in Equation 3.17.

$$\Delta\boldsymbol{x}(t) = \boldsymbol{\Phi}(t, t_0)\, \Delta\boldsymbol{x}(t_0) \tag{3.16}$$

$$\Delta \boldsymbol{y}(t_i) = \tilde{\boldsymbol{H}}_i \Delta \boldsymbol{x}(t_i) = \left.\frac{\partial \boldsymbol{h}}{\partial \boldsymbol{x}}\right|_{\boldsymbol{x}=\boldsymbol{x}_i^*} \Delta \boldsymbol{x}(t_i) \tag{3.17}$$

Note how the measurement residual is connected to the state residual. This is due to the fact that the values of ρ of Equation 3.11 are converted into $\tilde{\boldsymbol{H}}_i$ at each measurement epoch, as shown in Equation 3.18, which defines the measurement Jacobian matrix that relates the observables to the state vector. Defining $\tilde{\boldsymbol{H}}_i$ can be done analytically or numerically. Erdem et al. [11] provides analytical expressions for the entries of Equation 3.18. Most importantly, this matrix defines the *observational geometry*, which affects the ability to obtain information about a certainty state during the estimation process. In other words, the values in this array define the degree of observability as will be discussed in Section 3.4. $\tilde{\boldsymbol{H}}_i$ is converted into $\boldsymbol{H}_i$ through Equation 3.19, which relates the observations to the growth of state uncertainty with respect to t_0.

$$\tilde{\boldsymbol{H}}_i = \begin{bmatrix} \frac{\partial \rho}{\partial x_1} & \cdots & \frac{\partial \rho}{\partial \dot{z}_2} \end{bmatrix} \tag{3.18}$$

$$\boldsymbol{H}_i = \tilde{\boldsymbol{H}}_i \boldsymbol{\Phi}\left(t_i, t_k\right) \qquad \boldsymbol{\Phi}\left(t_i, t_k\right) = \operatorname{diag}\left[\boldsymbol{\Phi}_1\left(t_i, t_k\right), \boldsymbol{\Phi}_2\left(t_i, t_k\right)\right] \in \mathbb{R}^{12\times 12} \tag{3.19}$$

Regarding timestamps, measurements are divided into fit spans or tracking arcs defined by $k = 1, \ldots m$. For every arc k there are measurements $i = 1, \ldots \ell$. The dimension of $\tilde{\boldsymbol{H}}_i$ depends on the amount of measurement types that are included in the simulation and quantity of elements of the state vector. For each epoch in a fit span the measurement residuals and STMs are calculated. The observation-state relationship at t_i is mapped back to the epoch at the start of the measurement batch t_k [21].

3.3.3. Normal equation

Once the linearized equations are established, the final step can be done in which the elements of Section 3.3.2 are combined to solve for the state estimate. The best estimates in this scenario are computed by minimizing a cost function of the observation residuals using the so-called *normal equation* as shown in Equation 3.22. When measurements contain uncertainties like noise, a "weighted" version of this equation is used to compensate in estimation errors coming from these uncertainties, which is done by adding the measurement weighing matrix $\boldsymbol{W}$ as defined by Equation 3.20 [40]. When one has only one type of observable, when the matrix converts into a scalar quantity.

$$\boldsymbol{W} = \begin{bmatrix} \frac{1}{\sigma_1^2} & 0 & 0 \\ 0 & \ddots & 0 \\ 0 & 0 & \frac{1}{\sigma_n^2} \end{bmatrix} \tag{3.20}$$

Errors are typically assumed to be independent from previous measurements of the same observation type [40]. The normal equation in Equation 3.22 consists of the *information matrix* $\boldsymbol{\Lambda}$ and *information vector* $\boldsymbol{N}$. The information matrix reflects how much information the observed data provides about the states. Larger values of the entries in the matrix imply that the observations provide a lot of information about the state, leading to more precise estimates. Smaller values indicate less information and therefore less precision in the estimates [38].

$$\begin{aligned} \boldsymbol{\Lambda} &= \boldsymbol{P}_0^{-1} + \boldsymbol{H}^T \boldsymbol{W} \boldsymbol{H} = \boldsymbol{P}_0^{-1} + \sum_{i=1}^{\ell} \boldsymbol{H}_i^T \boldsymbol{W} \boldsymbol{H}_i \\ \boldsymbol{N} &= \boldsymbol{H}^T \boldsymbol{W} \Delta \boldsymbol{y} = \sum_{i=1}^{\ell} \boldsymbol{H}_i^T \boldsymbol{W} \Delta \boldsymbol{y}_i \end{aligned} \tag{3.21}$$

An *a-priori* covariance matrix $\boldsymbol{P}_0$ could be added to the information matrix in case there is already some knowledge about the state to guide the estimator towards a solution. Note that the normal equation calculates an estimate of the state deviation $\Delta\hat{\boldsymbol{x}}$ instead of the state itself, $\hat{\boldsymbol{x}}$, as can be seen in Equation 3.22. The calculation of $\hat{\boldsymbol{x}}$ is an iterative process, which goes as follows. A new updated trajectory is calculated, the steps of Equation 3.21, Equation 3.22 and Equation 3.23 are performed. Until a desired convergence level is reached, these steps are repeated. Convergence can be quantified in terms of estimation error or the number of iterations [38].

$$\Delta\hat{\boldsymbol{x}} = \boldsymbol{\Lambda}^{-1}\boldsymbol{N}\Delta\boldsymbol{y} \tag{3.22}$$

$$\hat{\boldsymbol{x}} = \boldsymbol{x} + \Delta\hat{\boldsymbol{x}} \tag{3.23}$$

3.4. Observability

An important aspect related to state estimation is the concept of observability, which refers to the capacity to acquire a unique estimation solution for spacecraft states [40, 52]. An increase in observability is related to an increase in state estimation accuracy and is used when one wants to relate orbit determination performance to the relative spacecraft geometry, measurement type, accuracy or measurement frequency [21, 52, 51]. It is the level of observability that defines why some orbit constellations are better able to perform AOD than others as a direct consequence of the geometric diversity of the orbit trajectories [79]. In other words, there are constellations in which for each measurement or batch of measurements more useful information is added to the estimation than for other constellations, as some orbit configurations are not able to obtain a unique solution based on relative observations [90].

This section is split up into three subsections. Firstly, Section 3.4.1 touches upon how observability is defined and how its performance is quantified. This is then followed by Section 3.4.2 that focuses on what analysis have been done so far in relation to observability, particularly in terms of inter-satellite orbit determination. Lastly, Section 3.4.3 elaborates upon the notion that the spacecraft states are coupled and how it can affect the navigation process.

3.4.1. Quantifying state observability

The degree to which radiometric measurements provide information on the states can be quantified from the eigenvectors and eigenvalues resulting from the information matrix or *observability Gramian* $\boldsymbol{\Lambda}$ as shown in Equation 3.24. It represents the sum of "observation effectiveness" elements $\delta\boldsymbol{\Lambda}\left(t_i\right)$ at observation $i = 1, \ldots \ell$ with $\delta\boldsymbol{\Lambda}\left(t_i\right) \in \mathbb{R}^{12\times 12}$ [21]. Note that Equation 3.24 is the same as Equation 3.21 but without the *a-priori* covariance [79]. For this reason, for measuring total observability, one should ignore $\boldsymbol{P}_0$ as it tends to give a warped image of the true observability as the estimate is guided towards a specific solution with priori knowledge instead of purely based on measurements only. [21].

$$\boldsymbol{\Lambda} = \sum_{i=1}^{\ell} \delta\boldsymbol{\Lambda}\left(t_i\right) = \sum_{i=1}^{\ell} \boldsymbol{H}_i^T \boldsymbol{W} \boldsymbol{H}_i = \sum_{i=1}^{\ell} \boldsymbol{\Phi}^T\left(t_i, t_0\right) \tilde{\boldsymbol{H}}_i^T \boldsymbol{W} \tilde{\boldsymbol{H}}_i \boldsymbol{\Phi}\left(t_i, t_0\right) \tag{3.24}$$

A property of $\boldsymbol{\Lambda}$ is that its inverse is the covariance matrix $\boldsymbol{P}$. With a known *a-priori* matrix $\boldsymbol{P}_0$, observability and covariance can be related. $\boldsymbol{P}_0$ can artificially make the system observable and should therefore technically not be used in observability analyses [22].

$$\boldsymbol{\Lambda} = \boldsymbol{P}_0^{-1} + \sum_{i=1}^{\ell} \boldsymbol{H}_i^T \boldsymbol{W} \boldsymbol{H}_i \tag{3.25}$$

One aspect is that the information matrix has to be positive definite in order for the system states to be considering observable [21]. While the degree of observability varies under each geometry, an information matrix with condition number (defined as the ratio of the greatest eigenvalue to the lowest eigenvalue) lower than 10^{16} is still considered positive definite and can then serve as a metric to assess whether the estimator is able to provide a unique solution [21]. The uniqueness of such a solution can only be established when the STMs of both spacecraft are different, which is only possible when at least one of the spacecrafts in the system has a unique orbit. If this is not the case, then the entries of Equation 3.18 become linearly dependent.

The effectiveness of the measurement for a particular position state can be represented as the eigenvalue belonging to the eigenvector of the respective state. The norms of the eigenvectors derived from $\boldsymbol{\Lambda}$ are an indication of the amount of useful information gathered from an observation of a particular state. The maximum of observability effectiveness of the position vectors can be described by Equation 3.26 [21]. The symbol i refers to the columns of $\delta\boldsymbol{\Lambda}$.

$$\sqrt{max||eig(\delta\mathbf{\Lambda}_i)||} \qquad i \in 1,2,3 \tag{3.26}$$

How state uncertainty changes over time is defined by the $\mathbf{\Phi}\left(t_i,t_0\right)\mathbf{\Phi}^T\left(t_i,t_0\right)$, also known as the *monodromy matrix* [21]. This matrix gives special eigenvalue properties [21, 91]. The last two of its six eigenvalues indicate the stable and unstable manifolds or, in other words, the principle axis in the ellipsoid that have $||\lambda|| \leq 1$ and $||\lambda|| > 1$ respectively [92]. If the STM is propagated over other time scales than one orbit period, one obtains "local" manifolds. An unstable manifold refers to the direction in the error ellipsoid in which state uncertainty builds up over time. A more effective observation senses along the wide axis of the uncertainty ellipsoid. The more perpendicular the observations are with respect to the unstable manifold, the worse the observation effectiveness. This can be seen by the timing and extent of "blackout periods" over time by K. A. Hill [21]. Since the observation direction with respect to the error ellipsoid matters, it means that measurement effectiveness depends on the relative orbit geometries of the two satellites performing SST. Plotting observability provides insight into an optimal timing observation strategy while taking into account the limitations of the sensors on-board. The moments at which the eigenvalues of the information matrix are the largest could be the best moments to perform observations [93]. The observability can also be applied when estimating model parameters [93].

From the eigenvectors derived from the monodromy matrix one can also find the "sensitivity", a slightly different metric but seems to refer to the same idea as state above [46, 94].

$$S = \frac{1}{2}\left(||\lambda_i|| + \frac{1}{||\lambda_i||}\right) \tag{3.27}$$

In Equation 3.27, one uses the eigenvalues from the monodromy matrix associated with the (un)stable subspace of the orbit. In case an orbit is stable or unstable, one has $S \leq 1$ and $S > 1$ respectively [94]. Another way to quantify the degree of observability is by the condition number. This is defined as the ratio of the largest to the smallest eigenvalue of the information matrix. A smaller condition number represents better observability [79]. The system is considered not observable if the condition number is larger than 10^{16} [95, 21].

3.4.2. Previous observability research

Most observability analyses in terms of AOD have been performed based on orbits around the Earth in the context of formation flying. These were based on angle-only [90, 96, 97, 51, 98], angle and angle-rate [93] or range-only [64, 52, 99, 100] measurements. For such two body systems, only local observability can be achieved without additional predefined knowledge on the system because these two body problems provide more than one solution for a set of measurements [100]. More importantly, cislunar formations with LPOs were conducted as well, although to a lesser extend compared to Earth or lunar orbiters [21, 11, 79]. The amount of information acquired at a certain epoch can be seen in Figure 3.3 and Figure 3.4. The left subfigure shows position observability for two satellites in different lunar orbits and the figure on the right indicates a constellation of a lunar orbiter with a L_2 Lagrange point orbiter. It is important to note the dips in $\delta\mathbf{\Lambda}$ which indicates that at those locations, observability is lower.

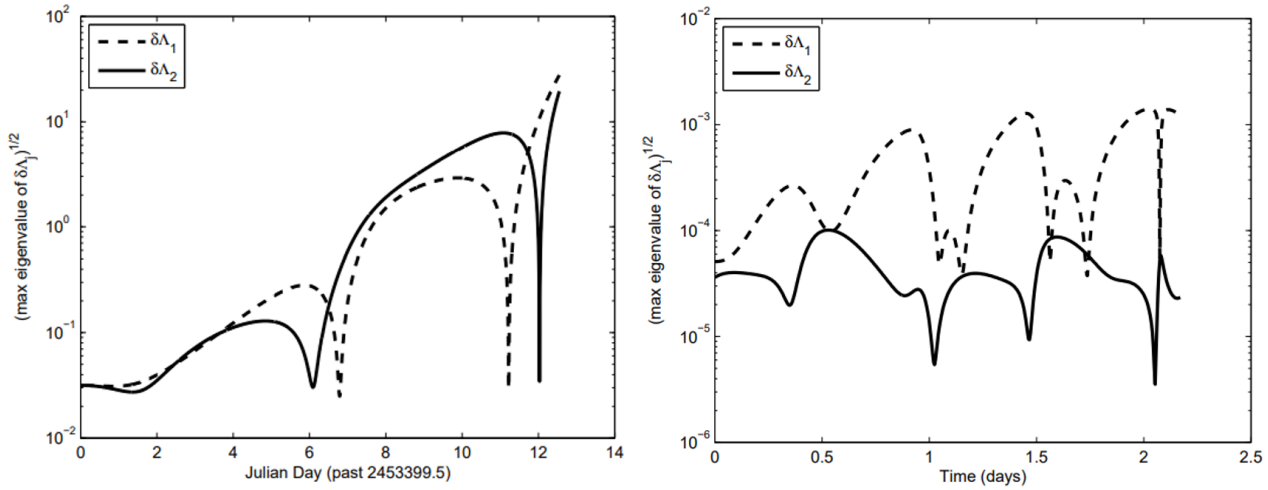

Figure 3.3: Position observation effectiveness for two different orbit combinations. Source: [21]

Another example of the time change of position state observability can be seen in the research done on the LUMIO/LPF mission by Turan et al [11]. The orange plot corresponds with the elliptical lunar orbiter LPF and the blue plot is related with the L_2 Lagrange point orbiter. Clearly, the observability of LPF varies more than that of LUMIO. LUMIO's observability does not vary as much and more measurements yield better knowledge of the position states. Fluctuations can be seen after day 6 for LUMIO, which is a direct result of the inter-connectedness as a result of the inter-satellite observations. The peaks and dips in the LPF plot correspond with the knowledge that passes in regions of faster dynamics (perilune) yield larger observability for position states and lower observability for velocity states [70, 101, 31]. The opposite is true for apolune [70]. What this means is that it might be more beneficial to perform tracking sessions at perilune to estimate position states and at perilune to estimate velocity states. As a caveat it should be noted that convergence issues could arise when one estimates in the perilune region [31]. This is because of the validity of the assumption of linearization, as discussed in Section 3.3.2, can breaking down, which prevents the estimation algorithm, as discussed in Section 3.3.3, from converging to a solution.

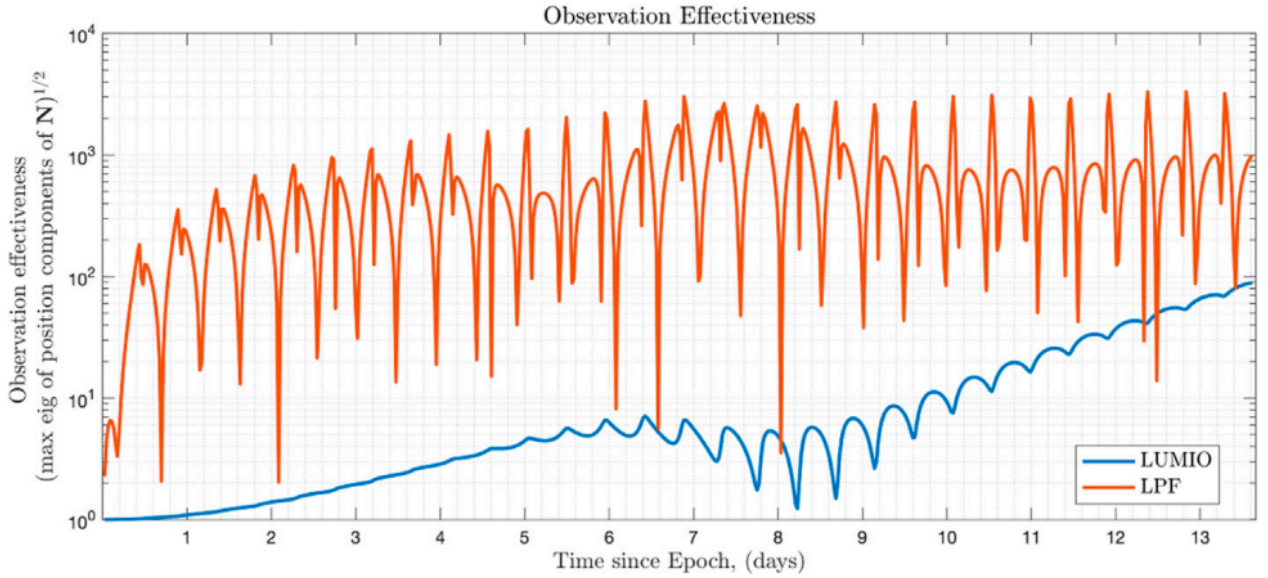

Figure 3.4: Observation effectiveness of the LUMIO-LPF constellation. Source: [11]

3.4.3. Spacecraft state coupling

When the measurement Jacobian $\boldsymbol{H}$ is decomposed into its elements, as shown in Equation 3.28, it becomes clear that its constituents consists of terms related to both satellites as indicated by the subscripts 1 and 2.

This is because the observational geometry, indicated by the partial derivatives, are taken for ρ, which is a function of the states of both satellites as was explained in Section 3.2.

$$\boldsymbol{H} = \tilde{\boldsymbol{H}}\boldsymbol{\Phi}\left(t_k, t_0\right) = \begin{bmatrix} \frac{\partial \rho}{\partial \boldsymbol{r}_1}\boldsymbol{\Phi}_{1,rr} & \frac{\partial \rho}{\partial \boldsymbol{r}_1}\boldsymbol{\Phi}_{1,rv} & \frac{\partial \rho}{\partial \boldsymbol{r}_2}\boldsymbol{\Phi}_{2,rr} & \frac{\partial \rho}{\partial \boldsymbol{r}_2}\boldsymbol{\Phi}_{2,rv} \end{bmatrix} \tag{3.28}$$

How this translates into the information matrix is made clear by Equation 3.29, which is based on Equation 3.24.

$$\boldsymbol{\Lambda} = \boldsymbol{P}_0^{-1} + \frac{1}{\sigma_\rho^2}\sum_{i=1}^{\ell} \begin{bmatrix} \frac{\partial \rho}{\partial x_1}\boldsymbol{\Phi}_{1,xx}\frac{\partial \rho}{\partial x_1}\boldsymbol{\Phi}_{1,xx} & \cdots & \frac{\partial \rho}{\partial x_1}\boldsymbol{\Phi}_{1,xx}\frac{\partial \rho}{\partial z_2}\boldsymbol{\Phi}_{2,z\dot{z}} \\ \vdots & \ddots & \vdots \\ \frac{\partial \rho}{\partial z_2}\boldsymbol{\Phi}_{2,z\dot{z}}\frac{\partial \rho}{\partial x_1}\boldsymbol{\Phi}_{1,xx} & \cdots & \frac{\partial \rho}{\partial z_2}\boldsymbol{\Phi}_{2,z\dot{z}}\frac{\partial \rho}{\partial z_2}\boldsymbol{\Phi}_{2,z\dot{z}} \end{bmatrix}_i \tag{3.29}$$

From Equation 3.29 is becomes clear that not only the observational geometry leads to state interconnectedness. In fact, cross terms exists that combine the growth of state uncertainty, defined by Φ, of both satellites into one mathematical product. Since $\boldsymbol{\Lambda}$ will be directly used in Equation 3.22 to calculate state estimates, the orbit determination process inherently depends on the states of both spacecraft simultaneously. The estimation uncertainties of spacecraft 1 and 2 rely on parameters related to each other, which can indirectly affect the correction costs of a satellite as shown in Equation 3.30. However, it should not be forgotten that the dispersion with the target orbit also plays a role. This will be discussed in Section 3.5.

$$\sigma_1\left(\frac{\partial \rho}{\partial \boldsymbol{r}_1}, \frac{\partial \rho}{\partial \boldsymbol{r}_2}, \boldsymbol{\Phi}_1, \boldsymbol{\Phi}_2, \sigma_\rho\right) \leftrightarrow \sigma_2\left(\frac{\partial \rho}{\partial \boldsymbol{r}_1}, \frac{\partial \rho}{\partial \boldsymbol{r}_2}, \boldsymbol{\Phi}_1, \boldsymbol{\Phi}_2, \sigma_\rho\right) \rightarrow \Delta \boldsymbol{V}(\sigma_2) \tag{3.30}$$

3.5. Correction model

Over longer durations of time, perturbative forces will divert a spacecraft from its desired orbit. Station keeping maneuvers (SKMs) should be incorporated to allow for a mission to operate successfully for extended periods of time [8, 68, 94]. The *correction model* will calculate such SKMs to enable a spacecraft to follow its targeted reference trajectory. In the context of LUMIO, this path is given by a continuation model as was explained in Section 3.1.4.

This section is split up into two subsections. Firstly, Section 3.5.1 will touch upon an algorithm that is used to calculate the costs associated with the SKMs. Then, Section 3.5.2 mentions some points in terms of the mission design that can affect the station keeping costs.

3.5.1. Target point method

The Target Point Method (TPM) calculates impulsive station keeping maneuvers by minimizing a weighted cost function that is expressed in terms of ΔV and state deviations from the predefined reference orbit [32, 102]. Howell and Pernicka [103] initially proposed using this method for LPOs in the Earth-Moon system in 1993 and the LUMIO and EQUULEUS small satellite missions have adopted the TPM [46, 5]. A visual representation of the method is shown in Figure 3.5. The process consists of a few steps which will be explain in this subsection.

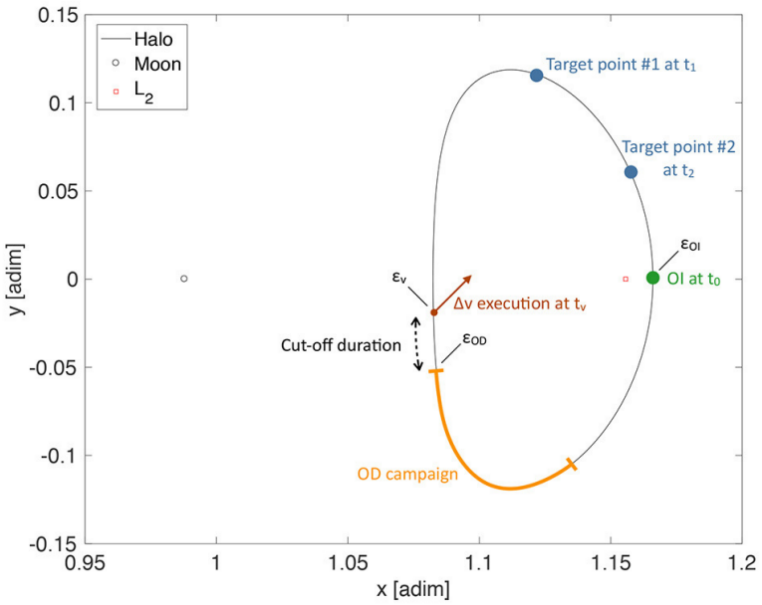

Figure 3.5: Illustration of the target point method for an L2 orbiter. Source: [46]

Firstly, consider a region in a LPO where a tracking arc is initiated, indicated by the yellow region in Figure 3.5. After the tracking session is finished, the latest state estimate is used to calculate the correction required to guide the spacecraft to the target points of which the calculation is based on minimizing the objective value defined by Equation 3.31.

$$
\begin{aligned}
J_{SKM} &= \Delta \boldsymbol{V}_{SKM}^{T} \boldsymbol{Q} \Delta \boldsymbol{V}_{SKM} + \sum_{i=1}^{N_{pt}} \boldsymbol{b}_i^{T} \boldsymbol{R}_i \boldsymbol{b}_i \\
\boldsymbol{b}_i &= \boldsymbol{\Phi}_{rr}(t_c, t_i) \Delta \boldsymbol{r}_c + \boldsymbol{\Phi}_{rv}(t_c, t_i) \Delta \boldsymbol{v}_c + \boldsymbol{\Phi}_{rv}(t_v, t_i) \Delta \boldsymbol{V}_{SKM}
\end{aligned}
\tag{3.31}
$$

From Equation 3.31 it is clear that the objective depends on SKM cost, $\Delta \boldsymbol{V}$, and its expected dispersion at a future target point number i. Figure 3.5 shows a cut-off duration, which is based on the fact that the updated state estimate is typically sent back and forth between Earth and the spacecraft to calculate the correction maneuver [46]. As a result, there is a period between the end of tracking and actual SKM. In the context of this study, there is no need for communication with the Earth, which leads to the assumption that this cut-off time is negligible and that, consequently, the maneuver occurs instantly after the latest tracking arc. Additionally, note that Figure 3.5 shows two target points. This is not required, as long as at least one is used as the indexing at the summation symbol in Equation 3.31 suggests.

Then, the most optimal SKM is calculated with Equation 3.32 which is the result when setting the partial derivative of J_{SKM} with respect to $\Delta \boldsymbol{V}$ to zero and rewriting the equation to an equation for $\Delta \boldsymbol{V}_{SKM}$. As shown in Equation 3.32, $\Delta \boldsymbol{V}$ depends on the on-board dynamic model ($\boldsymbol{\Phi}$), the position and velocity deviation between the estimated orbit and reference orbit ($\Delta \boldsymbol{r}_c$ and $\Delta \boldsymbol{v}_c$) and weighting matrices ($\boldsymbol{R}_i$). The entries of the weighting matrices are assumed constant throughout all calculations. Higher orbit methods versions of Equation 3.32 exist [104], but this will be not be dealt with in this work.

$$
\begin{aligned}
\Delta \boldsymbol{V}_{SKM} &= \boldsymbol{A} \sum_{i=1}^{N_{pt}} \left(\boldsymbol{\alpha}_i \Delta \boldsymbol{r}_c + \boldsymbol{\beta}_i \Delta \boldsymbol{v}_c \right) \\
\boldsymbol{A} &= - \left[\left(\boldsymbol{Q}^T + \boldsymbol{Q} \right) + \sum_{i=1}^{N_{pt}} \boldsymbol{\Phi}_{rv}^{T}\left(t_v, t_i\right) \left(\boldsymbol{R}_i^T + \boldsymbol{R}_i \right) \boldsymbol{\Phi}_{rv}\left(t_v, t_i\right) \right]^{-1} \\
\boldsymbol{\alpha}_i &= \boldsymbol{\Phi}_{rv}^{T}\left(t_v, t_i\right) \left(\boldsymbol{R}_i^T + \boldsymbol{R}_i \right) \boldsymbol{\Phi}_{rr}\left(t_c, t_i\right) \\
\boldsymbol{\beta}_i &= \boldsymbol{\Phi}_{rv}^{T}\left(t_v, t_i\right) \left(\boldsymbol{R}_i^T + \boldsymbol{R}_i \right) \boldsymbol{\Phi}_{rv}\left(t_c, t_i\right)
\end{aligned}
\tag{3.32}
$$

In case there is only one target point and assuming unit weight matrices, then Equation 3.32 can simply be rewritten as Equation 3.33. Note that in this case, the expression for $\Delta \boldsymbol{V}$ seems to be simply linearly related to the position and velocity deviation with respect to the reference trajectory.

$$\Delta \boldsymbol{V}_{SKM} = -\boldsymbol{\Phi}_{rv}^{-1}\left(t_c, t_i\right) \boldsymbol{\Phi}_{rr}\left(t_c, t_i\right) \Delta \boldsymbol{r}_c - \Delta \boldsymbol{v}_c \tag{3.33}$$

3.5.2. Operational considerations

Note that while Figure 3.5 only considers one tracking session and correction, it is up to the mission design requirements how many of such tracking plus correction sessions are performed. In order to avoid that SKMs are conducted unnecessarily often and to model hardware limitations of real propulsion systems, an additional constraint could be set on the minimum magnitude of $\Delta \boldsymbol{V}$ per maneuver. In other words, when the required correction, as calculated by Equation 3.33, is smaller than this threshold, the maneuver is canceled and the correction is performed at the next opportunity. Literature has performed such station keeping scenario with a L_2 LPO based on threshold values of 0.02 m/s and 0.03 m/s and showed that total costs increases with increases threshold value [105]. Depending on the expected values of $\Delta \boldsymbol{V}$ throughout a mission, propulsion subsystems requirements are set. Or, as the other way around, the correction strategy is adapted to the limitations of the propulsion system. Another consideration related to the propulsion system is the accuracy of the correction itself. It is known that errors in the execution of SKM maneuvers leads to increased $\Delta \boldsymbol{V}$ [8, 106].

Additionally, the SKMs are influenced by the magnitude of estimation error [107, 32], which means that the magnitude of $\Delta \boldsymbol{V}$ is influenced by the observability as discussed in Section 3.4 [108, 21]. A logical conclusion from this is that it means that an important factor for station keeping is the choice of the satellite constellation in which the inter-satellite tracking is performed. The LPF-LUMIO case study serves as a good candidate for such constellation as touched upon in Section 3.4.

The cost also simply relies on the shape of an orbit itself and the perturbations that are imposed on the satellite in the respective physical environment. This thesis works with LUMIO with an L_2 LPO, but SKMs can be performed on other orbits as well. It is known that co-linear halo orbits (L_1, L_2 and L_3) are inherently unstable [109, 60, 79] and that relatively low magnitude SKM corrections are required for those halo orbits compared to for example Distant Retrograde Orbits (DROs) [59]. Another way to link an LPO orbit and $\Delta \boldsymbol{V}$ is through the Jacobi energy of the orbit, of which the definition of Jacobi energy is defined [46]. In the context of LUMIO, a Jacobi constant of 3.09 was chosen such that the $\Delta \boldsymbol{V}$ for year of SKMs is kept minimal [46]. For more details on LPOs, please revisit Section 3.1.1.

Lastly, the choice on the SKM timing pattern can have a drastic influence on the accumulated $\Delta \boldsymbol{V}$. For example, the worst-case 1-year operational SKM $\Delta \boldsymbol{V}$ of the LUMIO orbit was found to be 28.1 m/s (μ + 3σ), but it should be noted that this value is based on a tracking timing in the sequence of 7, 7 and 14 days [46]. While this maneuver frequency design enables excellent science orbit operations, it comes at a higher cost compared to a more evenly distributed SKMs [46]. With regards to these distributed SKM timings, literature recommends carrying out three to four SKMs every halo orbit to minimize cost [109]. Additionally, it was proven that increasing the minimal interval between SKMs can significantly increase the accumulated $\Delta \boldsymbol{V}$ for a LPO [105].

3.6. Uncertainly propagation

Ideally, measurements of the true spacecraft state are done as often as possible. However, this might not always be possible or necessary. To obtain a notion of the growth of estimation uncertainty over time, one needs to propagate the statistical moments of this distribution over time. The values of these moments depend on the errors included in the measurement and dynamical models [40]. If there are no errors in the dynamical model, noise and bias that occur throughout the measurement process are the only cause of errors between model and actual state values [106]. Not including models parameters in the estimation leads to an overly-optimistic noise-only covariance matrix time evolution and does not represent a realistic uncertainty envelope anymore [82, 83]. In the non-ideal case, dynamical model errors can be split up into the categories of aleatory and epistemic errors [110, 106].

- **Epistemic errors**

Errors caused by a slight misrepresentation of the true accelerations in the acceleration model, i.e. to save on computer memory and processing time. Numerical solution techniques, such as discretization and approximation errors, and convergence precision, are also considered epistemic errors.

- **Aleatory errors**
  Errors that arise from the inherent stochastic nature of reality. If there were no epistemic errors, there would still be some random errors between expectation and reality.

In general, the uncertainties are believed Gaussian and independent, as this makes to possible to describe the distribution of the state by just the first two statistical moments, so mean and covariance [106]. There exist a variety of techniques to quantify the state uncertainty. Three commonly used techniques are explained below.

- **Monte Carlo**
  An intuitive solution which works on non-linear systems and with Gaussian uncertainties [106]. This method randomly generates initial state errors, propagates the dynamics and creates an empirical distribution, and thus mean and variance of the states. The statistics may only be generated for one epoch and lead to a large computational burden [85, 106].

- **Linear covariance analysis**
  Another option which requires a linearization the system [33, 106]. This can be done under the assumptions that

  1. A linearized model approximates the dynamics of nearby trajectories sufficiently with regard to a certain trajectory (the STM from Section 3.1 is used for this)
  2. A Gaussian probability distribution can properly capture the uncertainty. That is, no biases exist in the state and measurement uncertainties

  Estimating the time span over which Linear covariance (LinCov) can be used is then based on of knowledge of when the Gaussianiaty assumption breaks [24]. Additionally, since non-linear uncertainty propagation methods demand a greater amount of processing power than linear propagation methods, estimating the time when the Gaussianity of the uncertainty breaks is critical for obtaining optimal computational effectiveness [24]. Multiple approaches exist to determine when this happens, such as the Henze-Zirkler test for multivariate normality (MVN) or the Unscented transform based normalized offset (UNO) [111]. This method is computationally much more efficient and can be used in autonomous on-board mission planning [112, 113]. However, with the linearized system it becomes challenging to obtain the uncertainty from the orbit when the spacecraft is in an unstable environment or when evaluated over a relatively long time frame [85].

- **State Transition Tensors**
  A higher-order version of the STM where its terms can be added to the linearized version of LinCov as an extension of the Taylor series. Non-linear factors that are overlooked during the linearization process might have a significant impact on the solution's correctness [114]. In order to effectively explain uncertainty, the State Transition Tensors (STTs) account for non-linearities in the propagation of the mean and covariance [114, 26, 85]. More accurate information regarding the real trajectory can contribute to a faster state estimation convergence [85]. This can be done by means of an adapted version of the EKF: Higher-Order Numerical Extended Kalman Filter (HNEKF) [106, 115].

  Benefits include:

  1. The STTs are costly to compute. However, once the STT history for a particular reference trajectory is obtained, the result is algebraically evaluated on-board to forecast the influence of any state deviation, eliminating the need for many on-board integrations to evaluate the final trajectory distribution for every run.
  2. Faster on-board computations for station-keeping maneuvers. It enables near-real-time trajectory planning in response to navigation errors, or other unanticipated events.
  3. Because nonlinear dynamics are more easily captured, the state departure from a reference orbit is more precisely known. As a result, the region of convergence for these approaches should be

bigger than when only the first term is used. This could lead to smaller maneuver cost and thus a longer mission lifetime.

Overall, the STT approach outperforms others in terms of computational burden versus accuracy [116, 117]. Under impulsive maneuvers, an adapted version of the STT is used in the covariance analysis [117]. This work uses the linearized version for simplicity reasons.

With a better knowledge of uncertainty development, one could establish tracking approaches that minimize the number of observations necessary to tighten the uncertainty envelope [118]. An important aspect to note is that some dynamical regimes other than two-body periodic dynamics, like libration point orbits and near-rectilinear orbits, require adaptations to the standard STT method for accuracy and time improvements [119].

3.7. Overview coupling navigation system

The most important aspect to remember is that the total $\Delta \boldsymbol{V}$ is the result of a complex coupled system, described by, but not necessarily limited to, the following parameters:

$$\Delta \boldsymbol{V}(M, \boldsymbol{d}, \sigma_{OD}, T_{OD}, t_{SKM}, t_c, N_{TP}, T_{TP}, \sigma_{obs}, N_{obs}, \sigma_{SKM} ...) \tag{3.34}$$

Parameter	Description
M	The force model used on-board for state predictions in the estimator. If the outputs of this model are close to the reference orbit, the required corrections are smaller. However, the fidelity affects the calculation on-board as well.
$\boldsymbol{d}$	The dispersion relates the estimated state to the reference state. If it is still far off, then the correction would be larger.
σ_{OD}	State uncertainty of the estimation process influences the accuracy of the SKM as the correction is based on knowledge of the current position. Corrections downstream depend on the accuracy of previous maneuvers.
T_{OD}	The amount of useful information captured in an estimation arc depends on the satellite dynamics occurring in the given window. More observed geometry affects the accuracy of the state estimates.
t_{SKM}	Time of the maneuver, depends on durations and start epochs of previous arcs, doing it later leads to more state uncertainty again.
t_c	Cut-off time between OD and a maneuver calculation, depends on the computational efficiency of on-board electronics. Leads to a delay in maneuver.
N_{TP}	Number of target points chosen in a maneuver calculation.
t_{TP}	Epochs of target points chosen in a maneuver calculation.
ϵ_{obs}	Noise level of measurements. More noise leads to more state uncertainty.
N_{obs}	Amount of measurements. More measurements lead to accurate estimation results.

Table 3.1: Description of station keeping cost variables

The estimation error and dispersion both play a crucial role on the total $\Delta \boldsymbol{V}$. With more measurements, the estimation error should theoretically convergence to smaller and smaller values. In that case, the dispersion could play a larger influence on the total maneuver costs instead. Figure 3.6 shows a schematic overview showing how the trajectories of Figure 2.4 are related to the error terms which then lead to a value of maneuver cost. Note how the correction themselves can be an error source as well. That means that a correction itself can alter the ideal downstream trajectory.

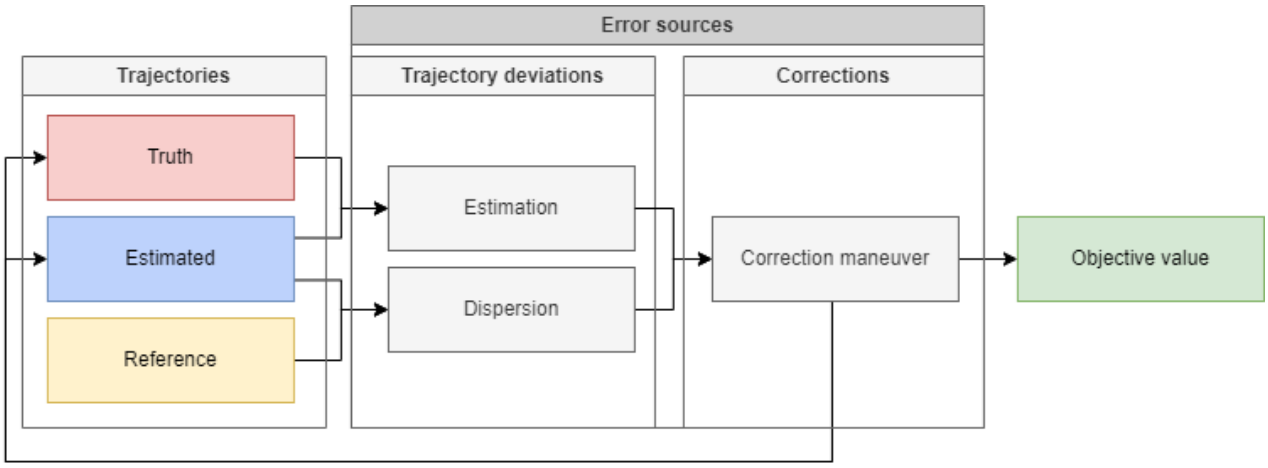

Figure 3.6: Overview of the contributors of maneuver costs

Part II

Main Matter

4

Methodology

There are various methods to optimize a time window as described in Section 2.5. This chapter aims to provide one with insights into the research structure that is used to explore solutions for improved tracking window configurations. The foundation of this work relies on the use of external packages and data sets, which is touched upon in Section 4.1. The main assumptions and details regarding the setup of the simulation is described in Section 4.2 and Section 4.3, respectively. Lastly, the setup that is used to explore the simulation results is explained in Section 4.4.

4.1. Software and data sets

The simulation framework makes use of a combination of publicly available packages and data sets in order to perform the calculations. The information touched upon in Section 4.1.2 is not available online but was made available on request.

4.1.1. TU Delft Astrodynamics Toolbox

Throughout this work, all calculations related to orbit propagation and estimation were conducted by means of the TU Delft Astrodynamics Toolbox (TUDAT). TUDAT contains a robust collection of validated astrodynamics functionalities [84]. TUDAT's functionality is built in C++ but includes a Python wrapper called tudatpy. Besides the propagation of translational and rotational states of bodies, tudatpy possesses an extensive estimation capability that enables one to estimate initial states, biases and other model parameters through Batch Least Squares, using various observables. It has been used before in a previous thesis work on LUMIO [29]. Tudatpy integrates the Spacecraft Planet Instrument C-matrix Events (SPICE) toolkit from NASA's Navigation and Ancillary Information Facility (NAIF), which includes the JPL DE405 ephemerides database. The usage of this database is common practice in literature when it concerns those higher-fidelity models [21, 59, 8, 120, 15]. A downside of tudatpy is that it is still in production and documentation is a work in progress. Another relevant TU Delft-built work is the CRTBP Autonomous Orbit Determination application, built in Matlab by Erdem Turan. While this application is built based on the CRTBP only, it could be used to validate the TUDAT CRTBP equivalent. This program is not publicly available.

4.1.2. Reference trajectory

The reference trajectory of LUMIO is a pre-planned orbit generated at Politecnico di Milano in Italy. This orbit is generated based on an algorithm that generates a continuation model, resembling the targeted orbit over the time frame of MJD 59091.50 until MJD 61325.00, which is from August 8th 2020 to April 4th 2026. It is assumed that the discontinuities as a result of generating the continuation model are negligible in comparison with the orbit estimation and orbit correction errors that LUMIO is subjected to in this work. This trajectory will serve as the basis for all of LUMIO's SKM calculations. This work assumes that the mission starts on March 21st 2024. This is based on a date that was mentioned in previous study and earlier thesis work also used this date. This date is considered valid under the notion that the orbital period LPF is small and therefore similar observational geometries occur as well when the simulator starts at later dates.

4.2. Simulation assumptions

The predominant assumptions and its corresponding thought process are discussed in this section.

- **Simulation represents a longer mission scenario**
  The simulation results are representative enough for a longer mission duration than modeled. Due to computational constraints, it is not feasible to run a simulation over a full period of 365 days, especially when a Monte Carlo simulation is performed. For this reason, the cost associated from a simulation with a duration of 28 days was chosen. This value is scaled appropriately to 365 days.

  However, consider the first stage of the simulation which is the orbit insertion stabilization phase. Since the simulation starts with some initial estimation error as remnants from the previous orbit phases to get to the LPO, the ”nominal” conditions are assumed to occur after those effects have faded out. Only then SKM costs are certain to be the direct result of the the AOD using inter-satellite links only. This stable behavior is assumed to occur after one LUMIO orbit of approximately 14 days, as was also suggested by Cipriano et al. [46]. With a default simulation duration of 28 days, this means that the cost derived after 14 days, so 14 days, will be used for the annual SKMs cost calculation. A longer propagation time should see how valid this assumption actually is.

- **No cut-off time**
  SKMs occur instantly after a new state estimate is obtained. The run time required to propagate the states known on-board from the updated initial state to the current epoch is considered negligible compared to the total arc length, orbital periods or even the arc duration. In reality, the duration of simulating this depends on a lot of factors such as the processor and fidelity of the used model. A comparison of the run time of various dynamic models should validate the validity of this assumption.

- **Instantaneous maneuvers**
  Similarly to the cut-off assumption, the orbit corrections are assumed to be impulsive and to occur instantaneously after the last epoch of an estimation arc. This means that LUMIO is assumed to have instantaneously moved its propulsion system in the right direction such that the maneuvers are conducted in the right direction. The validity of this assumption should be made clear by defining the individual SKMs after each arc and calculating the corresponding burn time associated with those SKMs given the propulsion subsystems of LUMIO.

- **No station keeping for LPF**
  This work only looks at the SKM cost associated with LUMIO because its halo orbit is known to be inherently unstable compared to other orbits such as that of LPF as touched upon in Section 3.1.1. Additionally, it allows for a degree of simplicity by considering the tracking window optimization and its operational implications for one mission only. The last reason is that the reference trajectory of LPF is simply not given, so it is challenging to know what a valid reference trajectory would be.

- **Initial correction maneuver interval of 4 days**
  Literature suggest that 3 to 4 maneuvers is the optimal station-keeping frequency for a halo orbit [109]. For an orbit period of LUMIO of approximately 14 days, and assuming the mean of 3.5 maneuvers per halo orbit, it would equate to an interval of 4 days between maneuvers. In order to compare to this scenario with potentially better results, a baseline scenario tracking window configuration is made where the duration of each arc is 1 day with a 3-day separation between the start of a new arc and the last maneuver.

- **Full line-of-sight availability of both spacecraft**
  In reality, not only the translational dynamics of the spacecrafts are important, but also the rotational dynamics. In order to establish a proper link, both spacecraft should point towards each other with a decent pointing accuracy for sufficient signal power transfer. Additionally, the spacecraft have their own mission goals in which payload have to point towards their respective target locations at specific epochs and are thus not available for links at any time.

- **No systematic model errors**
  The model does not assume systematic measurement and dynamic model errors. In other words, bias was not considered in the calculations. This was done to eliminate additional error sources besides measurement noise that could impact tracking window optimization.

4.3. Full simulation framework

This section serves to provide a clear notion of what is expected from the simulation that is used to simulate the inter-satellite tracking and correction maneuvers. The main goal of this simulation is to obtain an approximation of the annual costs associated with orbit corrections for LUMIO, expressed in ΔV (m/s), over a period of 28 days as discussed in Section 4.2. More details on this assumption can be found in Section 4.3.1.

Figure 4.1 illustrates the structure of the full simulation framework, which is split up into its main model constituents, as highlighted by the blue column. Each blue model block relies on the information passed from the previous blocks. This section aims to provide an extensive overview of the simulation framework by systematically clarifying details related to each block. An overview of the numerical details can be found in Table A.2.

The simulation framework is made with the mindset to adjust *dynamic, measurement, estimation and correction models* in a modular manner. Combined with an inputted observation window timing sequence, these four constituents form the building blocks for the *navigation model*, which outputs an approximation of the annual ΔV. Through this system, it is possible to perform a comparison analysis of the station keeping costs associated with certain observation window configurations. The mentioned constituents will be elaborated upon in Section 4.3.2 until Section 4.3.5 and the their relation to the navigation model will be explained in Section 4.3.6. Additionally, the simulation framework allows one to optimize station keeping costs using the *optimization model* which contains a heuristic optimization algorithm that will use the ΔV outputs of the navigation model with the objective to minimize this parameter. This will be touched upon in Section 4.3.7.

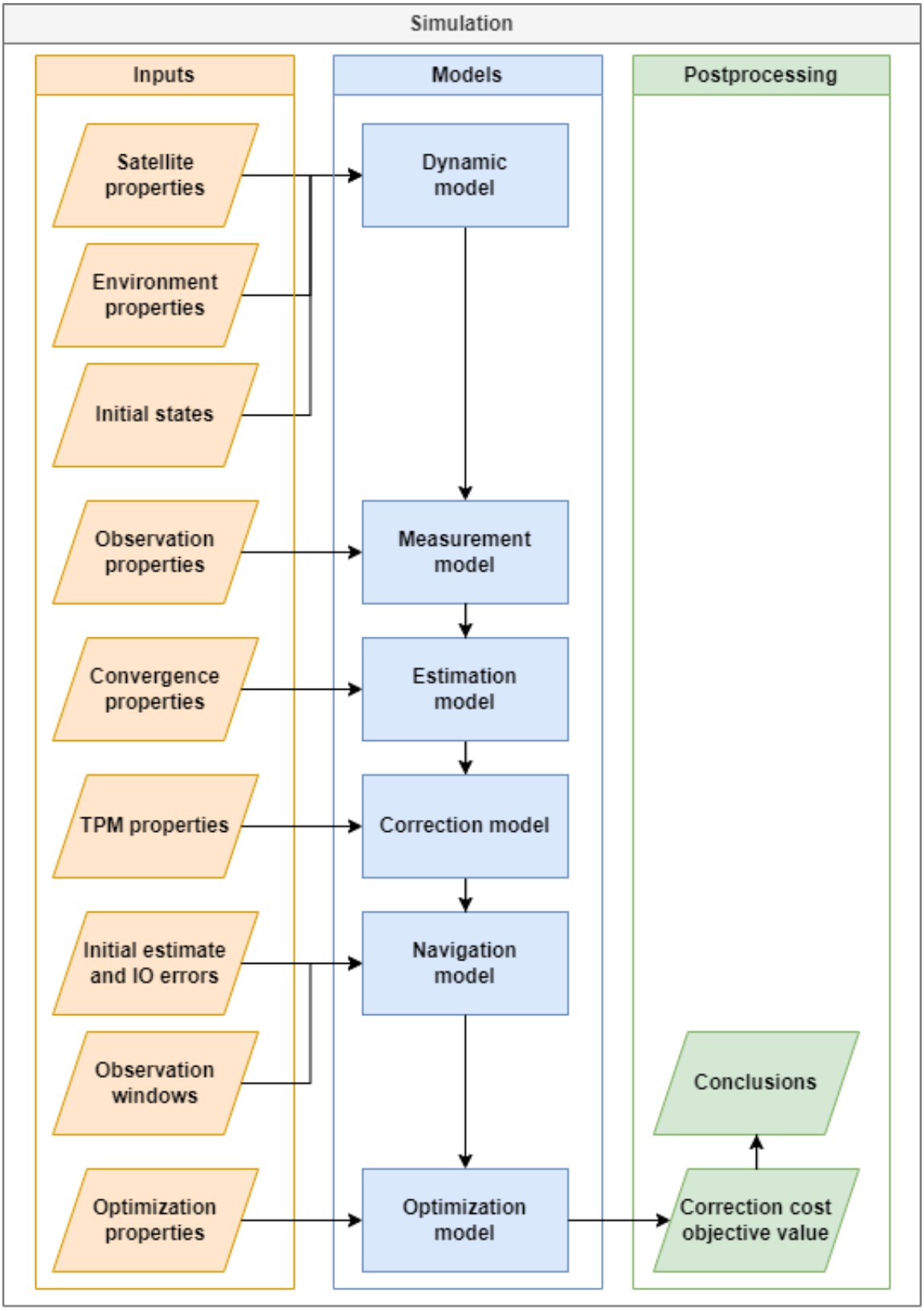

Figure 4.1: Schematic overview of the full simulation setup

4.3.1. Annual cost approximation

Due to computational constraints, the optimization model cannot cover the entire 1-year operational period. As such, an approximation has to be made of the annual cost. This is done according to the following formula:

$$||\Delta \boldsymbol{V}_{annual}|| \approx ||\Delta \boldsymbol{V}_{>14days}|| \left(\frac{365}{T_{duration} - T_{14days}} \right) \tag{4.1}$$

Here, $T_{duration} - T_{14days}$ refers to the time difference between the threshold time of 14 days since the start of the simulation and the total duration of the simulation. This means that for a total simulation duration of 28 days the relevant costs are those associated with the corrections that occur in a time span of 14 days. In the case that the total duration is 56 days, then the relevant costs come from a time span of 42 days. The $||\Delta V||$ after the threshold of 14 days is multiplied by a factor that scales the simulation value of the SKM cost to 1 year. The visualization in Figure 4.2 is used to explain how the results are shown in Chapter 5.

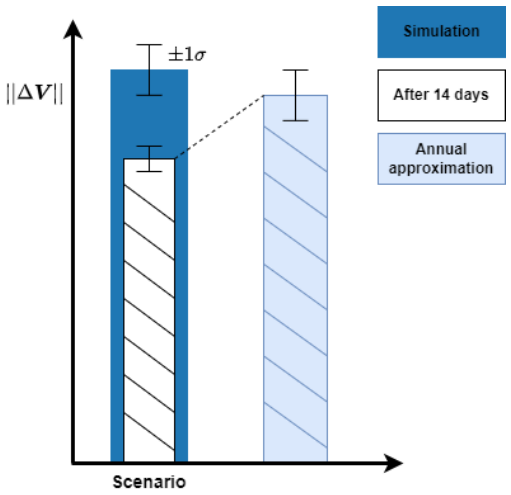

Figure 4.2: Visualization of the approximation of the annual station cost

4.3.2. Dynamic model

Initial states

The simulation work assumes that the LUMIO spacecraft starts at its scheduled time of 00:00:000 on March 21, 2024 or Modified Julian Date 60390. Previously, this date was the target date for when LUMIO was expected to begin its operational phase. Although this date has been delayed to a yet to be defined time, the start epoch is assumed to not be a limiting factor on the overall analysis. For ease, the spacecraft's states are shown in Table 4.2 with respect to the Earth-centered J2000 and non-dimensionalized Earth-Moon synodic frame, respectively. The three orbit types shown in this figure are explained in Section 4.3.2.2. Note the offset between the truth and the initial state of both LUMIO and LPF of 500 m and 1 mm/s. This represents the initial estimation error and can be found in Appendix A. The LUMIO reference orbit history is derived from data set explained in Section 4.1.2, defined at the earlier mentioned default mission start epoch of MJD 60390. Because no precise expected state history of LPF spacecraft is available at the mission start time, the states of LPF are derived from the lunar Keplerian states provided by Scotti et al. [121] as shown in Table 4.1.

State	Value	Unit
Semi major axis	5737	km
Eccentricity	0.61	-
Inclination	57.82	deg
Argument of periapsis	90	deg
Longitude of ascending node	61.55	deg
True anomaly	180	deg

Table 4.1: Initial Keplerian states of Lunar Pathfinder

	Inertial LPF		LUMIO			
State	**Estimated**	**Truth**	**Estimated**	**Truth**	**Reference**	**Unit**
x	-274751545.6	-274752045.6	-310468779.1	-310469279.1	-310469279.1	m
y	250414392.2	250413892.2	249476676	249476176	249476176	m
z	137232530.7	137232030.7	174974583	174974083	174974083	m
v_x	-503.2448066	-503.2458066	-993.4040049	-993.4050049	-993.4050049	m/s
v_y	-183.5823604	-183.5833604	-766.3354851	-766.3364851	-766.3364851	m/s
v_z	-297.1638318	-297.1648318	-524.9891151	-524.9901151	-524.9901151	m/s
	Synodic LPF		**LUMIO**			
State	**Estimated**	**Truth**	**Estimated**	**Truth**	**Reference**	**Unit**
x	0.970048539	0.970048179	1.062306657	1.062306297	1.062306297	-
y	-0.001916455	-0.001918478	-0.03735667	-0.037358694	-0.037358694	-
z	-0.013816446	-0.013816967	0.066320346	0.066319826	0.066319826	-
v_x	0.12284516	0.122842901	-0.018254046	-0.018256305	-0.018256305	-
v_y	-1.506863742	-1.506865024	-2.371789404	-2.371790686	-2.371790686	-
v_z	-0.183400182	-0.183400603	-0.118124416	-0.118124836	-0.118124836	-

Table 4.2: Initial states of the simulation in the inertial and synodic reference frames

Model classification
Different types of orbits should be considered for the estimation and orbit correction process. There are three different types of orbits that are relevant for the analysis. Each has its relevance in either the estimation or station-keeping. For a visual representation please see Figure 2.4.

- **True orbit**
  The trajectory that is used to simulate the true observations during the estimation process.

- **Estimated orbit**
  The trajectory prediction of the spacecrafts that is calculated on-board. Ideally, this model captures all possible orbital perturbations, but that is not possible due to constraints on computing power and systematic uncertainties of the physical world. The relevance of including certain perturbations is at the core of this work.

- **Reference orbit**
  The orbit that is used to define the planned trajectory throughout the mission. This trajectory is the state history from a continuation model as discussed in Section 3.1.4. Because of this, corrections shall be applied to the estimated orbit. How accurate this correction is depending on the accuracy of the orbit determination process.

These models have to be simulated by the dynamic model. Such a model can have different levels of accuracy, depending on the acceleration terms that are added in the equations of motion. For the sake of clarity, it is important to establish a consistent naming convention for the different types of dynamic model that are used. The dynamic models are divided into three groups: *low fidelity*, *high fidelity* and *full fidelity*. In total there are 34 models. In the order of the groups, this equates to 1, 32 and 1 respectively. The division is shown in Figure 4.3. The details of the exact accelerations can be found in Appendix A.

- **Low Fidelity**
  The most simplified case of the dynamics of the satellites, constituting a 3-body system, which is the CRTBP. This model contains a Moon ephemeris that is a circular orbit at an average distance of 384747.63 km to the center of the Earth.

- **High Fidelity**
  Describes the dynamics of satellites with a Moon ephemeris that is derived from the JPL DE405 ephemerides. The most basic model contains three point masses for Earth, Moon and Sun. Depending on the subgroup,

the complexity can be extended with more acceleration terms such as radiation pressure or various degrees of spherical harmonics. Additionally, other planetary bodies can be added. For computational efficiency reasons, spherical harmonics are only considered for Earth and Moon in this work.

- **Full Fidelity**
  The group with the largest complexity of dynamics and aims to capture the physical world as good as possible within the realm of the translational dynamics functionalities of *tudatpy*. The base of the model contains all acceleration terms of the most complex High Fidelity model. Additionally, the Schwarzschild, Lense-Thirring and de Sitter terms for relativistic terms are added. The solar radiation pressure acceleration term is extended by including the albedo from Earth and Moon using the surface panel method [122]. The albedo of the Moon is variable and defined by a 15 order and degree harmonics of the emissivity properties of surface of the Moon defined by Floberghagen et al [123].

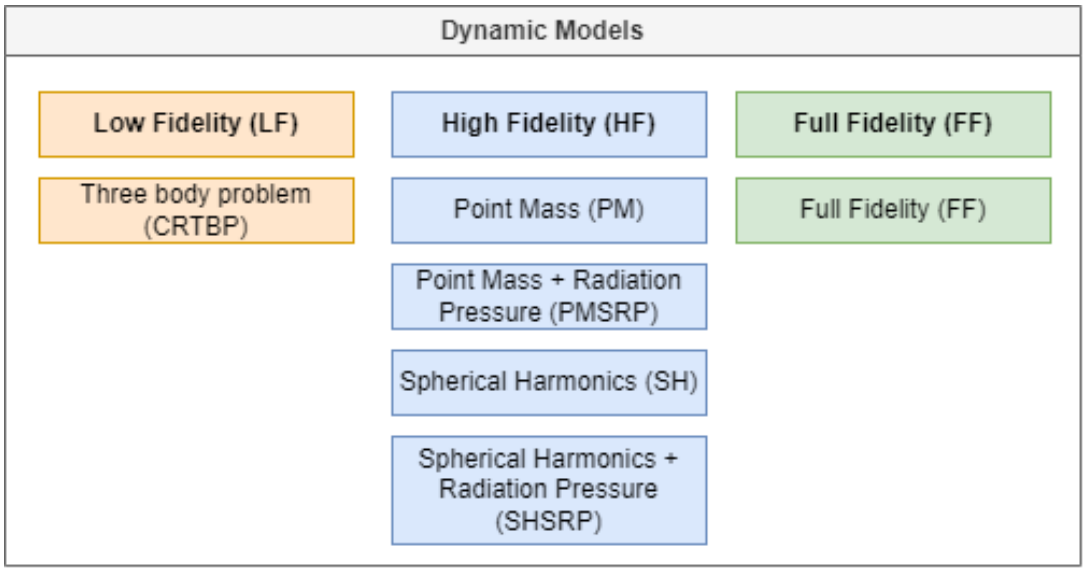

Figure 4.3: Classification of the dynamic models

4.3.3. Measurement model

The measurement model incorporates the principles explained in Section 3.2 for two-way range observables. Two-way ranging is chosen over one-way due to its better susceptibility to clock asynchronization compared to one-way ranging [124]. Naturally, the navigation system is susceptible to noise. Therefore, Gaussian distributed noise elements are added to simulate the behavior as a response to this stochastic nature. Table A.2 shows the standard deviation values associated with various noise terms expected in the real-world scenario. The noise uncertainty of 2.98 m 1σ is derived from the work of Turan et al. [11] and is assumed representative of existing pseudo-noise ranging systems [125]. Measurement errors are incorporated by means of defining two separate dynamic model objects representing a *truth orbit* and an *estimated orbit* as discussed in Section 4.3.2.

4.3.4. Estimation model

The estimation model utilizes a Batch-Least Squares (BLS) estimation algorithm and includes the concepts explained in Section 3.3. For this, specifically the estimation capabilities of tudatpy are used [84]. See Table A.2 for the overview of the values. The measurement frequency results from trial and error, between accuracy and run time. For any arc, only the initial spacecraft states are estimated, to reduce the overall complexity and to remove the need for an a-priori estimate of uncertainties and errors for other parameters that technically could have been estimated alongside, like gravitational parameters or the SRP reflectivity coefficient. The initial estimation errors are derived from the values used in the work of Turan et al. [11]. It is assumed that the initial estimation uncertainty values of Table A.2 are adequately realistic for initializing the navigation system on-board. At the start of the navigation routine, the state uncertainties are assumed to be uncorrelated, so the

state uncertainty matrix is a matrix with only squared values of the respective standard deviations along the diagonal.

4.3.5. Correction model

The correction model uses the Target Point Method (TPM) to calculate the SKM as touched upon in section Section 3.5.1. The default simulation settings incorporate only one target point, which is 3 days downstream after the cut-off. The choice of this duration is based on trial and error between accuracy and run time. A SKM is calculated after each arc, the corresponding ΔV is stored, and the orbit is adjusted accordingly. The maneuver occurs instantaneously, as defined in Section 4.2.

4.3.6. Navigation model

The navigation model can be described as the accumulation of a set of estimation arcs, or also known as observation windows. The arcs come from the estimation model. The purpose of the navigation model is to get the value of the total ΔV. The navigation model is in essence the objective function used in the optimization model, so it is the input to the final blue block as defined by Figure 4.1. The navigation model starts with a pre-defined initial estimation error, an a-priori covariance of the estimation error, and an insertion error at the start epoch. The covariance and estimation error initializes the BLS estimator with an initial guess and a-priori covariance. The insertion error refers to the initial difference between the *estimated orbit* and the *true orbit*. In a for-loop over the observation windows, it iterates through each arc and propagates the states based on the last information obtained from the latest arc. As explained in Section 4.2, a total duration of 28 days is considered. The values of the individual corrections that occur after 14 days are summed up and leads to the final objective value. See Table A.2 for more details on the values. A flowchart of the model is shown in Appendix B.

Default observation window

Based on the assumptions stated in Section 4.2, an initially ideal starting point for the tracking window configuration that satisfies the an ideal station keeping frequency based on literature [109], was chosen. These settings are shown in Table 4.3. This will be the absolute starting point for the optimization routine as will be discussed in Section 4.3.7.

Parameter	Value	Unit
Start epoch	60390	MJD
Arc length	1	day
Arc interval	3	day
Duration	28	day

Table 4.3: Default settings of the observation window

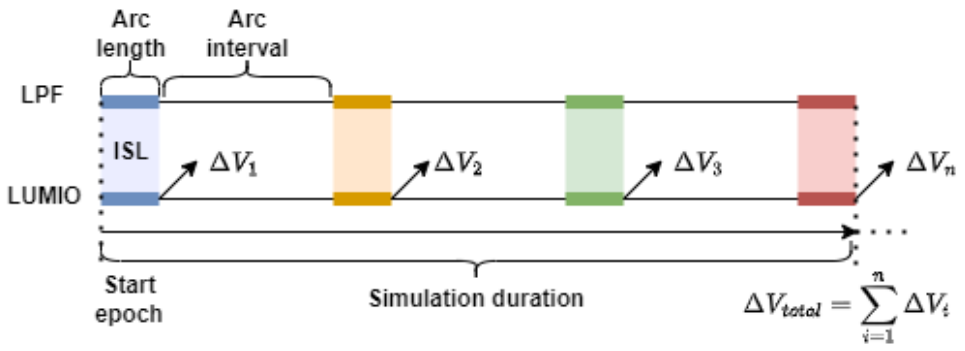

Figure 4.4: Observation window definitions

Error contributors

Orbit insertion errors are only considered for the states of LUMIO as LPF is assumed to be located at its reference trajectory at all times as mentioned in Section 4.2. For LUMIO, in practice, this value is assumed based

on a dispersion value found at the moment the spacecraft leave the rocket [126]. It is assumed that deviations from LPF's reference orbit are comparatively small to those of LUMIO in real scenarios. Because of that the effect of subsequent station keeping effects from the side of LPF are thus not considered. Like orbit insertion errors, station keeping errors occur only for LUMIO. The errors are defined in both magnitude and direction [126]. While the default case does in fact consider zero station keeping effects, a later sensitivity analysis will should to what extent these effects play a role on the total maneuver costs. Likewise, a zero-valued ΔV threshold is set, which defines the threshold of ΔV at which the propulsion system actually performs the correction due to technical limitations on minimum specific impulse or thrust. This is to accommodate potential lower limits associated with the performance characteristics of propulsion systems.

4.3.7. Optimization model

In the autonomous navigation framework, the total ΔV is the result of a complex coupled system, described by, but not limited to, the parameters explained in Section 3.7. The design space is spanned by the least amount of parameters to capture the effect of the varying observational geometry and station keeping epochs, while reducing the computational burden. The design vector $\boldsymbol{\alpha}$ contains only parameters describing the duration of an estimation arc. It is assumed that no cut-off time is present, so the SKM starts right after the arc. By the second constraint in Equation 4.2, the start of the next estimation arc should be at least 3 days after the latest SKM. By adjusting just the durations of the tracking window before a correction, one has not just control over the duration of the tracking windows, but also the consequent epochs at which the SKM occur. The optimizer looks for an optimal set of tracking durations, considering the cost associated with observing in certain dynamical regimes and delaying a maneuver at certain epochs.

$$
\begin{aligned}
\text{minimize} \quad & ||\Delta \boldsymbol{V}(\boldsymbol{\alpha})|| \\
\text{subject to} \quad & t_{OD,0} = MJD60390, \\
& t_{SKM,i} = t_{OD,i} + T_i, \\
& t_{SKM,i+1} = t_{SKM,i} + 3 + T_i, \\
& 0.1 \leq T_i \leq 2.0, \quad i = 1, 2, \ldots, n \\
\text{where} \quad & \boldsymbol{\alpha} = \begin{bmatrix} T_1 & T_2 & \cdots & T_n \end{bmatrix} \\
& \boldsymbol{\alpha_0} = \begin{bmatrix} 1 & 1 & \cdots & 1 \end{bmatrix}
\end{aligned}
\tag{4.2}
$$

For that reason, Equation 4.2 was chosen as the scheme. The 3 represents the constant arc interval of the default model settings. The upper and lower bounds are arbitrarily chosen. The navigation simulation runs a large set of computations based on many variables hidden within the dynamic and estimation models and thus not every optimization technique is feasible. Optimization methods must be used that can handle noisy non-differentiable solution spaces. In this study, two optimization method are compared for their ability to converge to a solution of the observation windows configuration defined by α.

Also, different durations and dynamic models are compared to see the effect on the optimization and approximation of the research objective of the annual station keeping cost. Figure 4.5 shows the relationship between the navigation model and the optimization model. Clearly, the optimization model feeds various candidate solutions for observation windows into the navigation model. Based on the estimation error and dispersion associated with the resulting evolution of spacecraft states and orbit corrections, a final objective value is outputted. Based on this, new candidate solutions are inputted, and the iterative cycle continues until a total of 40 iterations are done. This number proved to be a number at which most runs seemed to have converged most to a solution.

- **Nelder-Mead**
  The Nelder-Mead method, also known as the simplex algorithm, does not use gradient information from the objective, making it suitable for optimization situations in which the gradient of the function is unknown or cannot be fairly estimated [127]. An important aspect to note is that the Nelder-Mead method with this heuristic technique, which implies that solutions that are not guaranteed to be globally optimal but are sufficient for reaching a solution that improves the total maneuver cost. A disadvantage of the Nelder-Mead method is that it is known to be highly susceptible to converging to local minima and is sensitive to the size of the initial simplex. Literature suggest that increasing the size of the initial simplex and and the defining the shape of the simplex as a regular simplex is advantageous for

a limited-evaluation-budget case [128]. Another disadvantage is that the Nelder-Mean method suffers from poor performance in larger dimensions, also known as the *curse of dimensionality*. The algorithm's performance can degrade in high-dimensional spaces because the simplex can become distorted and collapse, leading to inefficient exploration of the search space [129]. Because of this, the choice of the initial simplex becomes more critical. A poorly chosen initial simplex can lead to slow convergence or convergence to sub-optimal solutions. In high-dimensional spaces, defining a good starting simplex is more complex and requires careful consideration.

- **Particle Swarm Optimization**
  The Particle Swarm Optimization (PSO) algorithm might yield better results and is less susceptible to the *curse of dimensionality* [69]. This method is inspired by the behavior of social organisms such as flocks or birds. It generates a population of particles, each representing a candidate solution, which move through the search space based on their individual velocity and the collective influence of the best solutions found by the swarm. The algorithm updates the states of the particles based on the objective value of the current solution of the particle itself and the global solution found so far. Through a balance of ”exploration” (looking for new solutions) and ”exploitation” (diving deeper into a good solution), the particles are encouraged to explore new regions of the search space while also following promising solutions [69]. The technique is another method to solve noisy non-differentiable objective spaces [69, 25]. While it tends to be more computationally intensive, it is able to find a global optimum more easily and is robust to a large set of applications [128]. It has been used before by Turan et al. in the context of tracking window optimization [25].

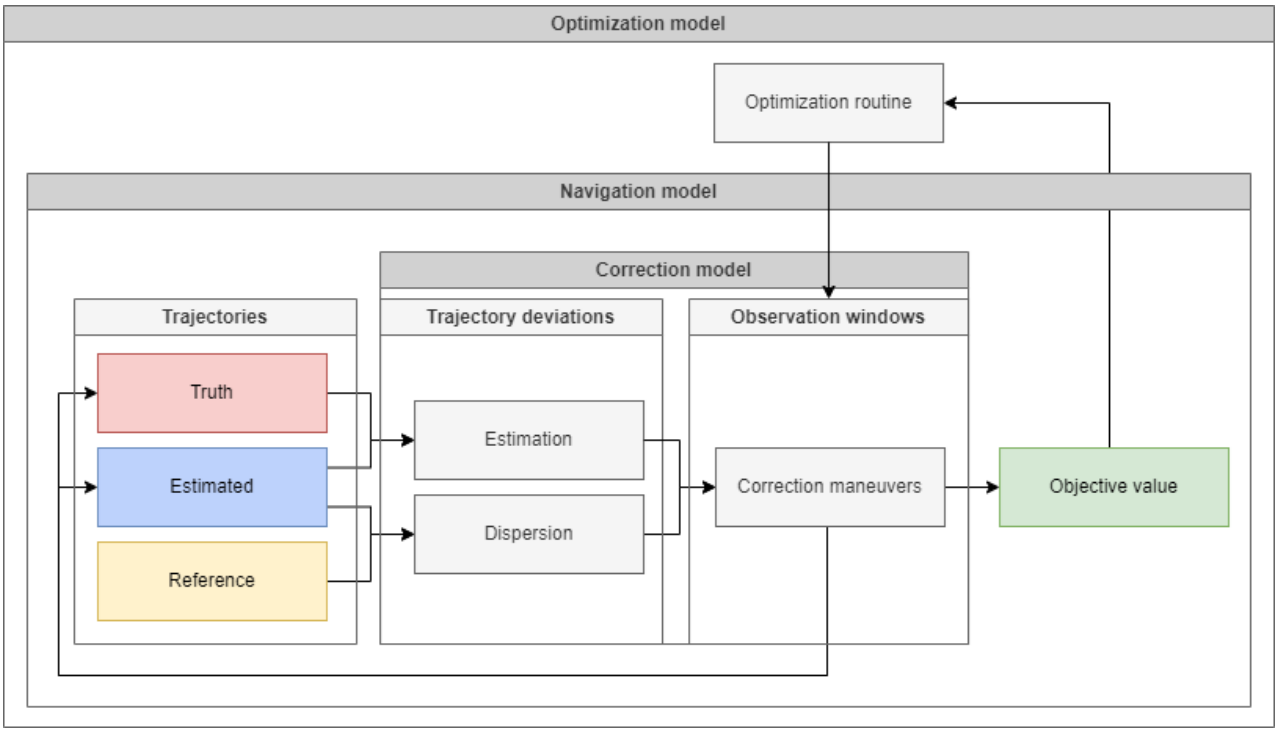

Figure 4.5: Structure of the optimization logic

4.4. Test setup

The goal of this section is to show the steps that will be taken to visualize the results from the constituents of the earlier mentioned models, see what model parameters affect the station keeping costs and finally the optimization results. In order words, the goal is to understand the mechanisms that occur in the process of orbit estimation, correction and tracking window optimization. The method is set up such that the results allow for a logical flow of the results. In Section 5.1, the aim is to define a final choice on the dynamic model that is considered on-board. With this model, a navigation analysis is done for an initial orientation of the results of the orbit geometry, observability and maneuver costs to visualize the navigation problem. This is one in Section 5.2. After this, a sensitivity analysis is elaborated upon in Section 5.3. Finally, Section 5.4 will state the goal of the final optimization.

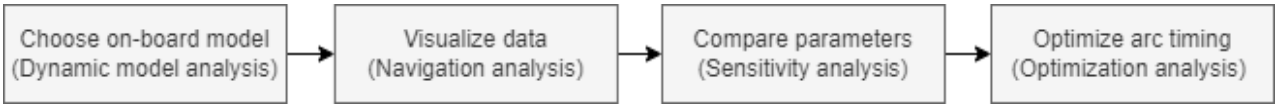

Figure 4.6: Methodology used for the analysis of the results

4.4.1. Dynamic model analysis

This work relies on the choice of the on-board dynamic model as it relates to the extent of computational efforts and accuracy of simulating the dispersion. These respectively affect the ability to find solutions and lower the difference to the reference orbit as much as possible to reduce the SKM cost. This means that it is beneficial if the same analysis can be conducted with more simplified models while being able to draw similar conclusions related to the expected maneuver cost [105]. The effectiveness of the maneuvers depends on the fidelity of the model. Additionally, if a dynamic model is better capable of simulating the reference orbit, then that will affect the maneuver costs positively due to the lower magnitude of the dispersion. In other words, the accuracy versus computation time relation allows for an assessment on the feasibility of the usage of the model in real missions, while taking the total duration of the design exploration on this work into account. So, the information on the total run time and the dispersion are considered to justify the usage of one particular model for the rest of the analyses conducted throughout this work. Note that in reality, the truth can never be known with absolute certainty. As explained in Section 4.2, this work assumes that the on-board dynamic model essentially perfectly simulates the true trajectory and that the only element of uncertainty comes from the noise of the measurements.

4.4.2. Navigation analysis

A lot of data comes with running the simulation. As part of an initial exploratory study, different tracking window cases are considered and their advantages and disadvantages are compared against each other. While this is not an optimization, it aims to show how different tracking window combinations can have different outcomes.

Default scenario

First, details of the default simulation scenario as shown as elaborated extensively in Section 4.3 are shown. Simulation outputs are shown which aims to relate it to the theory on observational geometry, observability, state uncertainty, dispersion and the resulting annual ΔV. The purpose of these results is to show the relations that exist between these parameters and to establish some broad conclusions on the overall workings of the navigation model without necessarily going into the exact optimization of the tracking windows yet.

Candidate scenarios

As part of an initial exploratory study, different tracking window cases are considered. These can be classified with increasing complexity. The objective is to compare the benefits and drawbacks associated with these scenarios. A separate chapter, Section 5.4 is allocated to discussing the results of the last item due to its complexity and nuances.

- **Constant arc duration**
  This case performs tracking windows at a constant duration, but with a pause between different arcs. Different combinations of arc interval and duration are considered and compared.

- **Arcs based on specific region of orbit**
  This case contains arcs that occur specifically in certain regions in an orbit that are shown to be the most relevant for state observability. As was explained in Section 3.4.2, regions of faster dynamics (perilune) yield larger observability for position states and lower observability for velocity states and the opposite is true for apolune. Perhaps it is more beneficial to perform tracking sessions at perilune or apolune to see if this alleviated level of observability in such a orbit region can yield a positive effect of the overall orbit determination and, consequently, navigation results.

- **Variable arc duration**
  Each arc length is adjusted individually such that the length is not constant. In this case, the solution space is explored in which certain combinations of tracking sessions make use of a better combination of state observability and thus provide better estimation errors and more accurate SKMs.

4.4.3. Sensitivity analysis

The simulation contains a lot of parameters that can be adjusted. These could be related to the observation windows, such as arc lengths, or auxiliary parameters such as station keeping error or observation noise level. Some might lead to more effect on the total ΔV than others. The sensitivity analysis aims to provide an overview of the parameters that are most critical to the station keeping reduction. In order to separate the parameters related to the observation windows from the auxiliary parameters, it is split into individual sections. The exact parameters and their values will be touched upon in Section 5.3. Only one parameter will be changed, so the rest remains the same with respect to the default case as described in Section 4.3.

4.4.4. Optimization analysis

In this final step, the optimization model, with the optimization problem definition discussed in Section 4.3.7, is employed to define the optimal window. This will initially be based on the settings of the default simulation setup, as shown in Table A.2. A short sensitivity analysis is done on the optimization model results as well to see if the final window configuration depends significantly on the inputs of the optimization routine.

5

Main results

Based on the simulation structure and workflow described in Chapter 4, this chapter aims to provide the results belonging to the steps and methods mentioned in the previous chapter. This chapter is split up such that different scenarios are compared in a systematic manner. Section 5.1 shows the influence of using a variety of on-board dynamic models. The best model derived from this chapter forms a baseline for the calculations of the navigation and optimization models. Section 5.2 elaborates on the navigation analysis, in which various aspects of the navigation model are shown for the default settings. Then, Section 5.3 provides an overview of the effect of changing many model parameter on the total SKM costs. Section 5.4 shows the results from the optimization model. Finally, the operational benefits associated with the improved tracking configuration is touched upon in Section 5.5.

5.1. Dynamic model analysis

The force model details for each dynamic model can be found in Appendix A and more information in the classification of the model was done in Section 4.3.2.

5.1.1. Initial uncorrected trajectory

Figure 5.1 shows the trajectory using an uncorrected PMSRP01 on-board dynamic model (for details, see Appendix A). The figure shows how the uncorrected trajectory of an example scenario starts following a typical LPO shape, but the unstable nature of the L2 orbit leads LUMIO to drift away from the orbit to eventually gravitate towards the Moon. It clearly shows the need for a set of corrective maneuvers within a 28-day period to be able to sustain it's 1 year operational lifespan as significant diversion starts to occur over a bit more than one halo orbit already. While the duration considered in Figure 5.1 is 35 days, the wrong trajectory is a direct consequence of not performing corrections earlier, so within the 28 days considered in the simulation cases.

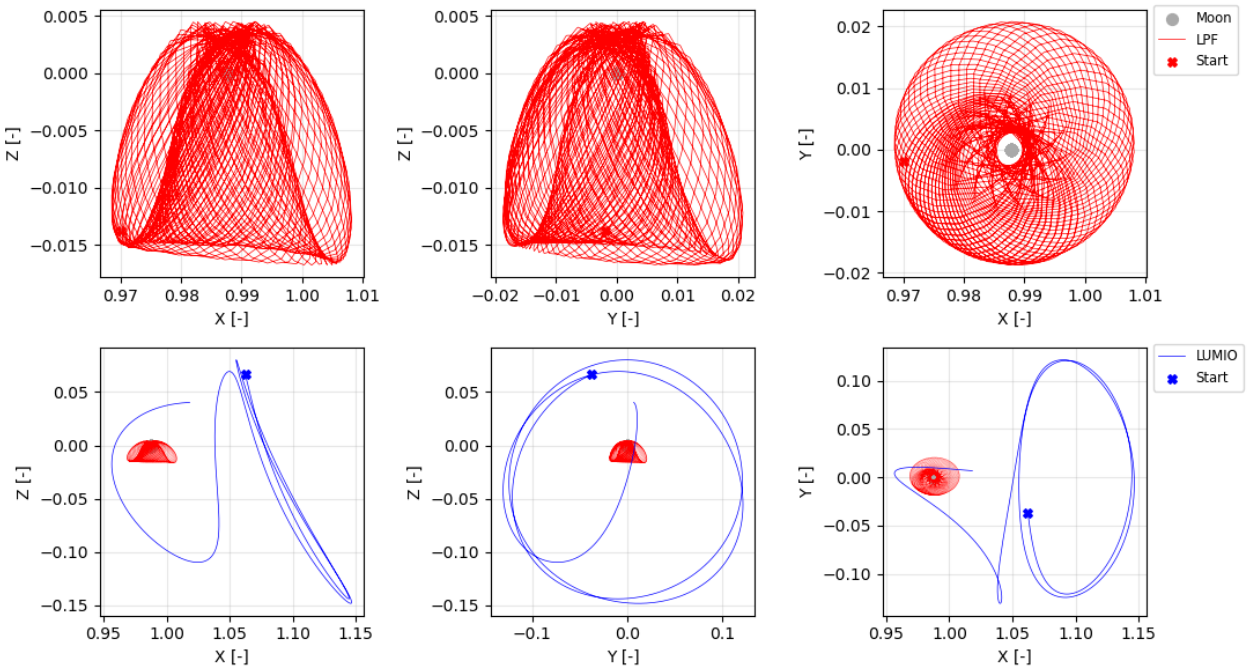

Figure 5.1: Reference trajectories versus uncorrected trajectories over 35 days

5.1.2. Run times

Figure 5.2 shows the run times resulting from propagating the respective models for one day. It is the result of a Monte Carlo analysis, in which 50 runs were performed with varying start epochs that occur between 60390 and 60404 to see the effect of the variation of orbits on the run time. The propagation time of exactly 1 day was chosen to allow for easy time scaling to other propagation times under the assumption of an equal propagation time to run-time ratio. Observe the exponentially increasing run time with model complexity. The CRTBP yields the smallest run time with a mean run time of 0.8 s. This small value is expected, because it does not consider any other terms than the point masses of the Earth and the Moon. Considering an additional point mass gravity of the Sun, which is included in all models besides CRTBP, already triples the total run time in the best case (PM01 and PMSRP01 models) to approximately 4 s. Including solar radiation pressure does not seem to increase the run time noticeably. On the other hand, including spherical harmonics terms drastically increases the total run time to a best scenario of 15 s for SH and SHSRP. Running a full-fidelity model yields an additional order of magnitude increase to approximately 200 s. In terms of run time, it seems beneficial to use a PM-type model with or without SRP. Section 5.1.3 should show whether to choose PM or PMSRP based on the expected dispersion with respect to the reference trajectory.

As was explained in Section 4.2, it is assumed that there is no cut-off time. This also implies that the state uncertainty growth is negligible between the ending the estimation arc and the correction. Assuming the PMSRP01 model, statements can be made related to the operations of the correction maneuvers. Given a TPM with one target point 3 days ahead, as touched upon in Section 3.5.1, the total time to calculate a maneuver using this method (and thus the cut-off time) is $4 \cdot 3 = 12$ s. Note from Figure 5.2 that a CPU with a clock frequency of 2.2GHz is used. LUMIO uses the AAC Microtec Sirius as On-Board Computer (OBC) with a 50MHz clock frequency [4, 130]. Even though this processor would theoretically increase the run time by a factor of $2200/50 = 44$ to 528 s, it is still small compared to the period of LUMIO or a tracking arc. It is also quite small compared to the cut-off of 12 h that is currently considered for LUMIO [4]. The run time calculations show that that this 12 h time window is not required in the scenario of AOD, making corrections more accurate.

Performing these correction calculations also would not take a lot of power. With a mere power requirement of 1.3 W, the total energy consumption of the OBC would equate to $1.3 \cdot 528 = 686.3$J. For reference, LUMIO's radio transponder has a power requirement of 94.4 W [131], which means that the correction calculations themselves have limited effect on the power budget.

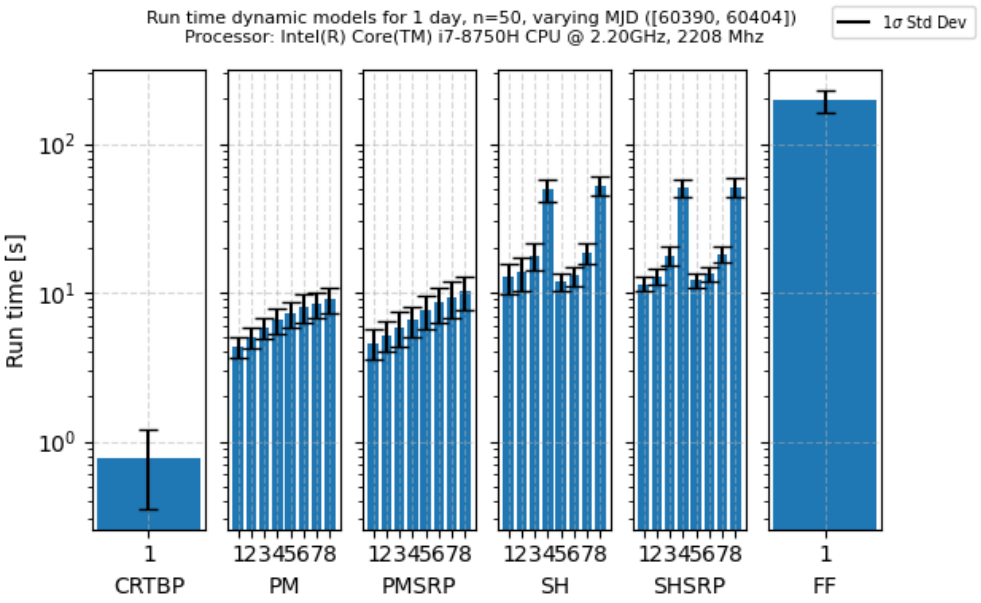

Figure 5.2: Run time values for various dynamic models

5.1.3. Dispersion

The degree of dispersion between the on-board and reference model affects the total station-keeping costs [8]. As such, the aim of this section is to obtain insights into what is the best dynamic model in terms of lowest dispersion. Based on the values shown in Figure 5.3, a judgment can be made on what model is drifting the least from the intended reference trajectory as was touched upon in Section 4.1.2. With the combined information on run time and dispersion growth a trade-off can be made on the overall best on-board model. Figure 5.3 shows the RMSE over a period of approximately one LUMIO orbit: 14 days. It can be seen that models that include SRP terms generally perform better. Dispersion values tend to decrease with increasing model complexity. CRTBP systematically performs the worst with an RMSE of $1 \cdot 10^8$ m. This is expected as there is always a large offset as a result of the assumption of constant Earth-Moon distance. Then, the PM- and SH-type models produce errors which are three orders of magnitude lower at $1 \cdot 10^5$ m. The same models, but including SRP offers another order of magnitude improvement by having a value of approximately $8 \cdot 10^3$ m. It is clear that incorporating spherical harmonics terms does not seem to improve the dispersion. Computationally, using spherical harmonics instead of point masses does not improve maneuver cost in a significant way, while it does significantly increase total run time. The same could be mentioned about the addition of other celestial bodies, albedo and relativistic effects added in the FF model, which clearly offers no noticeable dispersion benefits. On the other hand, including SRP offers much more improvement in dispersion with negligible increase in run time. Again, the PM-type model with SRP performs best and due to the negligible influence on dispersion caused by other planetary bodies, the simplest version is chosen to be used throughout this work: PMSRP01. Again, for details on the dynamic models, please visit Appendix A.

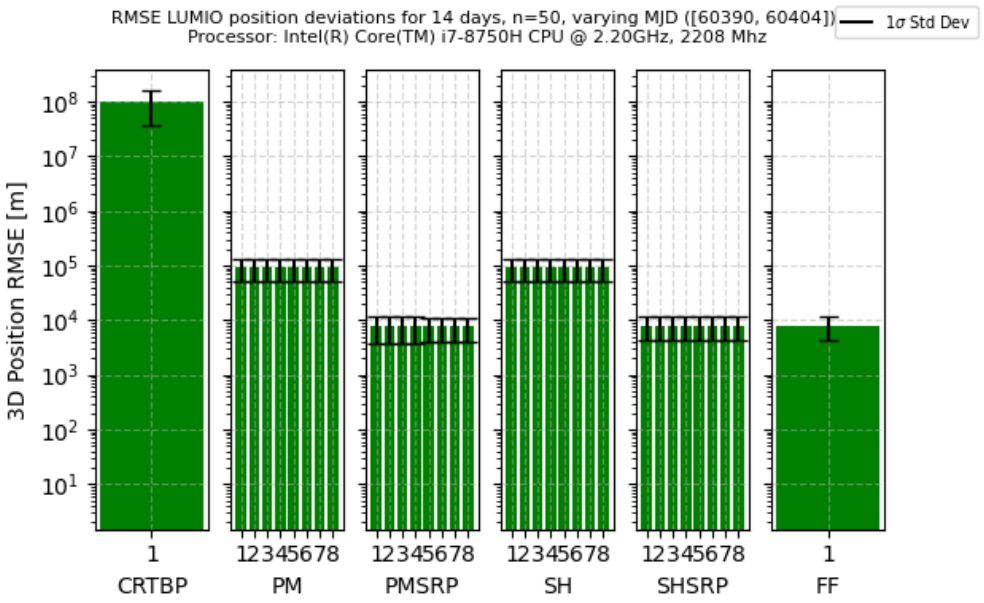

Figure 5.3: Position dispersion RMSE values for various dynamic models

5.1.4. Acceleration terms

Figure 5.2 and Section 5.1.3 show the run time and dispersion result caused by different dynamic models, but one can also look specially into the model constituents to deepen the understanding of the relevancy of each included acceleration term. the the Looking into the accelerations will provide a clue into the relevance of including certain force terms into the simulation. Figure 5.4 and Figure 5.5 provide additional information over Section 5.1.2 and Section 5.1.3, because it allows to systematically assess the effect of individual accelerations and thus allows one to quickly see which term would actually be relevant to include in a dynamic model.

The peak values in the total accelerations in Figure 5.4 occur at perilune passes. As expected, the most predominant terms, in order to larger to smaller, are: point mass Moon, point mass Earth, radiation pressure directly from the Sun. While the J2 and J2,2 terms are relatively large in magnitude, the point mass terms of all planets, albedo, relativistic effects and the spherical harmonics of Earth are negligible. This suggests that the usage of a point mass model of Earth, Moon and Sun + SRP should also provide a sufficiently accurate depiction of the realistic scenario. With Figure 5.2 in mind, excluding other planets and spherical harmonics also saves a lot of computational cost with limited loss of realism. The acceleration terms related to LUMIO are prone to a lower extent of variation. However, it is clear that the reduction in gravity terms from the Moon intuitively are the main contributors to the reduction in magnitude of the overall acceleration.

Finally, the found results allows one to assess the correspondence of the calculations done earlier by T. Tanis [29] which were based on the same dynamic model parameters. Indeed, the shape and magnitudes in Figure 5.5 and Figure 5.4 are the same as shown in the thesis report of T. Tanis. Additionally, the dip in SRP from the Sun seen in Figure 5.4 just after day 4 corresponds nicely with the results found by T. Tanis. This seems to be the only region in which occultation occurs as a result of the Moon blocking the sunlight reaching LPF.

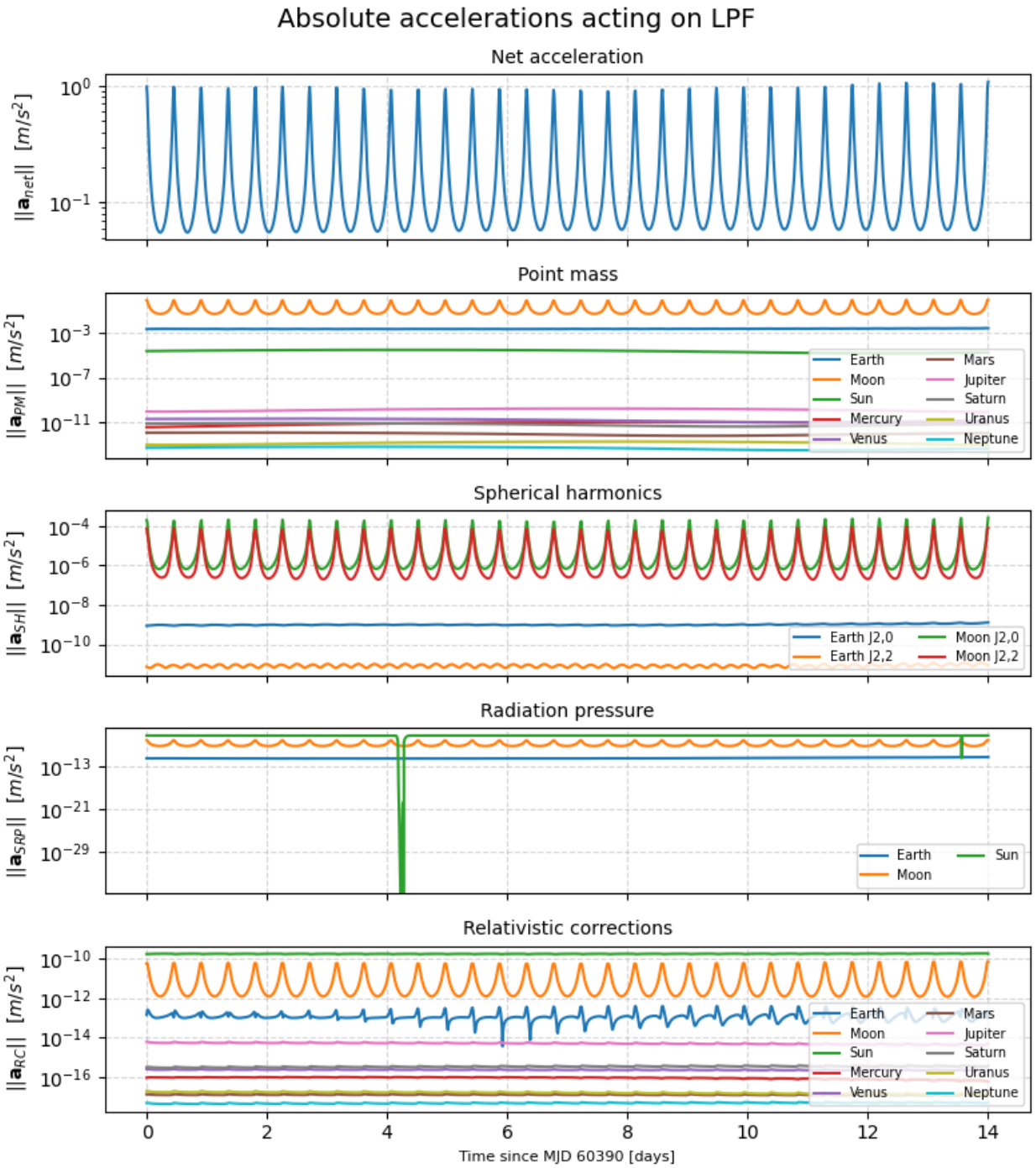

Figure 5.4: Norm of acceleration terms acting on LPF

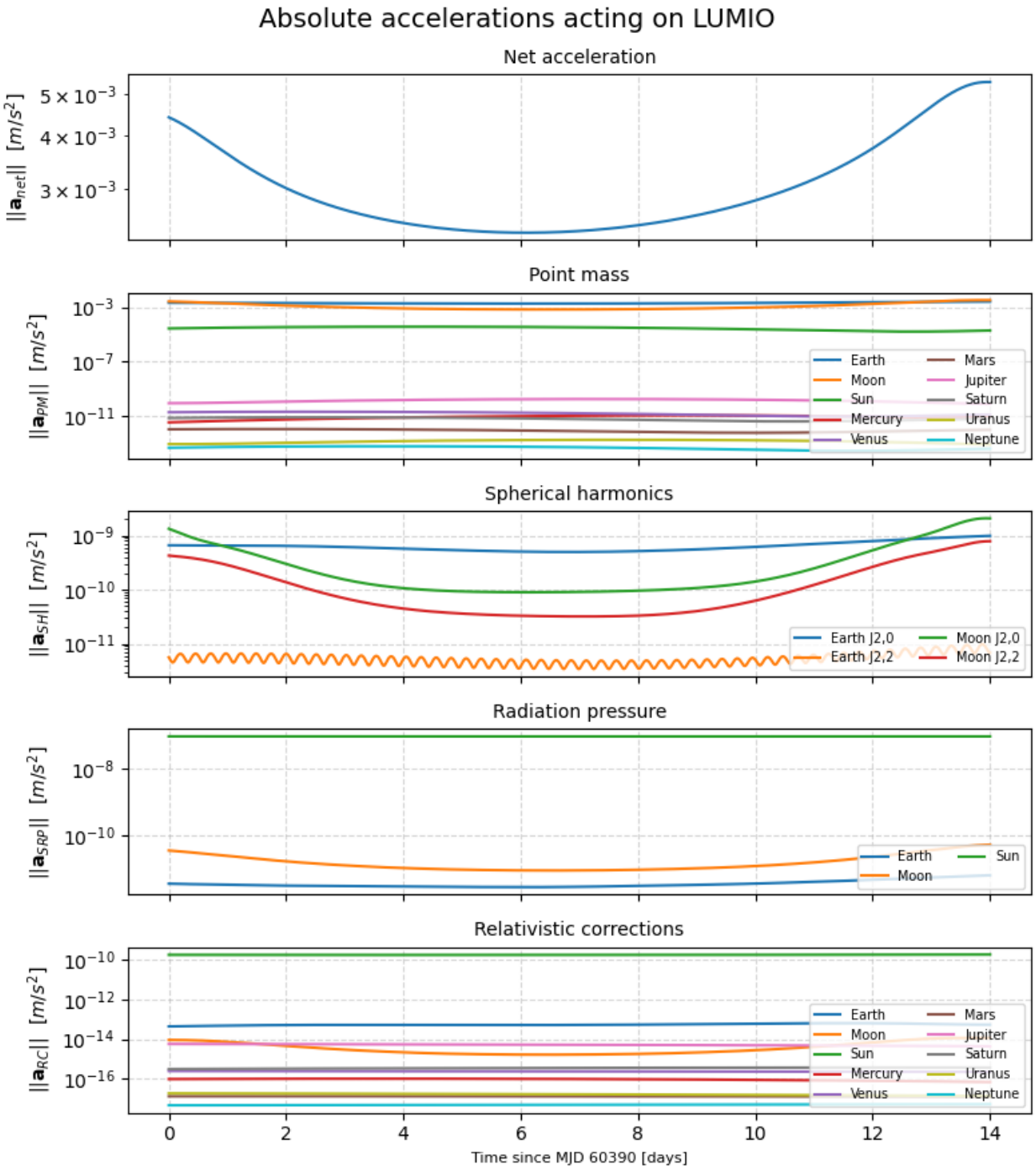

Figure 5.5: Norm of acceleration terms acting on LUMIO

5.2. Navigation analysis

Chapter 4 introduced the baseline scenario for the simulation settings with the default observation window settings as was shown in Table 4.3. Section 5.1 led to a final choice on the model that will be used for the remainder of this work. This information is now combined to show information associated with the OD and SKM process for the default observation window scenario.

5.2.1. Default scenario

Orbit geometry

Figure 5.6 provides a graphical representation of the observations that occur over a period of 28 days. The arrows represent the magnitude and direction of the maneuvers. Note how the geometry explored by LPF neatly distributes over time. Additionally, note how an arc duration of 1 day captures the geometric diversity gained over a bit more than 2 LPF orbits. This suggests that an arc duration of 1 day likely provides more than enough geometrical information to sufficiently converge the estimator to an improved solution for the state estimate. As such, this could suggest the possibility of reducing the duration of each arc.

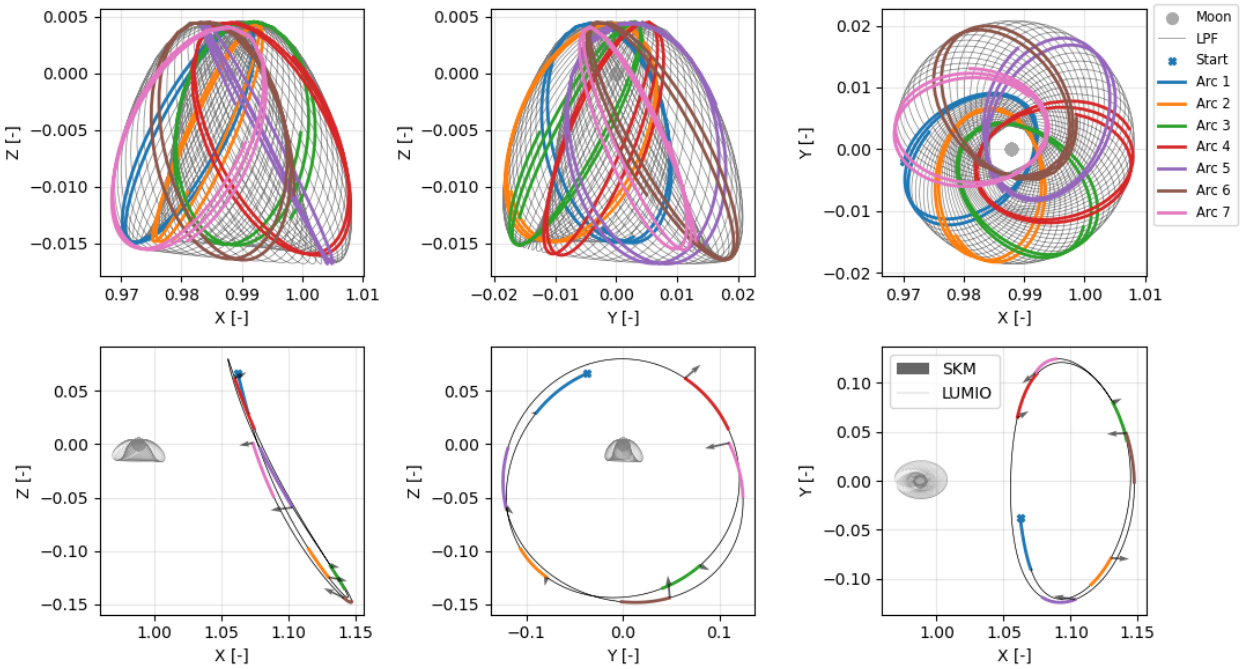

Figure 5.6: Overview of estimation arcs of the default scenario in 2D synodic frame

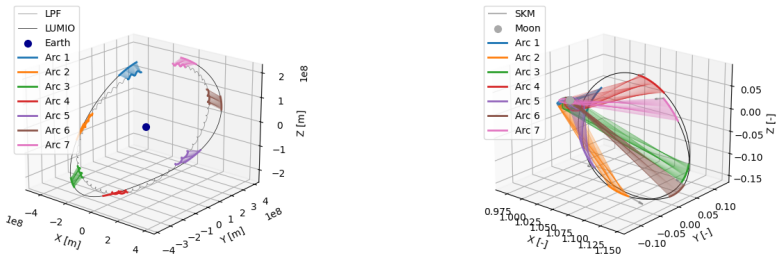

(a) Inertial frame **(b)** Synodic frame

Figure 5.7: Overview of estimation arcs of the default scenario in 3D

Covariance analysis

Covariance is a measure of the uncertainty associated with the estimation of the true value of the states of the satellites. Throughout the estimation process, the evolution of the estimation errors varies based on the initial estimation error that is given at the start of the simulation and the relative geometry of the spacecrafts. The covariance is thus a statistical representation of the distribution of estimation error outcomes given random draws from an initial distribution of estimation errors. While Monte Carlo simulations can be performed, the same result could be obtained via covariance analysis. Here, the covariance is propagated using the *a-priori* covariance given in Table A.2, which serves as the initially considered uncertainty associated with the estimated states.

Figure 5.8 indicates that the uncertainty of any position of velocity states in the system converges to almost noise levels. This is also the case for the individual components. Given the 3σ bounds, the probability is 99% that the estimation error of a position or velocity state resides within these bounds. The periodicity of the LPF-related errors matches with the period of its orbit of approximately 0.45 days. Note the logarithmic scaling, indicating a rapid convergence of the values. After 14 days, the 3D 3σ RSS estimation uncertainties have already reached a lower bound. Keep in mind that the model does not assume systematic errors, so the only contributor to the uncertainty is the measurement noise. Figure 5.9 shows the same for each state separately, indicating that all states are able to be estimated to similar levels.

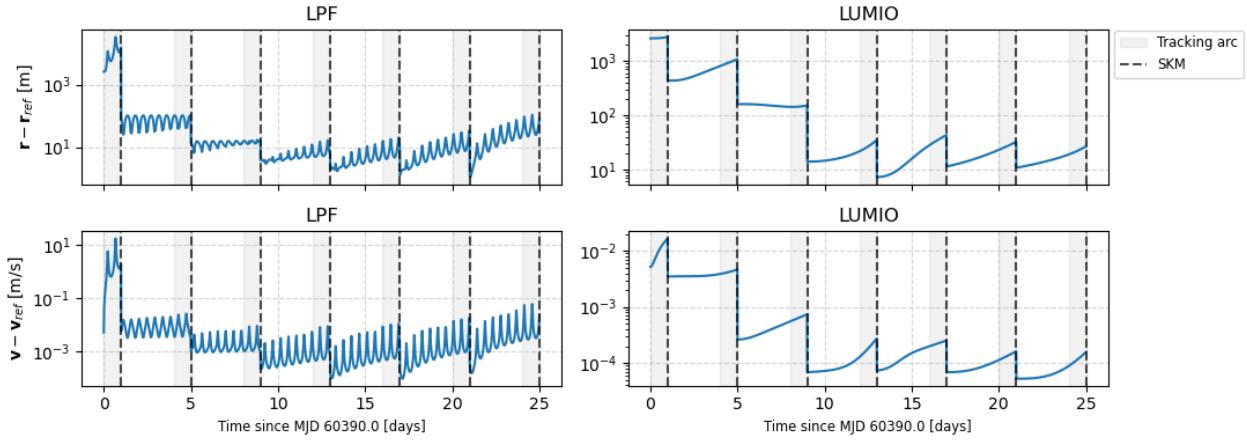

Figure 5.8: Total 3D 3σ RSS estimation uncertainties history of the default scenario

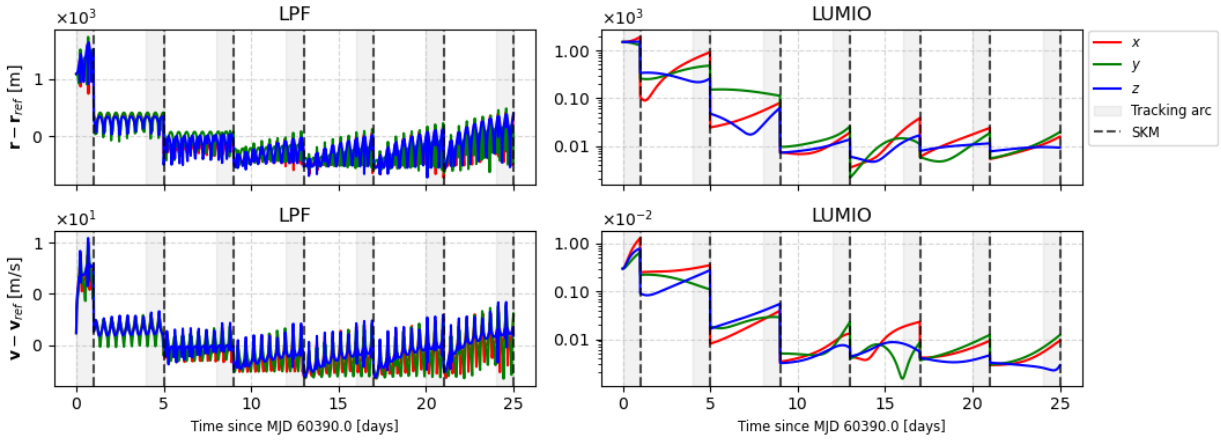

Figure 5.9: Total 3D 3σ RSS estimation uncertainties history of the default scenario decomposed by individual state

Estimation errors

As discussed in Section 4.3.6, the two orbit related errors are estimation error and dispersion. The rapid convergence is also clear from the history of the estimation error itself. Figure 5.10 shows the 3D RSS solutions. Clearly, the estimation error after a few tracking arcs is 2 to 3 orders of magnitude smaller than the initial error. Figure 5.11 shows a similar convergence pattern for all state estimates separately, suggesting that the estimator is able to find better solutions for the state estimates for each state and therefore shows that it does not lack observability for one or more states. This confirms that the LPF-LUMIO constellation is an excellent example to incorporate AOD with.

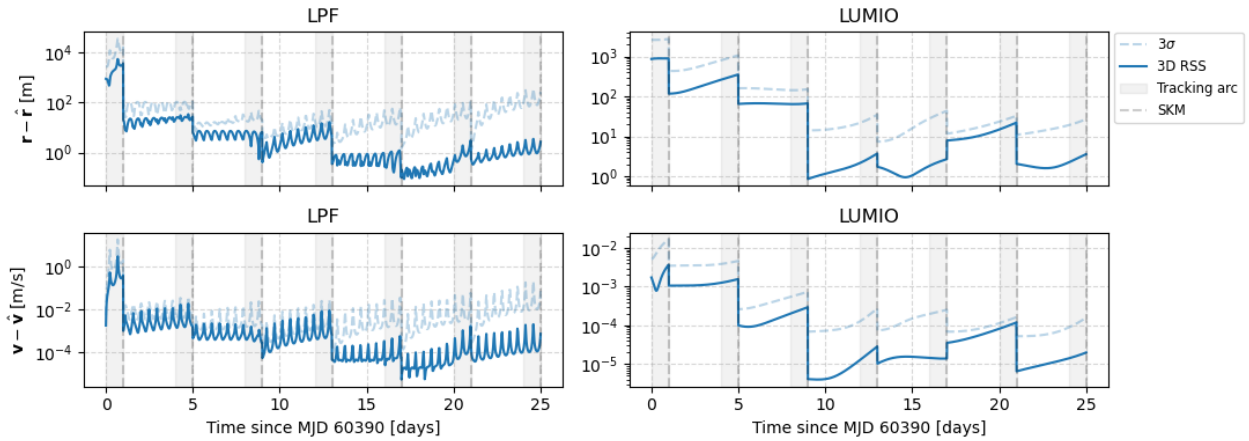

Figure 5.10: Absolute 3D RSS estimation errors

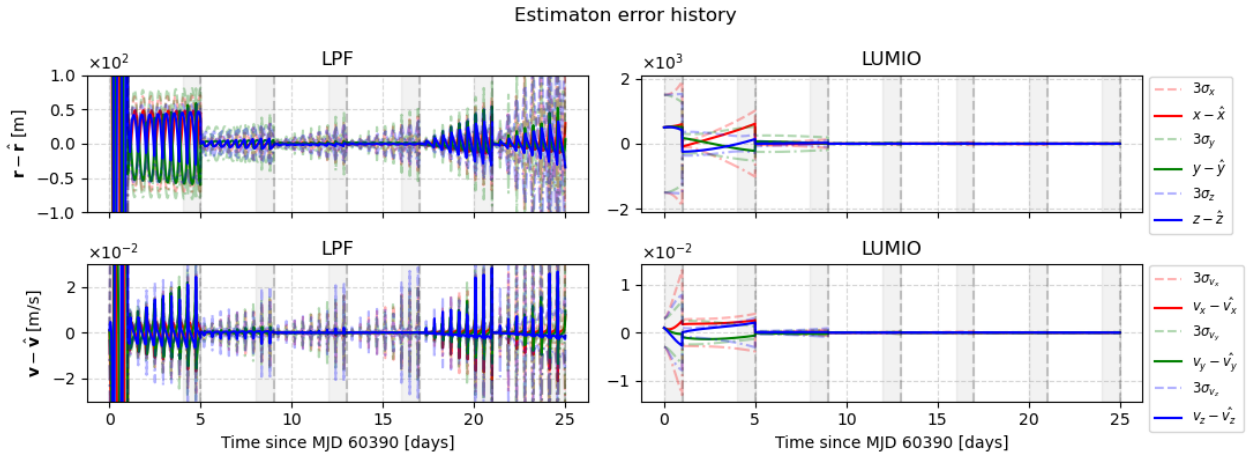

Figure 5.11: Estimation error history for default case

Dispersion

The dispersion is shown in Figure 5.12 as the difference between the *estimated trajectory* and the *reference trajectory*. Besides, Figure 5.13 shows it as the difference between the *true trajectory* and the *reference trajectory*. Note that the former is the best-known dispersion on-board. The latter is the true dispersion. It is important to note that the the station keeping cost depend on the dispersion that is known at a moment on-board [70], which means that the corrections are based on the dispersion of Figure 5.12 rather than Figure 5.13. In Figure 5.12, at the start, a 500 m error comes from the initial estimation error. Similarly, a 1 mm/s velocity discrepancy can be found in the velocity states. The model details can be found in Appendix A. Once the first estimation arc is done, the newly updated trajectory is used to define the newly expected dispersion. This information is the input to the correction model as its estimated states are the best knowledge that LUMIO has and is thus the most accurate knowledge to perform correction calculations with. Note how the jumps after each arc are smaller over time, caused by the decrease in estimation error. As such, Figure 5.12 ends up nearly the same as Figure 5.13.

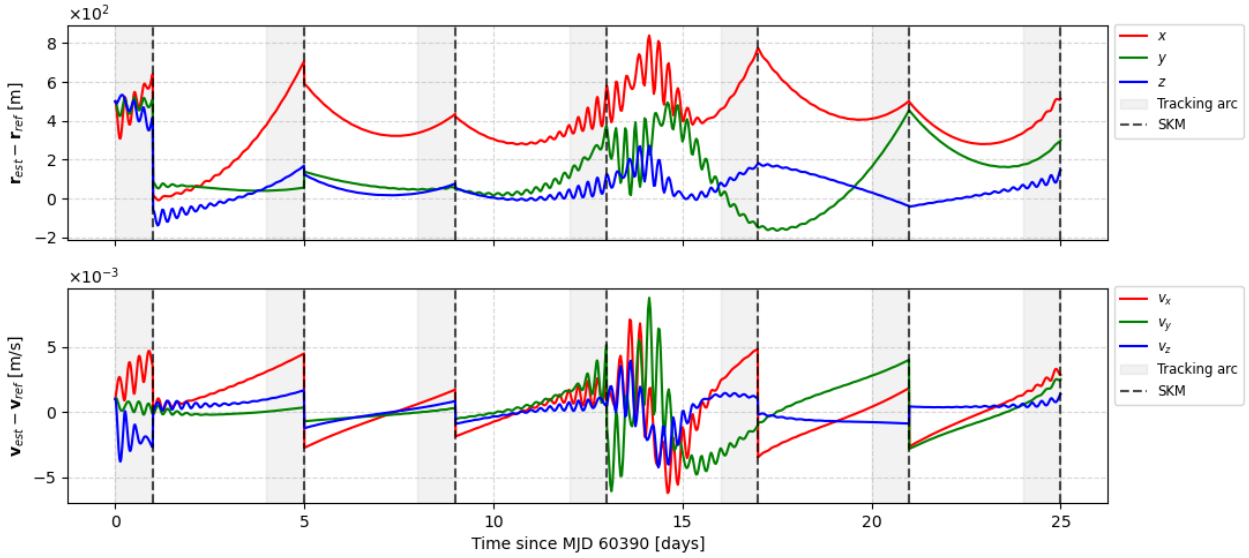

Figure 5.12: Dispersion of the estimated and reference LUMIO states

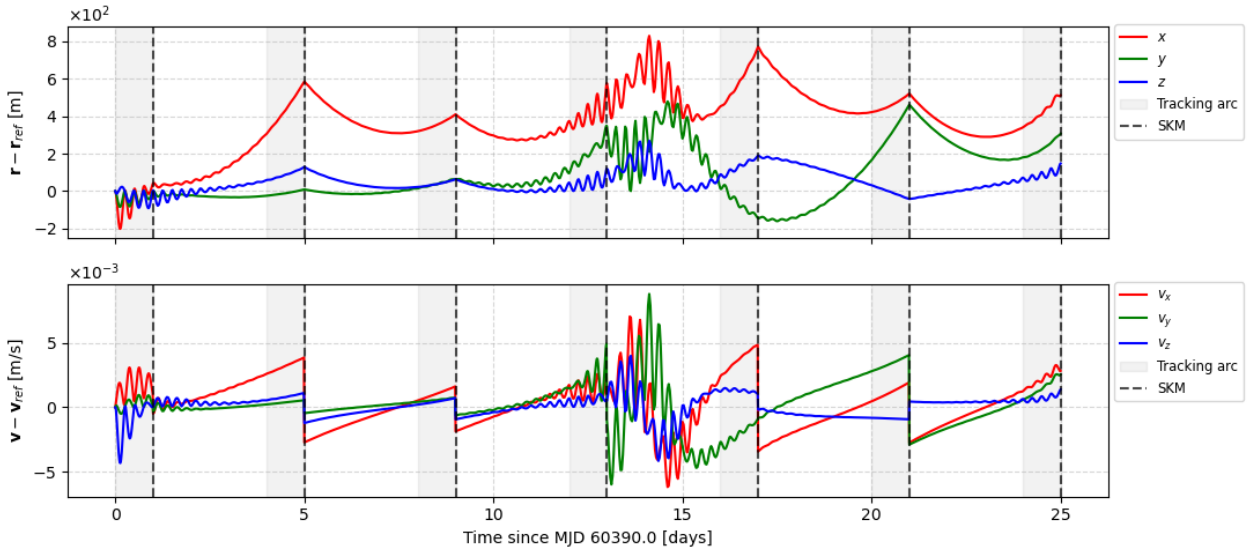

Figure 5.13: Dispersion of the truth and reference LUMIO states

Since the estimation error and dispersion are both contributors to the total ΔV, it is of interest two see how these two parameters change in magnitude, and thus relevance, throughout the navigation process (as defined by the *navigation model* explained in Section 4.3.6). Figure 5.14 shows how the 3D RSS position and velocity estimation and dispersion errors vary over time. Clearly, for position, the estimation error resides around the 10 m, while the dispersion tends to hover around the 500 to 800 m range and is thus consistently larger than the estimation error. A similar trend is clear for velocity. From this, one can state that the effect of estimation error itself has less of an effect on the ΔV than the dispersion does.

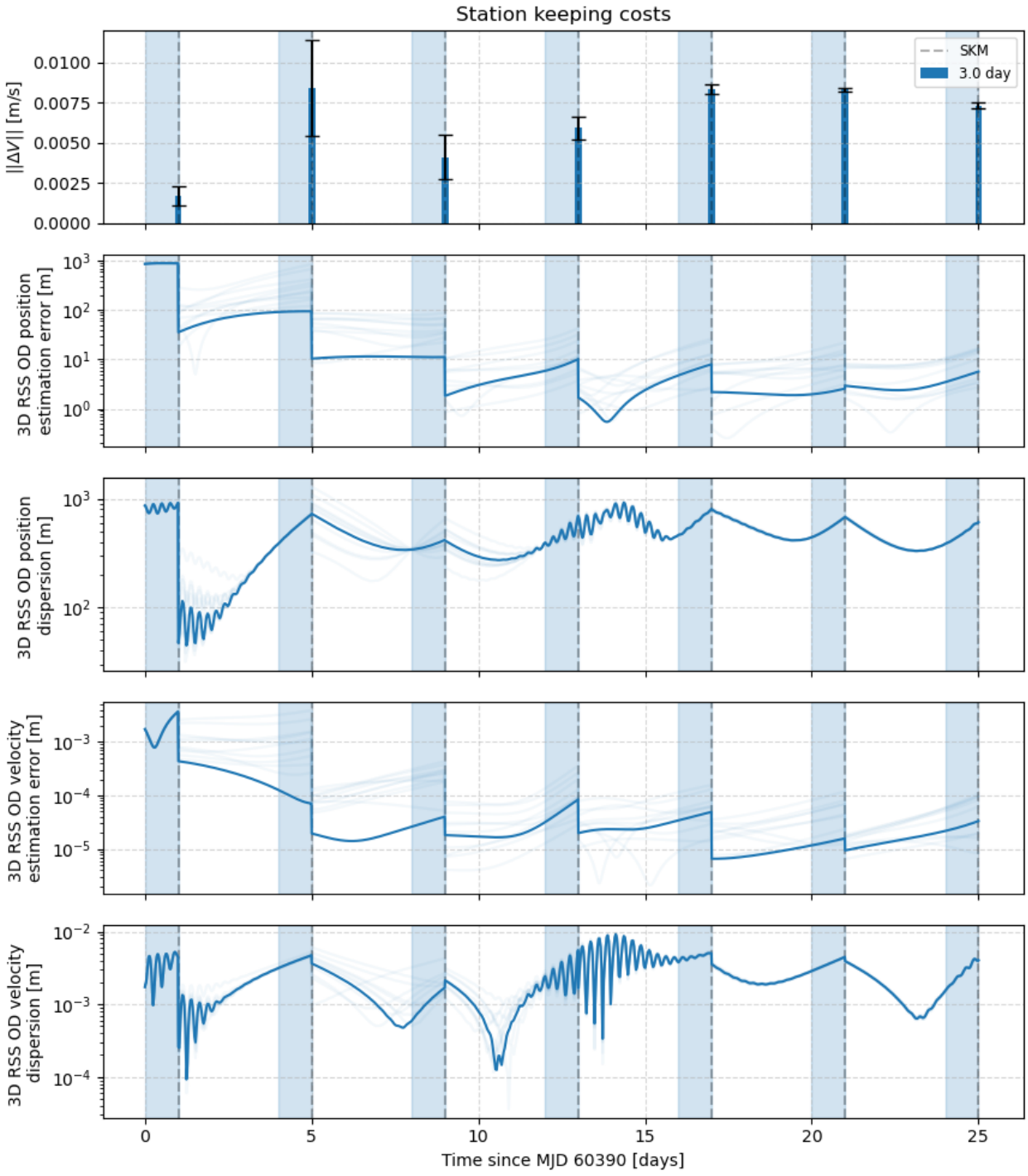

Figure 5.14: Individual SKMs with corresponding contributors' estimation error and dispersion

State correlation

As mentioned in Chapter 3, the estimation error covariance of the two spacecrafts should become coupled as the duration of the estimator fit span progresses. Clear correlations are visible between the position states of both satellites in Figure 5.15, which is a before-after depiction of the *a-priori* and estimated matrix at MJD 60390, respectively. It thus shows the result of the first arc of the default scenario with a duration of 1 day. While initially uncorrelated, the additional observations lead to a strong correlation mostly between a few specific states. For example, the state x_1 shows a strong proportional relationship with the z_1 and $\dot{x}_2$. Similarly, a strong positive relationship exists between x_2 and z_2. These relationships are challenging to intuitively make sense of as it depends not only on the direction of the observations, but it also varies with the specific orbital location of LPF through the STM. Nonetheless, it seems that there exists a strong positive correlation between the x and y states of the same spacecraft. Inversely proportional relationships exist between them as well and can be read off in the same fashion.

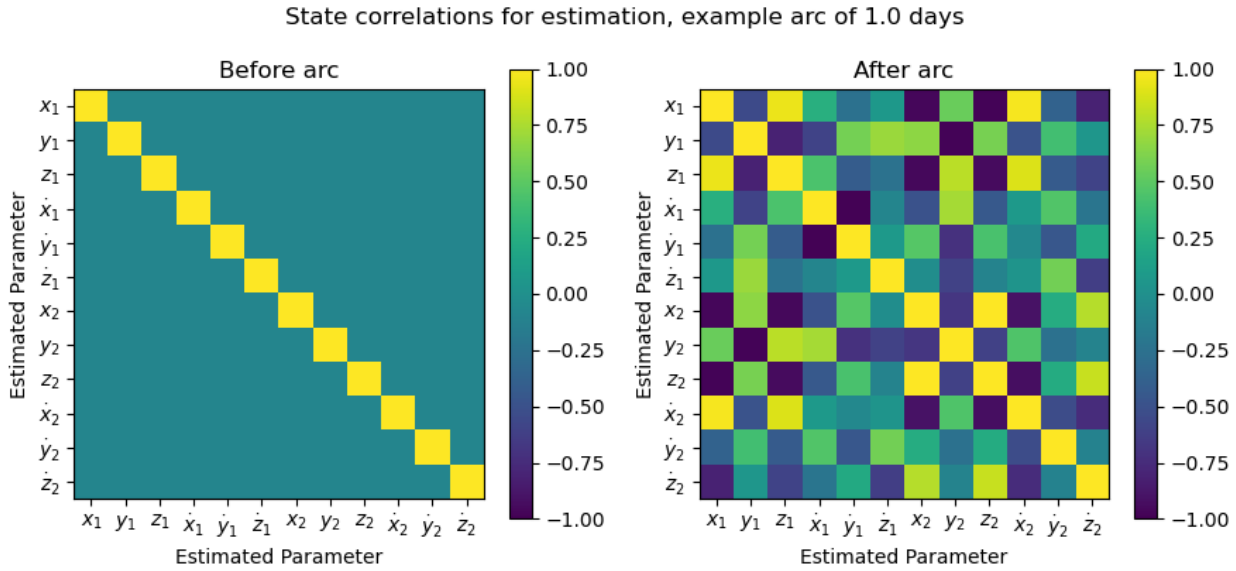

Figure 5.15: Correlations between spacecraft states in estimation in default case

Observations

The observation history is plotted to see whether the observation residuals (the difference between the estimated trajectory and the truth) are as expected and that there are not discontinuities in the ISL range observations. Figure 5.16 shows that observations are performed at a constant interval. The residuals are the final residuals that are found for the best iteration of the iterative BLS estimator.

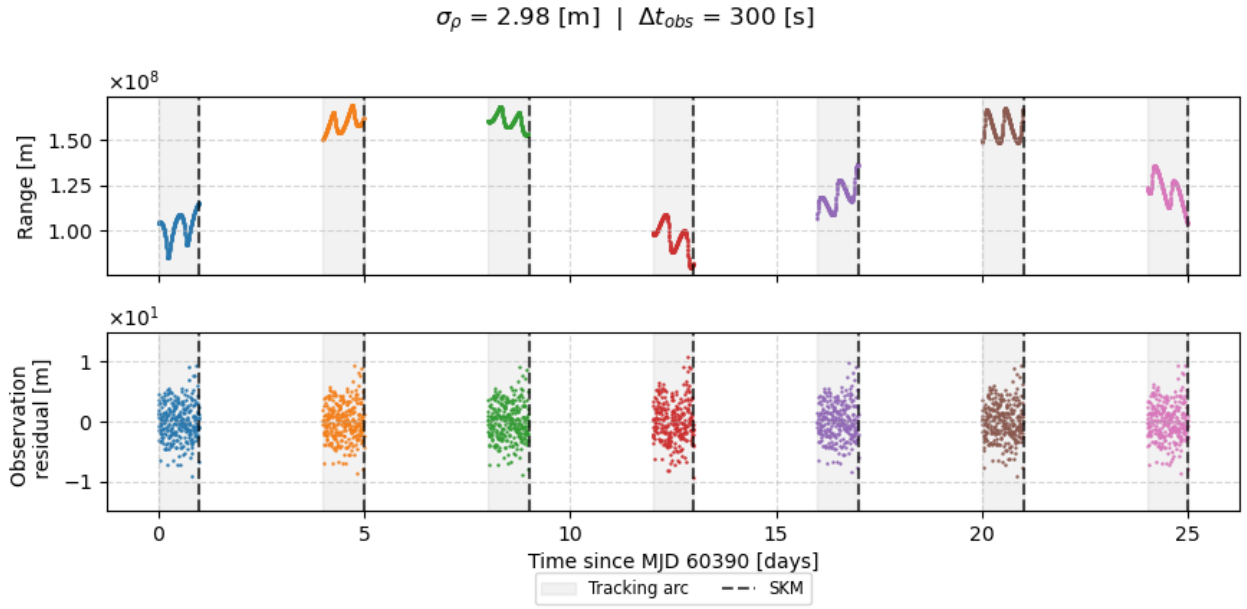

Figure 5.16: Observation history for default case

The residuals seem to follow a Gaussian distribution, indicating that the estimator has fitted the model to the truth near perfectly. This is expected when there are no systematic bias effects included in either the observation model or dynamic model. As such, for the settings of the default model this is what is expected. To be sure of the normality, the Shapiro–Wilk test statistic was used to determine whether the Null-hypothesis, which is that the residuals indeed follow a Gaussian distribution, is true or false [132]. Indeed, all cases are indeed normally distributed as shown in Figure 5.17.

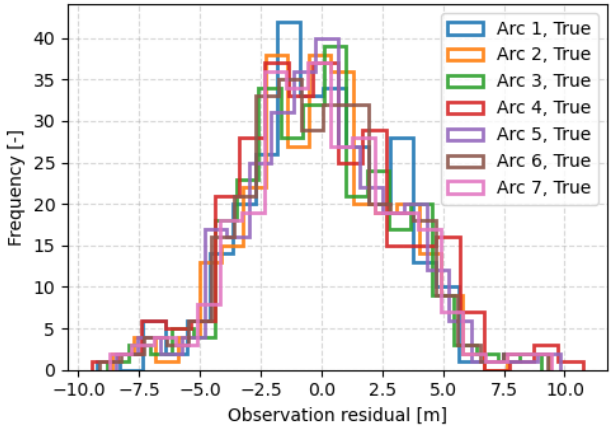

Figure 5.17: Histogram of observation residuals with Shapiro–Wilk test results

Observability analysis
The observability metrics discussed in Section 3.4 allows to examine the regions of higher and lower parameter estimation effectiveness, which translates into OD errors, which translates into a larger ΔV. Figure 5.18 shows that LPF possesses a much larger variation of effectiveness than LUMIO and larger in magnitude. This suggests that, although information on LPF states is obtained to varying degrees of success over time, the state information of both satellites are observable and beneficial towards the estimation process. Velocity components in the z-axis appear to have more difficulty being observed.

The figures below show only the result for the first arc for better visibility of the results. As can be shown in the upper figure of Figure 5.18, effectiveness is rising as measurements give the estimator useful information. The LPF plot, which is connected to the relative geometry between S/C, exhibits more variations and its effectiveness varies heavily with its orbital location. As discussed in Section 3.4, the condition number of the information matrix provides insights into the numerical stability of an estimate. A low condition number is referred to as well-conditioned. This means that a little change in the inputs (the observations) results do not result in a large change in the solution or dependent variable (the state estimates). A decreasing value of this metric for both LPF and LUMIO suggests a good convergence towards an estimate.

Lastly, a factor known as the Dynamic And Geometric Dilution Of Precision (DAGDOP) is used to take into account effects from inter-satellite dynamics and geometry simultaneously, which is recommended in uses cases of dynamically varying uncertainties over time [35]. This is the same as the 3D RSS value of the three estimation uncertainties values associated with the position of LUMIO over each epoch.

Figure 5.18 considers the effects of the total position of velocity states only. It is also possible to see if there is any observability associated with specific states. According to Figure 5.19, this is not the case as the values of the shown observability metrics appear to be similar in magnitude. This suggests that there is sufficient geometric variety between the orbits which is beneficial for the estimation process and thus ultimately the accuracy of the SKM maneuvers.

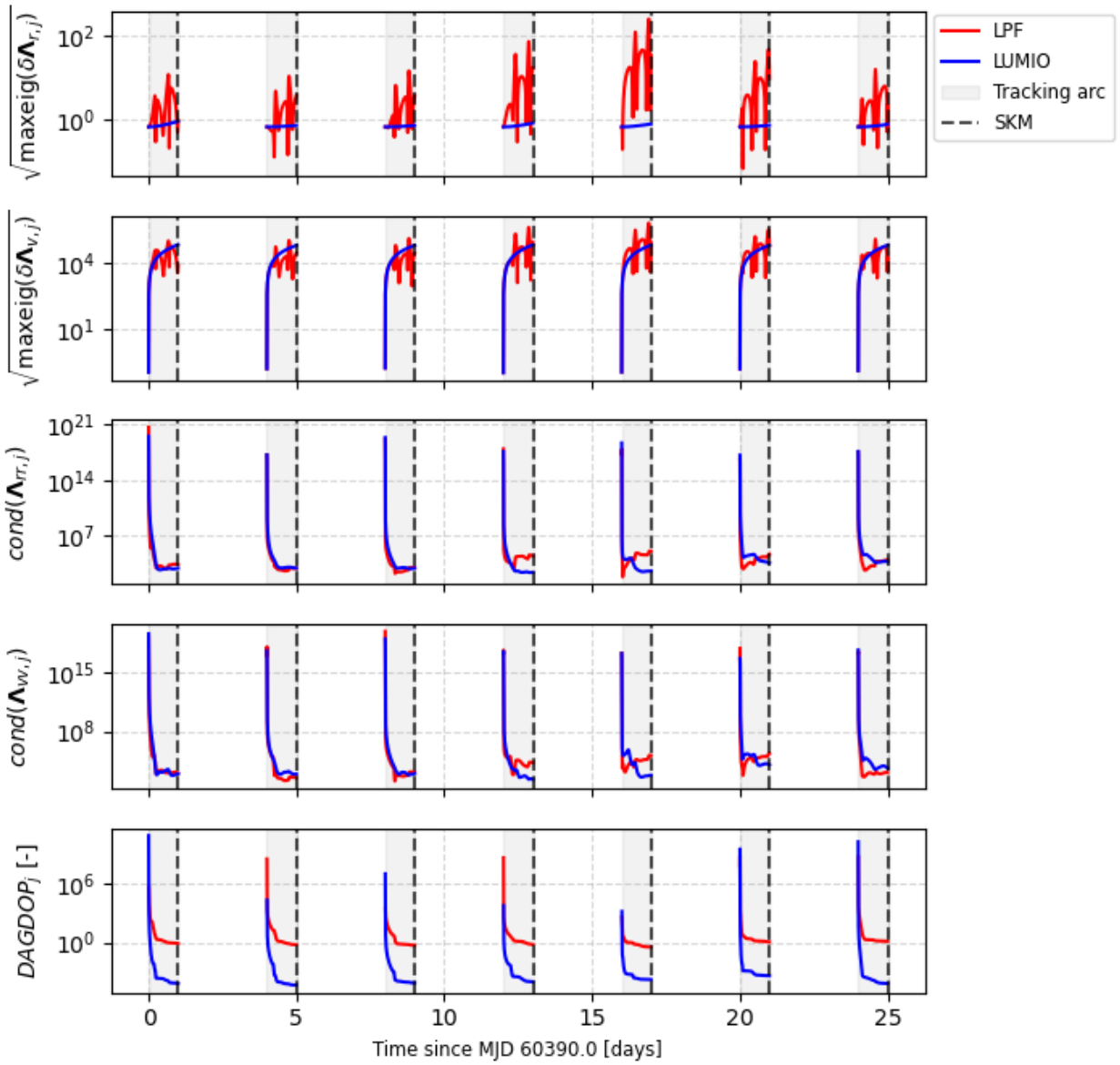

Figure 5.18: Observability metrics for default case

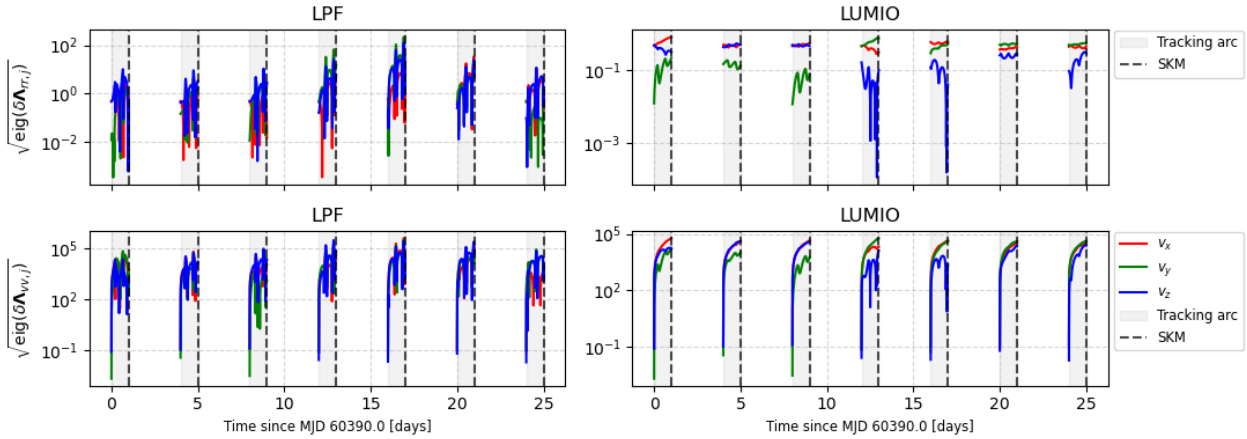

Figure 5.19: Observability metrics for default case decomposed by individual state

5.2.2. Candidate scenarios

Section 5.2.1 yielded results associated with the default observation window case. However, the goal of this thesis is to evaluate the effect of a change in window timings. This section aims to provide a visualization of the effect of different window scenarios on the results of the total correction cost. The advantages and disadvantages from the operational perspective are discussed as well. The tracking window configurations serve as an initial guide towards an optimization routine, which will be discussed in Section 5.4. All simulation settings remain the same as defined in Table A.2, but only the respective observation window timing is adjusted. The results are from a Monte Carlo evaluation of 10 runs. The only variation comes from the observations, as a result of measurement noise.

In the analysis, there are two types of tracking window scenario's that are considered. Table 5.1 shows the scenarios. Values with an asterisk (*) resemble the default tracking window case. The arc durations are chosen to highlight the upper and lower limits of realistic arc configurations. The first scenario simply considers varying arc durations and intervals. It could be that specific combinations of duration and interval are superior to others. In this case, within a tracking window configuration, the value of the interval and duration are kept constant, so it is not yet optimized by adaptively tailoring the lengths of certain arcs to improve costs.

The other scenario looks to what extend tracking around specific orbit locations affects the total SKM costs. Specific regions near an elliptical orbit can yield different degrees of estimation errors and can influence SKM costs [101]. For the specific orbit regions cases, the *perilune* and *apolune* cases are chosen such that they highlight the effect of the extreme regions of the LPF orbits. As such, orbit-based observation configurations as studied as well. As can be derived from Figure 5.4, the orbital period of LPF is approximately 0.45 days. In order to remain as close as possible to the default maneuver frequency of 4 days, a tracking arc is only done every 8 passes for the perilune and apolune cases.

	Cases (days)						
Constant							
Arc length	0.1	0.2	0.5	1.0*	2.0		
Arc interval	0.1	0.2	0.5	1.0	2.0	3.0*	4.0
Orbit based							
Perilune	0.1	0.15	0.2				
Apolune	0.1	0.15	0.2				

Table 5.1: Test cases for candidates of observation window timings

Tracking with constant length and interval

The estimation uncertainty gives an indication of the range of estimation errors that can be expected, given the *a-priori* comprised on the data of Table A.2. Figure 5.20 shows the evolution of the estimation uncertainties for varying arc lengths. As such, the initial estimation uncertainty values are the same for both satellites. Note the logarithmic scaling on the y-axis. Near the start, the estimation uncertainties grow much faster for LPF than for LUMIO. This may be due to the fact that the faster dynamics of LPF generates much larger sensitivity to the initial estimate and drives the uncertainty upwards. Also, as expected, an overall decrease occurs for both satellites, which shows that the estimation uncertainties of LPF correlate with the estimation uncertainties for LUMIO. The position and velocity elements of the estimation uncertainties for a given spacecraft follow the same shape. After 14 days, the estimation uncertainties of all four cases have reduced by one to two orders of magnitude with respect to the value at the start epoch, indicating that the length of the arc might not have a large influence on the estimation error over the long term. Or in other words, tracking for 2.0 days instead of 0.1 days might not yield a drastic difference over the long run when it comes to the estimation error.

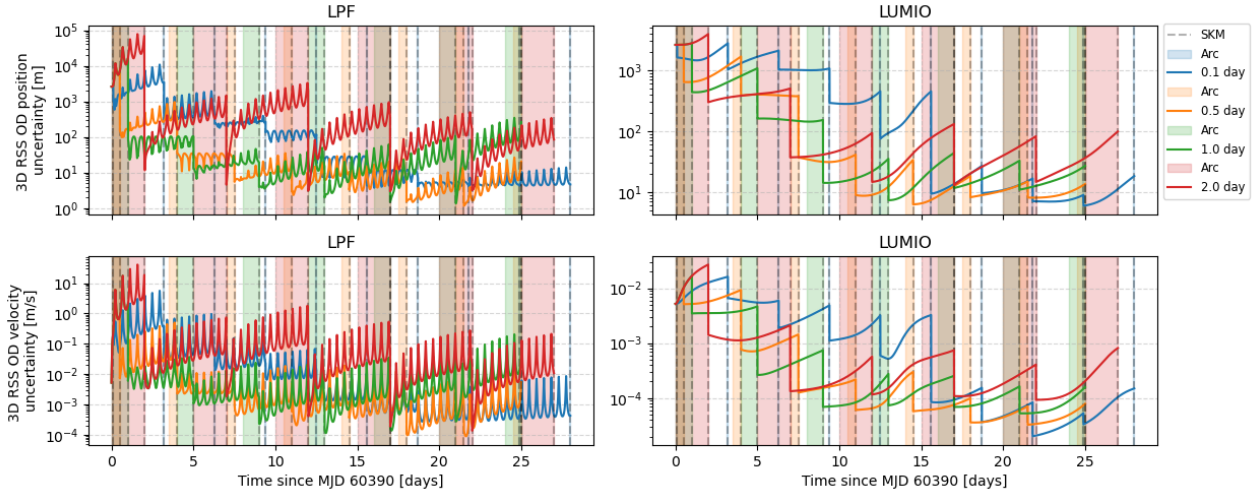

Figure 5.20: Comparison of 3D RSS estimation uncertainties for varying arc lengths

Figure 5.21 shows the relationship between the ΔV of each correction and the corresponding estimation error and *estimated* dispersion, both for RSS position states. It is crucial to note that the magnitude of the SKMs depends on the previous SKM, which in turn depends on the magnitude of the estimation error and the dispersion. Figure 5.21 shows that the magnitude for each correction for a given case. A couple things can be observed:

- **A too short arc length yields larger estimation error**
  Due to the limited variation in observational geometry and quantity of measurements, the shortest arc shown (blue) tends to maintain a larger estimation error. The poor estimation error also translates into a worse dispersion estimated on-board. Especially at the second SKM is large, which comes from the minimal reduction in estimation error that occurred in the first arc.

- **Shorter arc lengths yield larger cost uncertainty**
  Observe the error bars associated with the shorter arc lengths, especially the second blue arc. With less measurements, random noise effects can result in more variation in the final state estimate as the true observable is less well known with less measurements. Generally, the uncertainty decreases as the more tracking sessions have occurred.

- **After a threshold, measuring more does not improve estimation error**
  At some point, the estimation error is not so sensitive to arc length anymore. From that point, the dispersion might have a bigger influence on the costs.

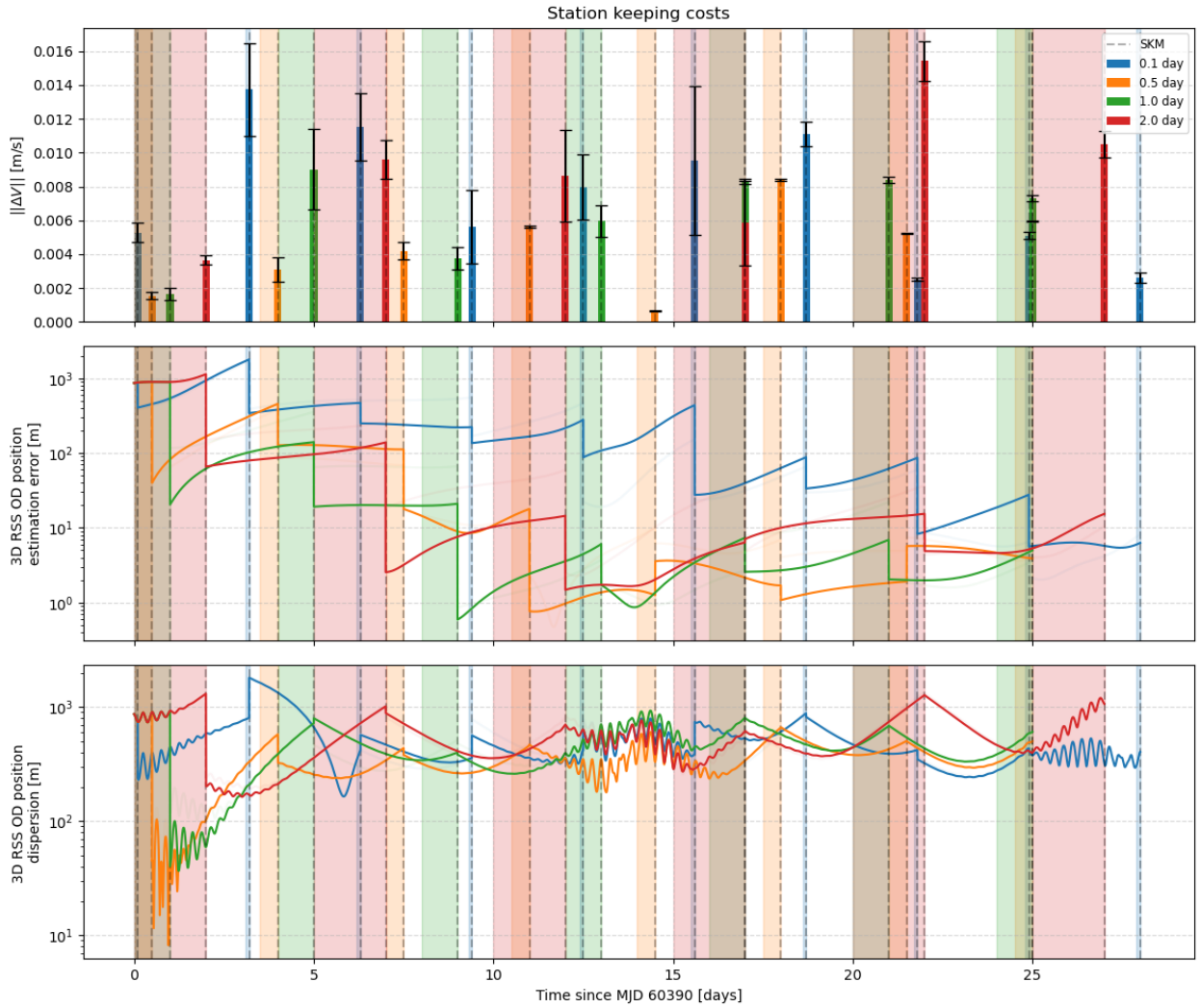

Figure 5.21: Station keeping cost comparison for default case with various constant arc lengths

Looking at Figure 5.22 and the annual approximation Figure 5.23, the minimum in this specific scenario seems to be located at an arc duration of 0.5 days. This suggests that it might be better to have tracking arcs of 0.5 days instead of the default scenario of 1.0 day. One should keep in mind that the results shown in Figure 5.22 are all with respect to the default simulation settings and thus only the arc length is changed. It could be the case that better costs exist when other (non-window) simulation parameters are changed as well. For example, the best arc length/arc interval combination might be related to the measurement interval or location of the target points. Additionally, a better optimum might exist for cases in which the arc lengths are variable instead. This optimal shall be found by the optimization routine later. Regardless, it was chosen to continue with the default arc length of 1.0 day as a start of the optimization in Section 5.4.

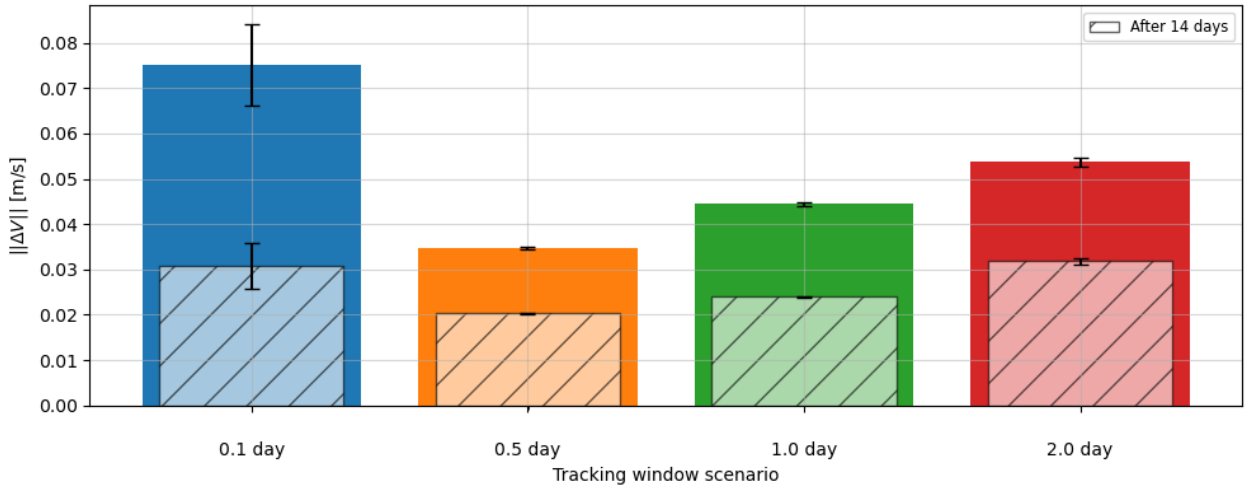

Figure 5.22: Total station keeping cost comparison for various constant arc lengths and fixed arc interval

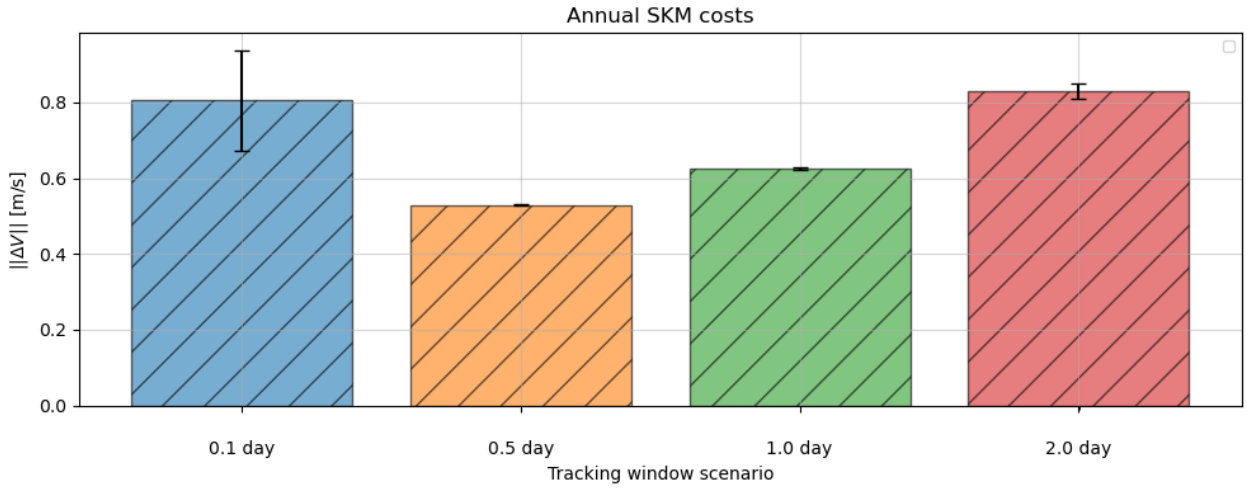

Figure 5.23: Approximation of annual total station keeping cost for various constant arc lengths and fixed arc interval

Another interesting aspect to consider is the linked relationship between the arc interval and the arc length. Figure 5.24 shows the costs for various combinations of these two parameters. The major x-labels signify the arc interval, while the minor ones represent the arc duration. From this figure, it can be observed that:

- **Arc length is the limiting factor**
  The largest deviations are caused by choosing the tracking duration. According to this logic, the same cost can be achieved with having tracking sessions spread further apart from each other. However, a very crucial point must be mentioned here. All costs are based on a simulation of 28 days. In scenario's where the tracking arcs are further apart, the relatively short simulation duration might underestimate the true cost as a large individual correction could come just after the 28 days due to dispersion or estimation error build-up.

- **A too short arc length generally yields larger costs**
  As mentioned earlier, observing too shortly will yield larger costs.

- **0.5 days of tracking often yields lowest cost**
  The trend shown in Figure 5.22 generally holds with varying arc intervals. Note how small the error bars

are, which indicates that the cost annual approximation does not vary much given different sets of random measurement errors.

- **Larger arc intervals yield more cost uncertainty**
  Observing the error bars, one can see that it increases with larger arc interval. This is probably caused by the longer duration until the next arc, such that initial estimation differences have time to deviate more.

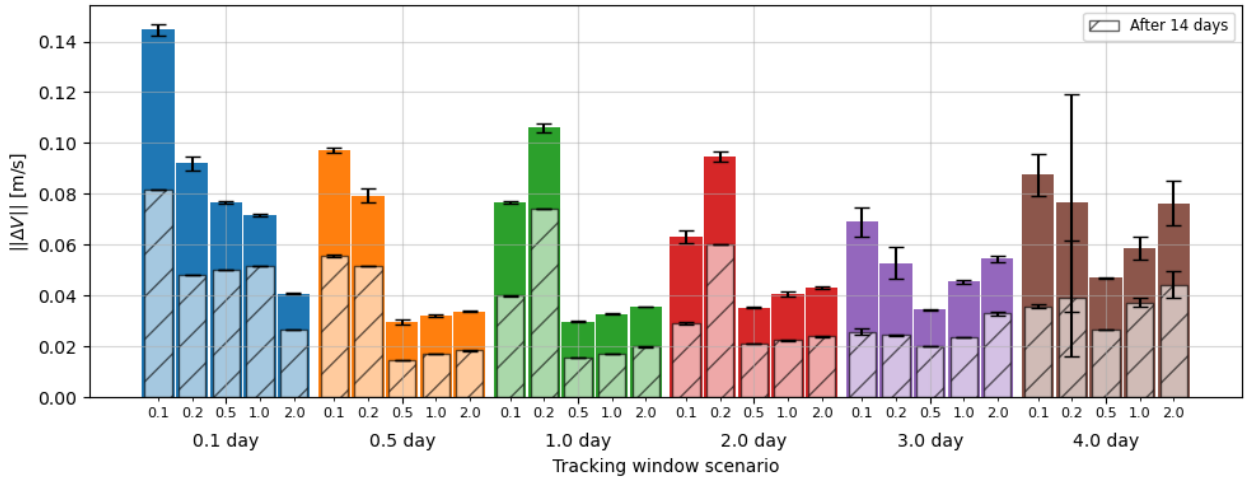

Figure 5.24: Maneuver costs for various arc length and arc interval combinations

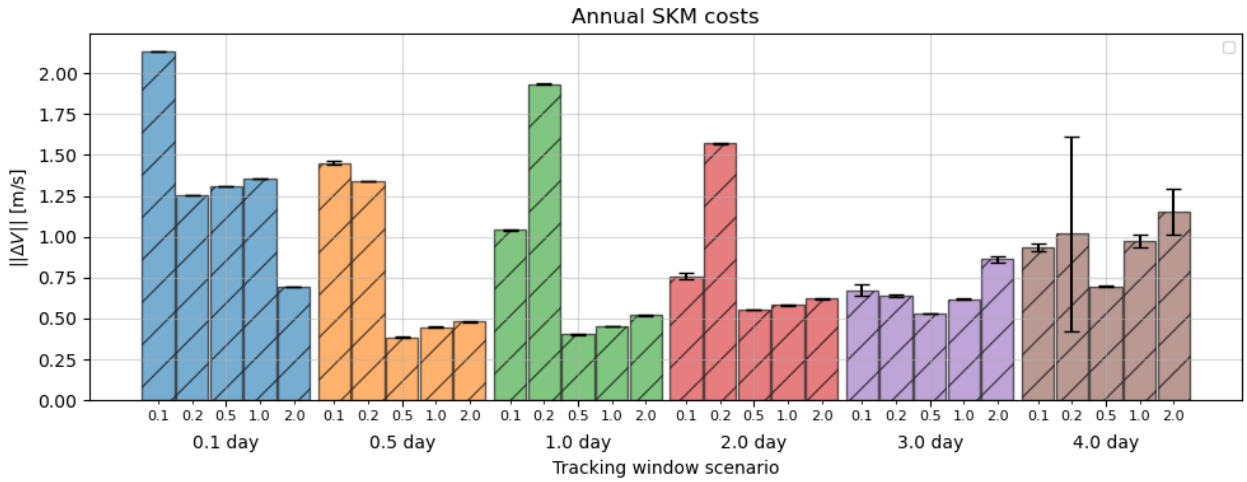

Figure 5.25: Annual maneuver costs for various arc length and arc interval combinations

Tracking at specific orbit locations

One can also look at tracking at specific location in-orbit. This section aims to provide similar details as the previous by looking at the effect of tracking at the perilune and apolune of the orbit of LPF. The choice of the arc durations and locations is explained at the start of Section 5.2.2. Figure 5.26 and Figure 5.27 show the uncertainty and individual corrections for a perilune and apolune case for a scenario in which a 0.1-day tracking session is done every 8 LPF orbit revolutions to approximately match the maneuver frequency of 4 days. This might not be the best for ΔV so a deeper analysis is done into the perilune and apolune cases by considering varying amounts of the number of passes between two tracking arcs. For example, when the value is 5, then an arc is conducted every 5 LPF orbits.

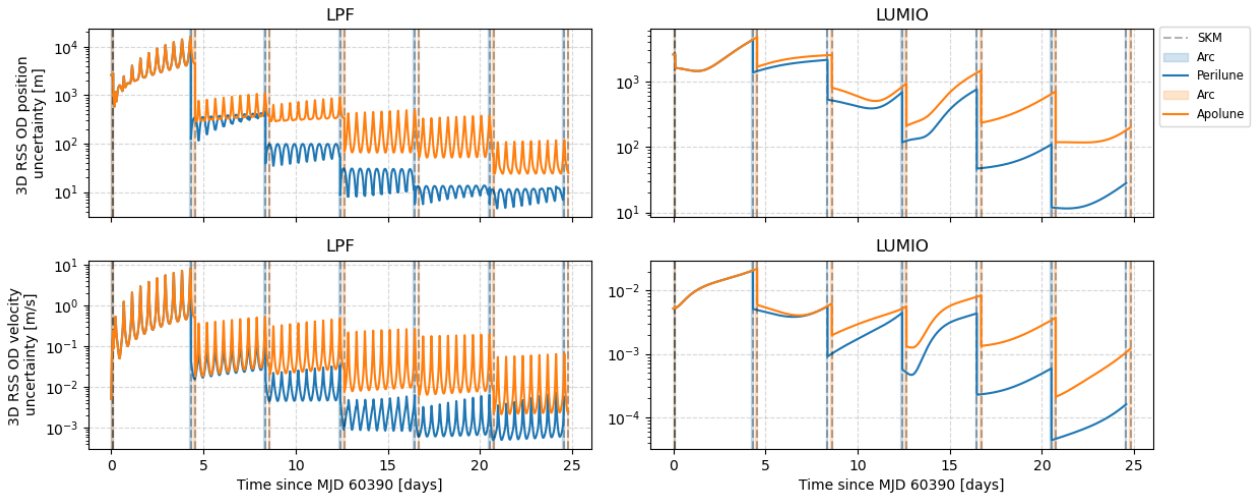

Figure 5.26: Comparison of 3D RSS estimation uncertainties for varying orbit regions

Figure 5.26 shows that the perilune performs better when it comes to the estimation uncertainties. The same nature as Figure 5.20 is clear, where magnitudes of the uncertainties of one satellite tend to correspond with the magnitude of the other. As such, improvements in estimation aid the state knowledge of both satellites simultaneously.

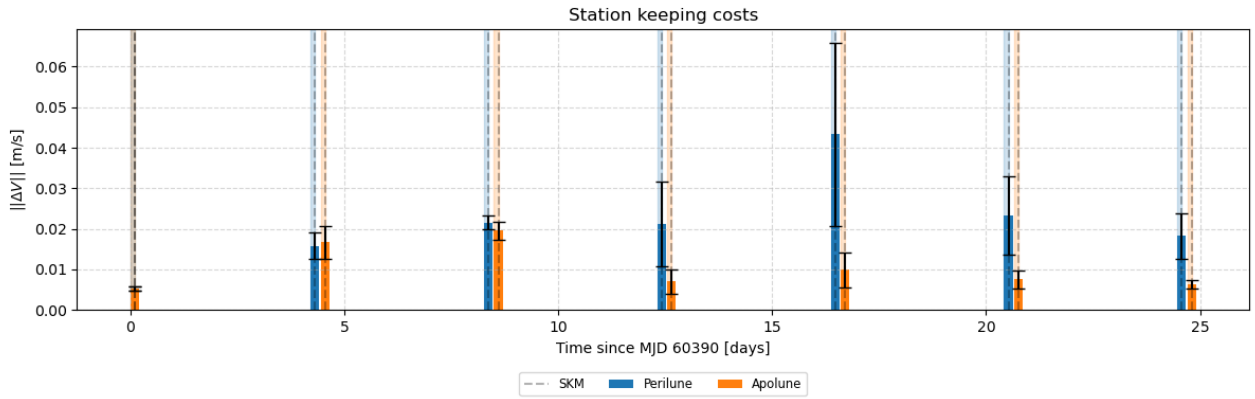

Figure 5.27: Station keeping cost comparison for varying orbit regions with default arc interval

Figure 5.28 to Figure 5.30 show the costs for increasing arc lengths around the orbit points. The following observations can be made:

- **Perilune only worse for short tracking arcs**
  Only Figure 5.28 shows that there is only a clear distinction in costs between tracking in perilune and apolune. Only for perilune tracking, skipping more passes yields worse results.

- **Cost uncertainty grows with arc interval**
  Error bars grow when there are more passes before a new tracking session is performed. The uncertainties are slightly larger for perilune tracking, which could be explained by a large variation in estimates caused by the faster dynamics in the perilune.

- **Skipping passes more or less random for larger arcs**
  In Figure 5.29 and Figure 5.30 it is clear that tracking at more passes doesn't improve cost. If anything, some are especially worse. This could be due to the fact that the target point is fixed at 3 days, which makes it possible that corrections have to be performed while the while the spacecraft is relatively far apart from the reference orbit.

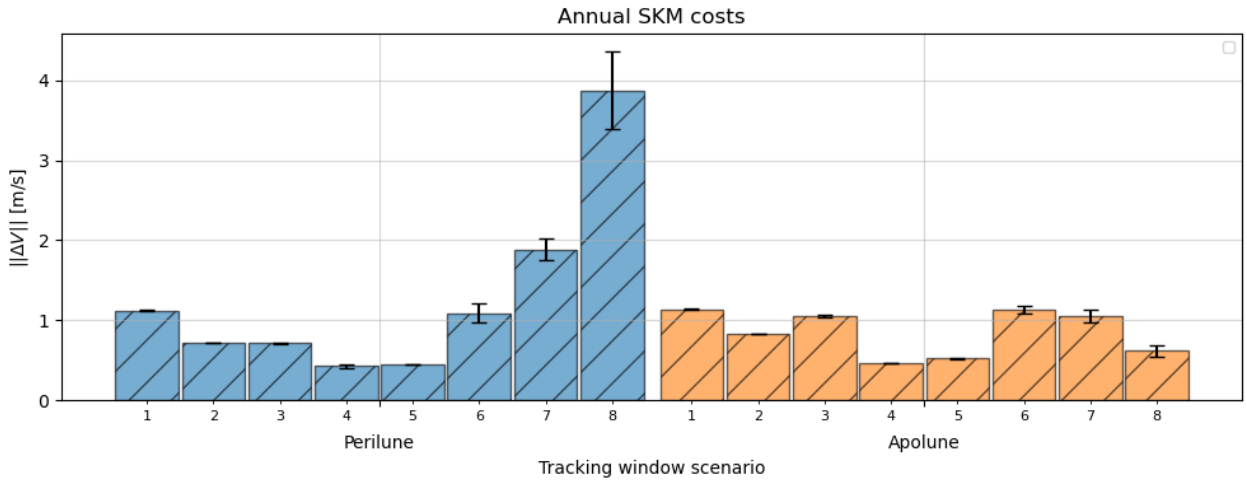

Figure 5.28: Annual approximation of total station keeping cost comparison for perilune and apolune, 0.1 day of tracking

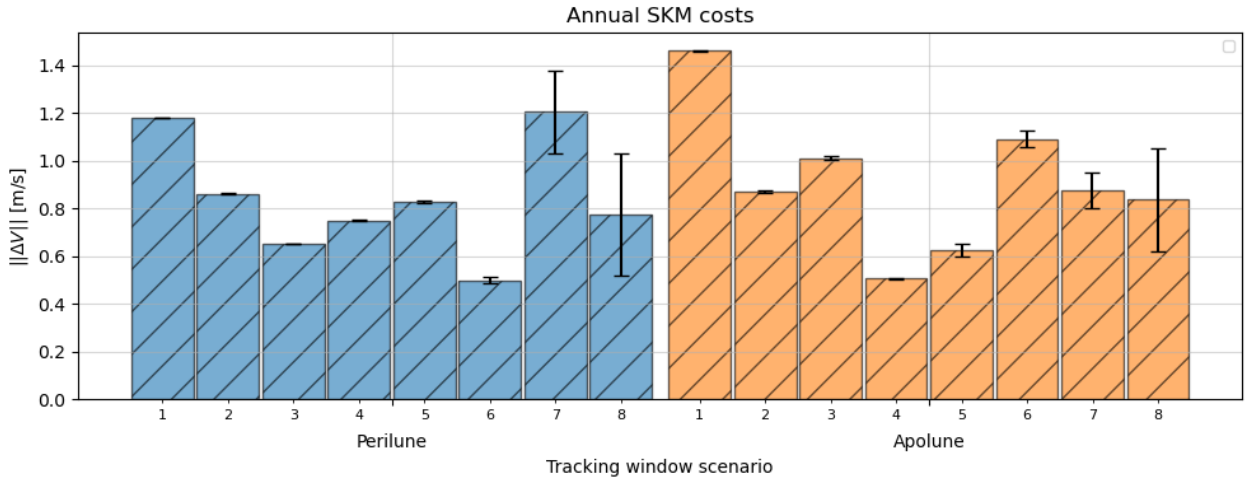

Figure 5.29: Annual approximation of total station keeping cost comparison for perilune and apolune, 0.15 day of tracking

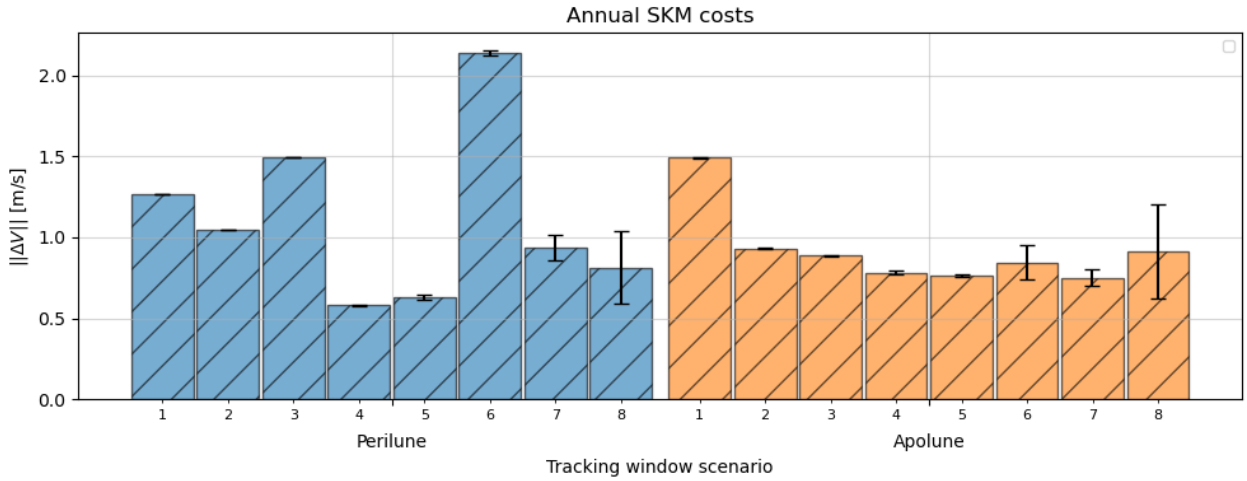

Figure 5.30: Annual approximation of total station keeping cost comparison for perilune and apolune, 0.2 day of tracking

5.2.3. Summary

All in all, the best annual costs of the discussed cases in Section 5.2.1 and Section 5.2.2 are shown in Table 5.2. Observe that the lower limit seems to be around 0.44 m/s. Additionally, note that thus-far only cases are considered where the arc lengths are constant and thus do not vary within a tracking window configuration. Results of further optimization are shown in Section 5.4.

	Configuration	**Annual ΔV [m/s]**	**Reduction [%]**
Constant arcs			
Default	Arc length: 1.0 day Arc interval: 3.0 day	0.613 $\pm$ 0.0066 1σ	-00.000 $\pm$ 1.077 1σ
Best	Arc length: 0.5 day Arc interval: 0.5 day	0.375 $\pm$ 0.0020 1σ	-38.597 $\pm$ 0.228 1σ
Orbit based			
Perilune	Arc length: 0.15 day Arc interval: Every 6 passes	0.505 $\pm$ 0.0124 1σ	-17.618 $\pm$ 2.023 1σ
Apolune	Arc length: 0.15 day Arc interval: Every 4 passes	0.498 $\pm$ 0.0082 1σ	-18.760 $\pm$ 1.337 1σ

Table 5.2: Best annual total station keeping cost per tracking window configuration case

5.3. Sensitivity analysis

The navigation model contains a variety of parameters that could be adjusted. This means that any adaptation to those variables comes with a degree of variability of the ΔV objective outcomes. This section evaluates the sensitivity of those outcomes to these variable changes. As mentioned in Chapter 4, the default settings of Table A.2 are used. Any variable besides the changing variable in question varies.

This section is split up into two subsections. Section 5.3.1 aims to provide an insight into the result of variability in parameters related the choice of observation windows. Similarly, Section 5.3.2 compares auxiliary parameters that might affect the model outcomes but are outside the scope of adjustments related to the choice of observation windows. In general, this section aims to compare outcomes to the default cases extensively elaborated upon in Chapter 4 and aims to showcase additional information into the dominant influences for the objective of maneuver cost. All mean and standard deviation values are the result of 10 Monte Carlo runs with the PMSRP01 dynamic model that was selected in Section 5.1. The same data is shown in figure and table form. The table includes a *worst case*, which is defined as the mean plus three standard deviations. Note that this result technically does not cover all results as results could fall outside of the 3σ bound.

5.3.1. Observation window parameters

Table 5.3 provides an overview of the Monte Carlo statistics derived from the test cases. The plots of the annual ΔV can be found in Appendix D. The following statements can be made about the findings:

- The analysis for the arc duration is actually the same as discussed in Section 5.2.2. An arc duration of 0.1 days seems to provide the least ideal ΔV. A possible explanation for this could be that consistently for 0.1 days might not be enough to capture sufficient useful observational geometry which causes the estimation error to remain relatively large over time. On the other hand, at some point, tracking for too long allows for dispersion to grow in the meanwhile and the trade-off between improved estimation error does not outweigh the benefits of a SKM at a lower dispersion. Also, note the larger standard deviation values for the shortest arc. This could be explained by a larger difference in estimation outcomes due to a lower number of measurements for those shorter arcs. This gives more variation in the estimation errors. As a result, the final BLS outcome of the initial states might vary more.

- Regarding the arc interval, a similar statement can be made about the aspect of dispersion. Increasing the time between arcs increases dispersion and, as a consequence, the total SKM cost appears to grow linearly with the interval. The same can be stated about the uncertainty. Estimation outcome differences are exaggerated with time.

- The mission start epoch of the simulation has some influence on the total costs approximate. This is probably caused by the difference in the observational geometry during the tracking arcs, so the choice of when tracking occurs is a driving factor to SKM costs. It is very important to note that the deviation in cost approximation for different mission start epochs is even smaller when using a larger time frame as the simulation duration. The effect on the results for a simulation of 56 instead can be found in Appendix D. This means that a simulation of 28 days, as done in this chapter and shown in Figure 5.31 and Figure 5.32, does not always lead to representable values for the annual costs.

When one looks at the annual ΔV in Table 5.3, the difference between the minimal and maximum costs for *Mission Start Epoch* is 0.1117 m/s, while it is 0.339 m/s and 0.5274 m/s for *Arc Duration* and *Arc Interval*, respectively. This means that the last two variations in annual ΔV is about 3 to 5 times as large compared to those of the mission start epoch.

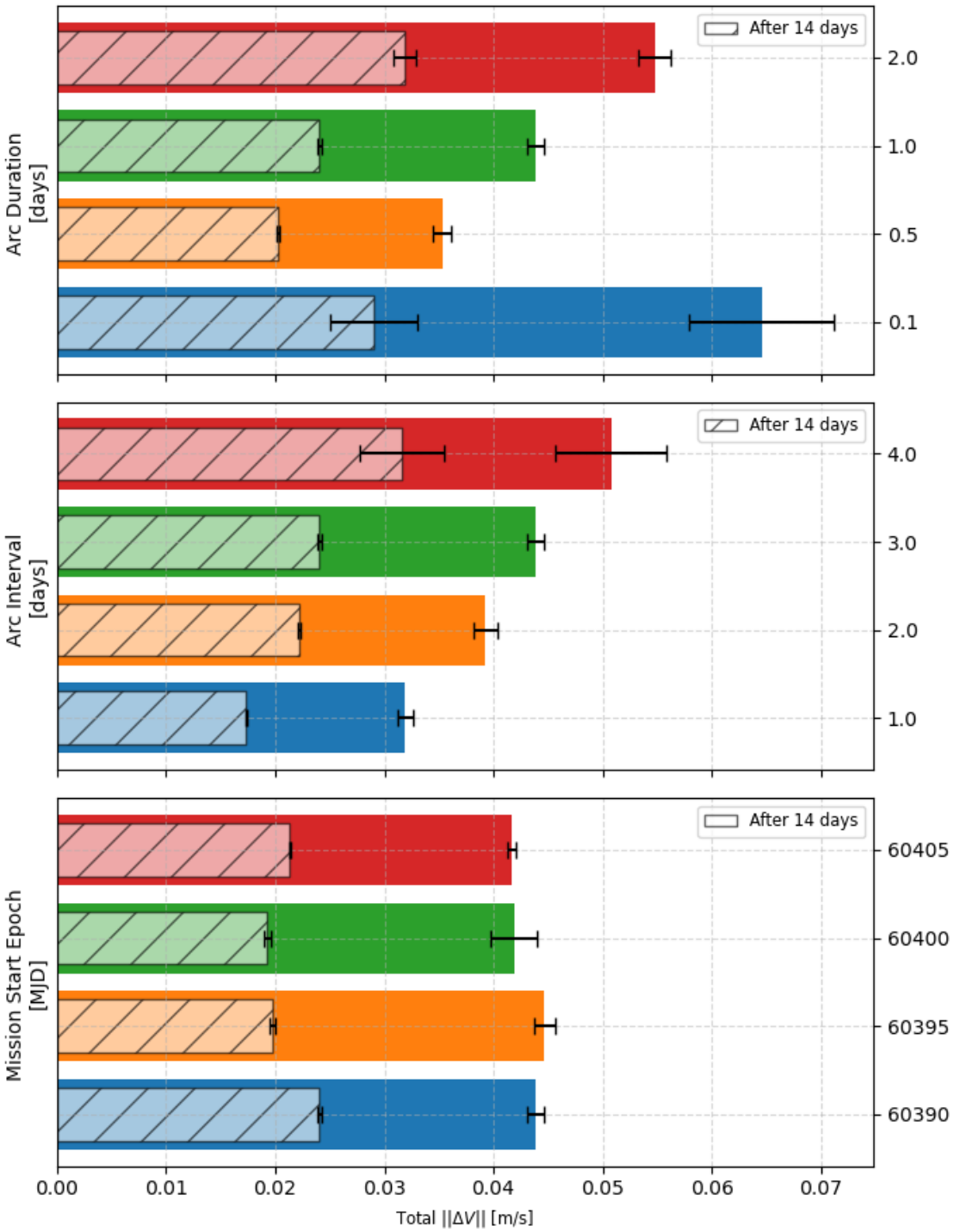

Figure 5.31: Sensitivity analysis results for observation window parameters (28 days)

		Total		After 14		Annual		
Case	**Value**	$\mu_{\Delta V}$	$\sigma_{\Delta V}$	$\mu_{\Delta V}$	$\sigma_{\Delta V}$	$\mu_{\Delta V}$	$\sigma_{\Delta V}$	**Worst**
Arc Duration	0.1	0.0679	0.0056	0.0260	0.0011	0.6791	0.0280	0.7630
	0.5	0.0353	0.0014	0.0203	0.0001	0.5290	0.0015	0.5336
	1.0	0.0453	0.0006	0.0235	0.0003	0.6131	0.0066	0.6329
	2.0	0.0549	0.0011	0.0333	0.0007	0.8686	0.0183	0.9235
Arc Interval	1.0	0.0327	0.0002	0.0173	0.0000	0.4518	0.0010	0.4549
	2.0	0.0405	0.0008	0.0224	0.0001	0.5852	0.0031	0.5944
	3.0	0.0453	0.0006	0.0235	0.0003	0.6131	0.0066	0.6329
	4.0	0.0589	0.0037	0.0375	0.0015	0.9784	0.0388	1.0947
Mission Start Epoch	60390	0.0453	0.0006	0.0235	0.0003	0.6131	0.0066	0.6329
	60395	0.0448	0.0008	0.0198	0.0001	0.5165	0.0018	0.5220
	60400	0.0397	0.0010	0.0192	0.0003	0.5013	0.0073	0.5232
	60405	0.0422	0.0008	0.0216	0.0001	0.5629	0.0025	0.5705

Table 5.3: Sensitivity analysis results for observation window parameters (28 days)

5.3.2. Auxiliary parameters

The results of the auxiliary parameters are shown in a similar fashion. Table 5.4 provides a graphical interpretation of the Monte Carlo results derived from the test cases. For the *Initial Estimation Error* and *Orbit Insertion Error* case, the notation for the values is defined as position/velocity. The plots of the annual ΔV can be found in Appendix D. The following statements can be made about the findings:

- Most notably, the total cost is not much affected by the initial values of estimation error unless both the position and velocity components are increased by tenfold. However, the stable period after 14 days remains the same. Likewise, this is the case for varying insertion errors. This validates the notion that after 14 days, one has reached the stable region for nominal operation and the SKMs cost is just affected by the choice of observation windows.

- Interestingly, the number of measurements does not seem to influence the costs. This might have to do with the initial covariance that is already quite accurate. Lower covariance leads to a lower significance put on the new measurements and thus the final result is not as much affected by the number of measurements.

- Regarding target points, the analysis shows that choosing further points in the future doesn't guarantee better costs. The optimal, with the remainder of the parameters at the default settings, seems to be around the 3 to 4 days downstream. This aligns roughly with the epochs of the SKMs. In the single target point scenario, the method aims for minimal dispersion at the given TP. As such, larger deviations of TPs with respect to the planned SKM epoch leads to larger dispersion at the SKM epoch due to undershooting or overshooting.

- When it comes to the minimal ΔV threshold, the total increases by a lot when a lower minimal ΔV is chosen. The reason for this is that only highly minimal magnitudes of ΔV are required to maintain the orbit in the default case. Neglecting the SKMs will not cancel the tracking sessions but will maintain the dispersion to keep growing. As a consequence, the dispersion at the first correction that requires value over the threshold value will be relatively large. The 0.02 and 0.03 [m/s] cases are indifferent because the required costs were above 0.03 and not between the two threshold values.

- Lastly, the uncertainty of the costs varies more with increased SKM error than the mean value. The errors are drawn from a normal distribution and any error the current correction affects the next one. Surprisingly, the noise does not lead to large errors, presumable because correction errors have a maximum of 4 days to expand before a new one occurs.

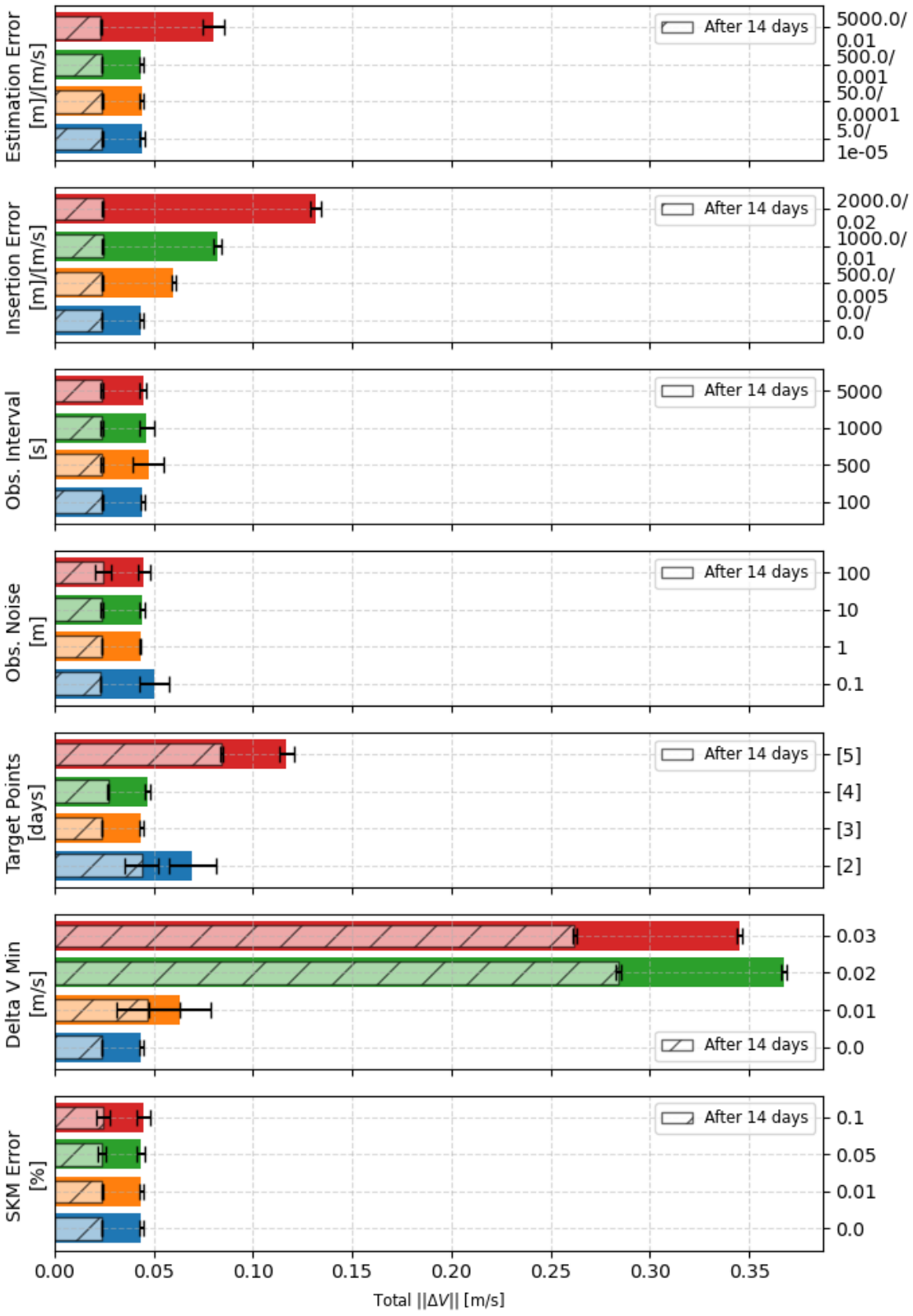

Figure 5.32: Sensitivity analysis results for auxiliary parameters (28 days)

		Total		After 14		Annual		
Case	**Value**	$\mu_{\Delta V}$	$\sigma_{\Delta V}$	$\mu_{\Delta V}$	$\sigma_{\Delta V}$	$\mu_{\Delta V}$	$\sigma_{\Delta V}$	**Worst**
Initial Estimation Error	5.0/ 1e-05	0.0444	0.0006	0.0235	0.0002	0.6121	0.0043	0.6251
	50.0/ 0.0001	0.0445	0.0003	0.0235	0.0004	0.6134	0.0098	0.6427
	500.0/ 0.001	0.0453	0.0006	0.0235	0.0003	0.6131	0.0066	0.6329
	5000.0/ 0.01	0.0873	0.0050	0.0227	0.0002	0.5921	0.0043	0.6050
Orbit Insertion Error	0.0/ 0.0	0.0453	0.0006	0.0235	0.0003	0.6131	0.0066	0.6329
	500.0/ 0.005	0.0613	0.0024	0.0236	0.0004	0.6151	0.0094	0.6434
	1000.0/ 0.01	0.0820	0.0036	0.0237	0.0003	0.6167	0.0071	0.6381
	2000.0/ 0.02	0.1314	0.0042	0.0239	0.0004	0.6223	0.0101	0.6526
Observation Interval	100	0.0448	0.0012	0.0235	0.0003	0.6131	0.0076	0.6360
	500	0.0459	0.0033	0.0236	0.0003	0.6156	0.0085	0.6412
	1000	0.0447	0.0019	0.0237	0.0002	0.6173	0.0064	0.6367
	5000	0.0457	0.0047	0.0238	0.0003	0.6215	0.0077	0.6447
Noise	0.1	0.0466	0.0022	0.0242	0.0010	0.6301	0.0271	0.7114
	1	0.0438	0.0009	0.0234	0.0002	0.6091	0.0048	0.6236
	10	0.0453	0.0009	0.0236	0.0003	0.6161	0.0083	0.6410
	100	0.0503	0.0053	0.0229	0.0022	0.5964	0.0566	0.7663
Target Point Epochs	[2]	0.0829	0.0122	0.0529	0.0111	1.3782	0.2885	2.2439
	[3]	0.0453	0.0006	0.0235	0.0003	0.6131	0.0066	0.6329
	[4]	0.0489	0.0023	0.0267	0.0002	0.6952	0.0054	0.7114
	[5]	0.1195	0.0044	0.0848	0.0012	2.2105	0.0313	2.3043
Delta V Min	0.00	0.0453	0.0006	0.0235	0.0003	0.6131	0.0066	0.6329
	0.01	0.0582	0.0212	0.0399	0.0224	1.0410	0.5850	2.7960
	0.02	0.3727	0.0010	0.2896	0.0010	7.5510	0.0258	7.6284
	0.03	0.3499	0.0009	0.2669	0.0009	6.9580	0.0242	7.0306
Station Keeping Error	0.00	0.0453	0.0006	0.0235	0.0003	0.6131	0.0066	0.6329
	0.01	0.0449	0.0006	0.0228	0.0004	0.5956	0.0116	0.6305
	0.05	0.0451	0.0005	0.0216	0.0007	0.5620	0.0191	0.6194
	0.10	0.0481	0.0013	0.0221	0.0007	0.5765	0.0177	0.6296

Table 5.4: Statistical results of Monte Carlo sensitivity analysis (28 days)

5.3.3. Summary

Considering the results of Table 5.3 and Figure 5.32, none of the annual ΔV yield a value that is smaller than those presented in Table 5.2. The sensitivity analyses have shown that the SKM costs is the most sensitive to the parameters of *minimum* ΔV *threshold* and *target points*.

5.4. Optimization analysis

Finally, this section seeks to find an optimized result of the optimization windows by considering the optimization scheme that was explained in Section 4.3.7. Remember, that the objective is to minimize for the annual ΔV of the corrections that occur after day 14 of the simulation. Similar to the sensitivity analysis, all analyses are done using the default settings defined in Table A.2. The test cases that are considered in Table 5.5 are therefore the only changing parameter. The first comparison concerns the variation in the optimization method. The way that an algorithm search from the optimum might affect the finally found design vector values. Secondly, the duration is varied to see if the annual cost approximation method explained in Section 4.3.1 varies in final value significantly if one has a longer time period to represent the annual correction cost. Varying the model fidelity serves as a way to validate the assumption that a point-mass model is indeed sufficient enough to use instead of a more computationally expensive spherical-harmonics based model as discussed in Section 5.1 and whether is actually has an effect on the optimization algorithm.

For a given test case, the only variety is caused by noise in the observations. To see what happens to the optimization solution under variation in observations, 5 optimization runs are done with different noise histories (different seeds for the observation noise). The final solutions for the test cases are shown in tables and compared in terms of annual ΔV. The structure of this section is such that it follows the order of the rows in Table 5.5. Finally, Section 5.4.4 will make final remarks on the comparison between the default scenario and the overall found best optimization result.

	Test cases	
Optimization method	Nelder-Mead	PSO
Model durations	28 days	56 days
Model fidelity	PMSRP01	SHSRP01

Table 5.5: Optimization model test cases

5.4.1. Varying optimization method

This section describes the differences in optimization outcomes between the Nelder-Mead and PSO algorithms. In total, 5 MC runs were conducted. The choice for this number was chosen arbitrarily, to simply show that there is variation in the optimization outcomes. For both methods, each run yielded a different design vector solution, while the reduction in the objective value is similar for all. Only the result of the first run is shown in the main body. The statistics of all runs can be found in Appendix C. Given this specific solution of the observation windows, this configuration was run multiple times with different noise seeds to confirm that the solution is robust in the sense that it can lead to ΔV reduction for more than one specific set of observation noises.

Observation windows

Figure 5.33 and Figure 5.34 show the evolution of the individual corrections (the colored bars) for the Nelder-Mead and PSO algorithm respectively. First note the decrease in standard deviations of the corrections over time, which is caused by the reduced effect of estimation error on the magnitude of a correction. For the optimized version, the arc lengths tend to be made shorter for the arcs that occur after 14 days. This is more extreme for the PSO algorithm. In fact, the PSO algorithm reduces the last two arcs to the lower bound of 0.1 days, indicating that such a low arc duration might be sufficient for orbit determination. On the other hand, the fifth arc is made longer, so shortest arcs might not always be best.

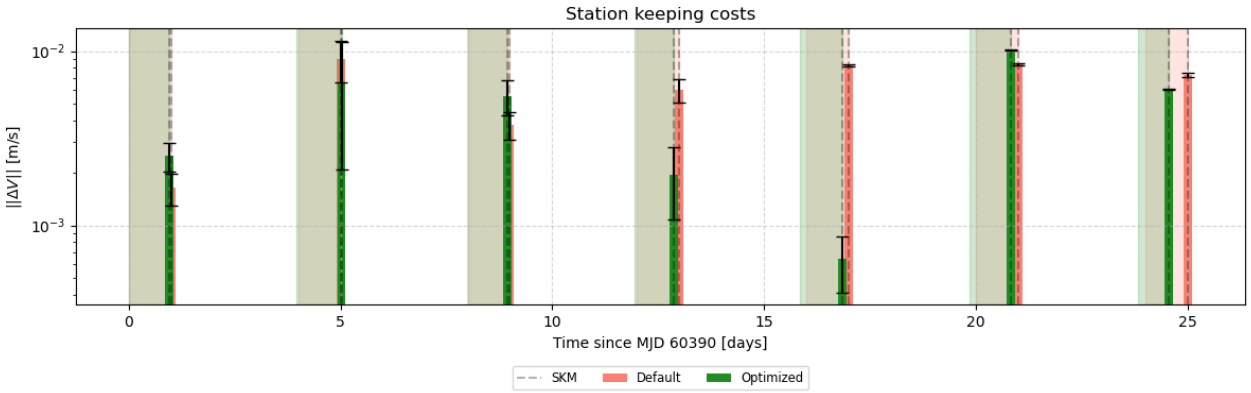

Figure 5.33: Default and optimized tracking configuration resulting from the Nelder-Mead optimization method for 28 days (run 1 of 5)

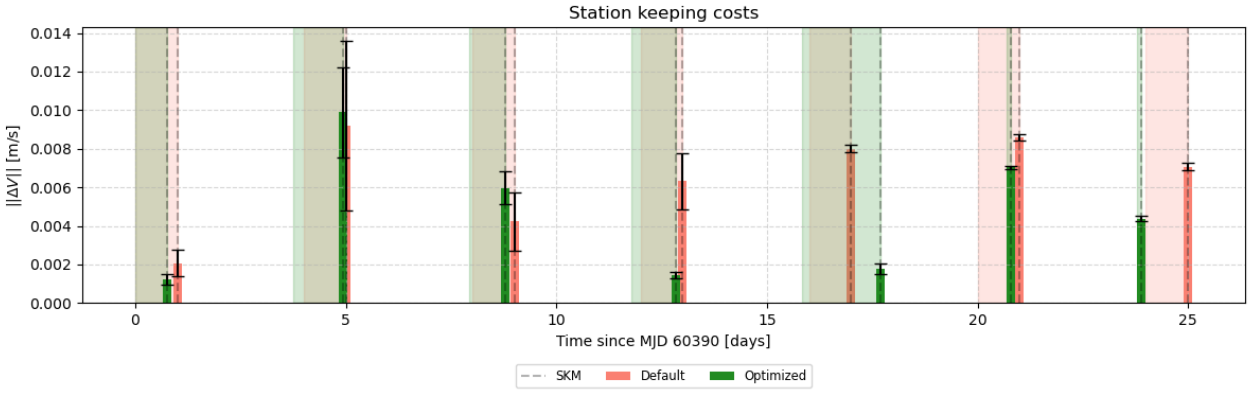

Figure 5.34: Default and optimized tracking configuration resulting from the PSO optimization method for 28 days (run 1 of 5)

By looking at the magnitude of the estimation error and dispersion values shown in Appendix C it can be observed that the main contributor for the total ΔV is the dispersion. This can be seen by how the peaks in the dispersion correlate with the peaks in the individual correction values.

Regarding the set of 0.1 days arcs tracking window configuration for the PSO case, it could be that it is not sustainable in the long run or that the optimization problem is not well defined and needs adjustments. For example, it could be that with the reduction of the arc lengths, a new arc and thus a new correction maneuver might fit within the 28-day span. However, the number is arcs is fixed in the beginning based on the default with the 1.0 days arc length, 3.0 days arc interval configuration. Because this arc is not included, the optimization routine can give an unrealistic approximation of the full annual costs as the simulation underestimates the cost in the 14-day time frame.

For that reason, the simulation is also run for a longer duration. This is done in Section 5.4.2. It was decided to continue with the PSO algorithm as the optimization method for the following analyses because of the better susceptibility for higher dimensional search spaces.

Total maneuver costs
Similarly to the previous section, the station keeping costs are shown in the same fashion. The magnitude of the bars corresponding to the full duration are bigger due to the larger influence of estimation errors. However, after 14 days, the variation in costs is negligible. Both optimization methods yield an improved cost over the default scenario and show robustness to variation in measurement noise in the "stable" phase 14 days after the start of the simulation. Comparing Figure 5.35 with Figure 5.36 respectively, one can state that the reductions are approximately 30 and 47%.

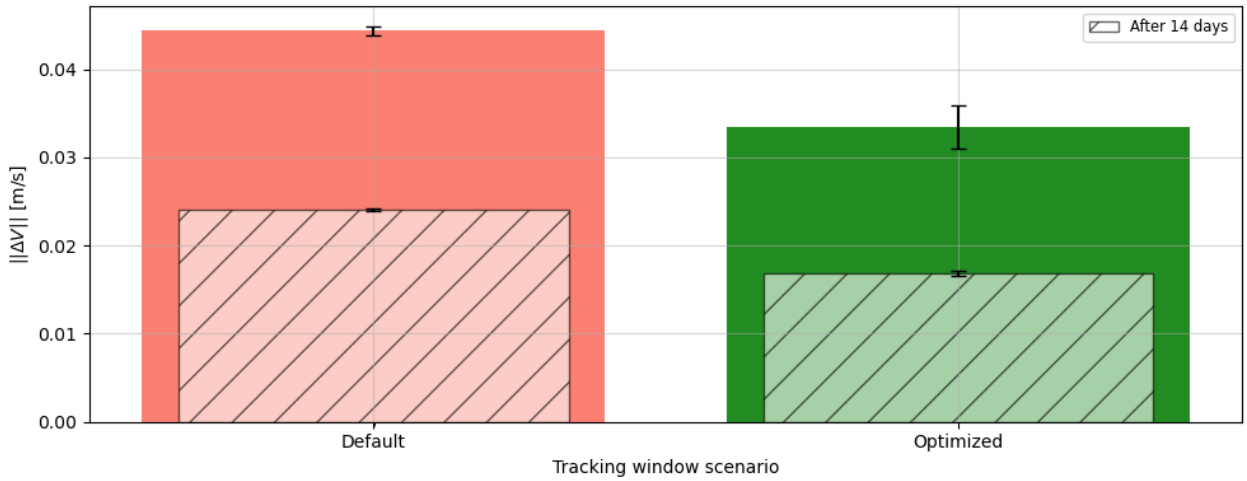

Figure 5.35: Default and optimized station keeping costs resulting from the Nelder-Mead optimization method for 28 days (run 1 of 5)

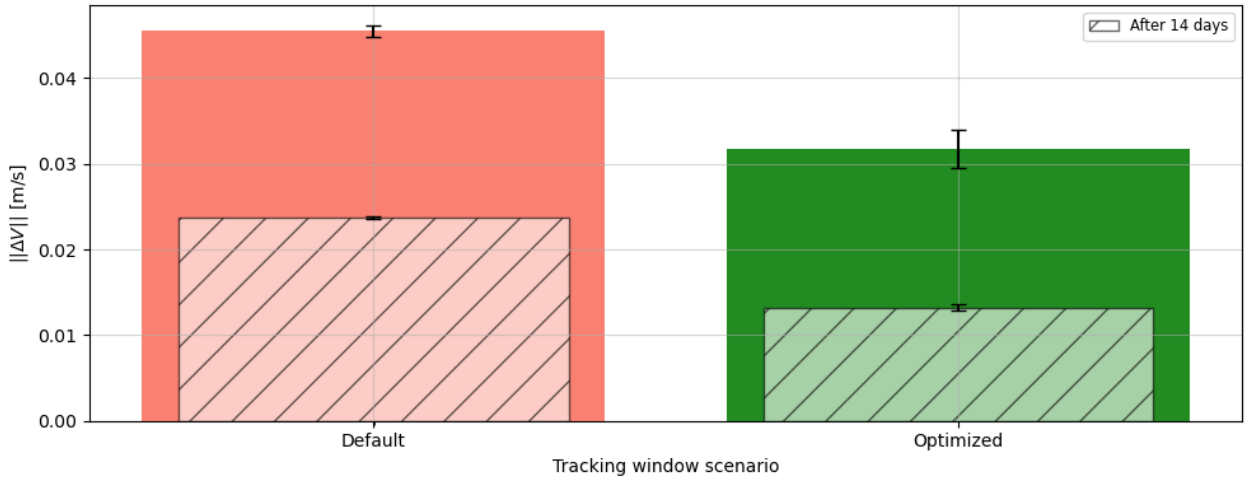

Figure 5.36: Default and optimized station keeping costs resulting from the PSO optimization method for 28 days (run 1 of 5)

The overview of the costs associated with all 5 solutions found per optimization method is show in Figure 5.37. It clearly shows that reductions can be made for each run. However, the PSO algorithm is able to find solutions that have an overall larger reduction. Because of these larger reductions, only this algorithm will be used for the rest of the analysis.

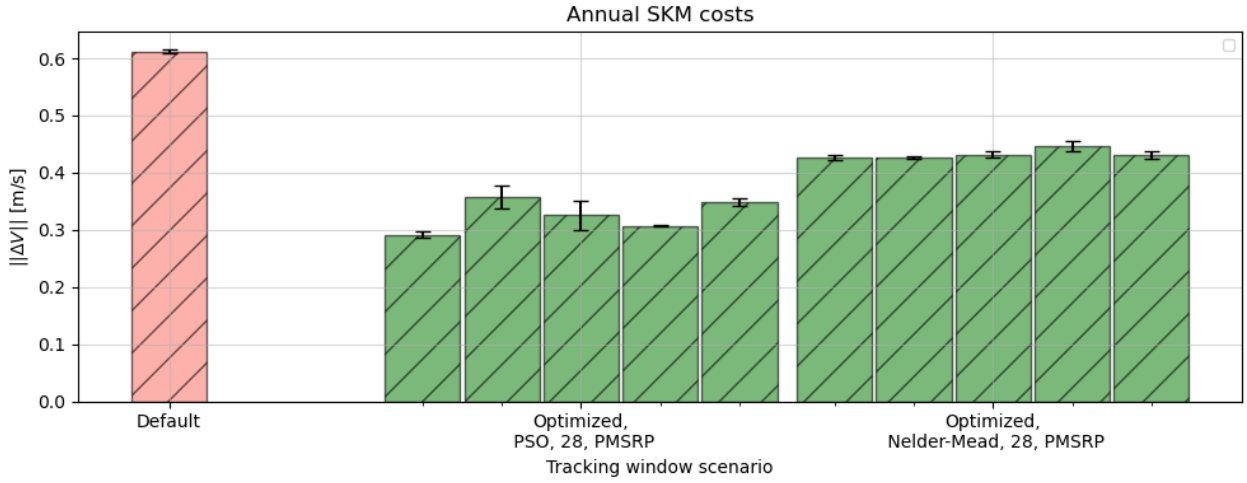

Figure 5.37: Overview of annual station keeping costs for the PSO and Nelder-Mead optimization methods

5.4.2. Varying model duration

As was suggested based on Figure 5.34, the reduction of the final arcs might give a skewed result for the final arcs near the end of the 28 days. This section aims to look into how the approximation of the ΔV is different when considering double the simulation time, so 56 days. The objective function in consideration is still the sum of the individual corrections after day 14 with respect to the start of the simulation.

Observation windows

Figure 5.38 does not show the same pattern in the first 28 days as shown in Figure 5.34. However, the final arc is still 0.1 days. Most arcs look almost similar in this time frame in terms of their timing. Nonetheless, note how much individual corrections can be reduced in ΔV with little variations in the arc. This indicates that minor changes to the mission planning regarding tracking can lead to a significant improvement. This might have to do with the larger design space (more design variables) and a need for more iterations before a better convergence is reached.

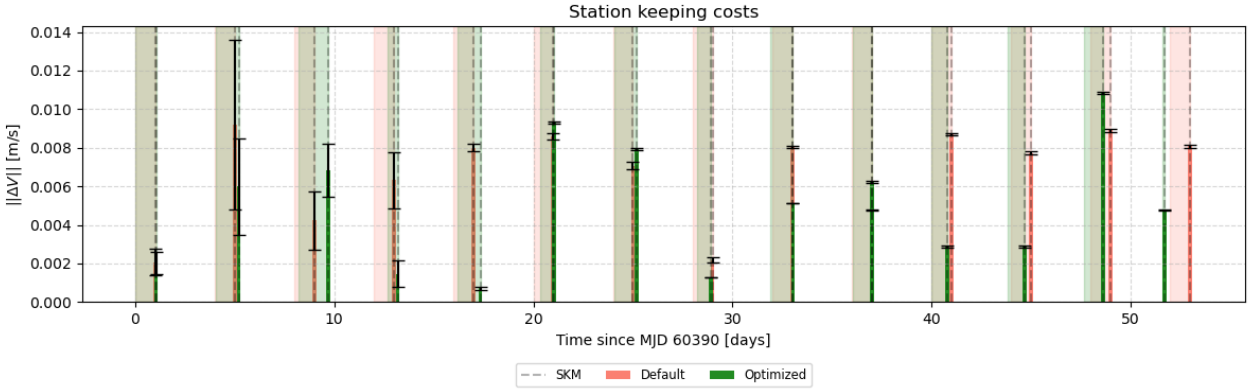

Figure 5.38: Default and optimized tracking configuration resulting from the PSO optimization method for 56 days (run 1 of 5)

Total maneuver costs

Because of the increase in total duration, the total costs naturally increase as well. Regardless, it is proven that reductions in costs can be made not just in the simulation for 28 days, but also for the longer time frame of 56 days. The error bars shown in Figure 5.39 are even smaller than in Figure 5.36, which implies that estimation errors have less and less of an effect on the maneuver cost as the mission duration increases.

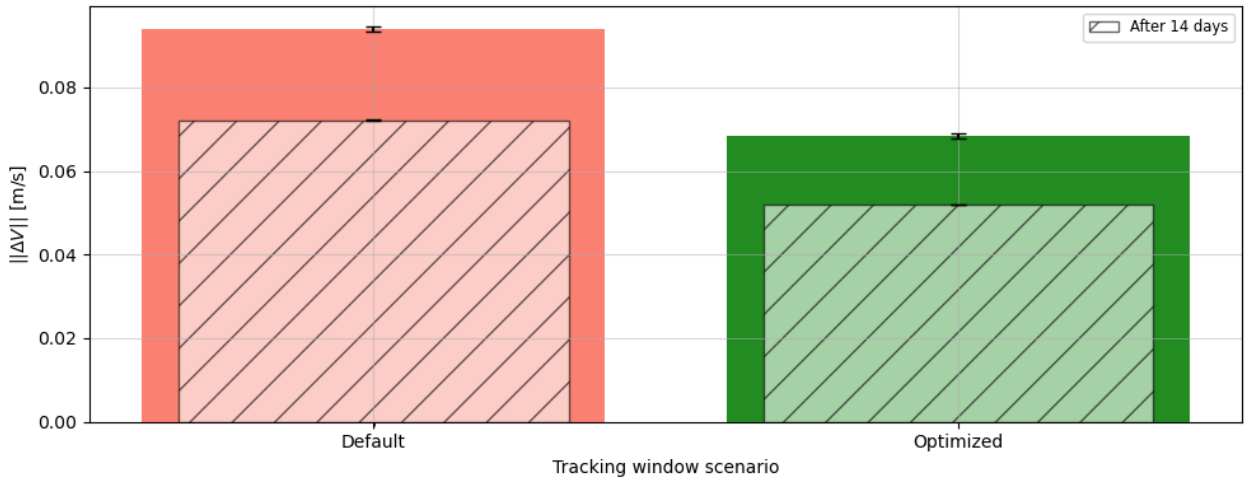

Figure 5.39: Default and optimized station keeping costs resulting from the PSO optimization method for 56 days (run 1 of 5)

5.4.3. Varying model fidelity

Comparing Figure 5.40 to Figure 5.34, one can observe that the results are largely the same, indicating that the choice of the model does not much affect the total cost estimate.

Observation windows

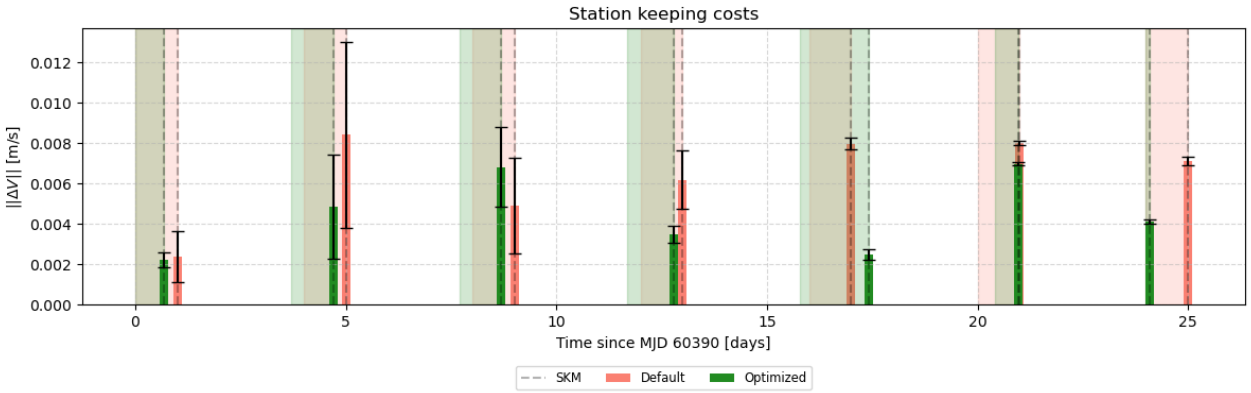

Figure 5.40: Default and optimized tracking configuration resulting from the PSO optimization method using SHSRP dynamics (run 1 of 5)

Total maneuver costs

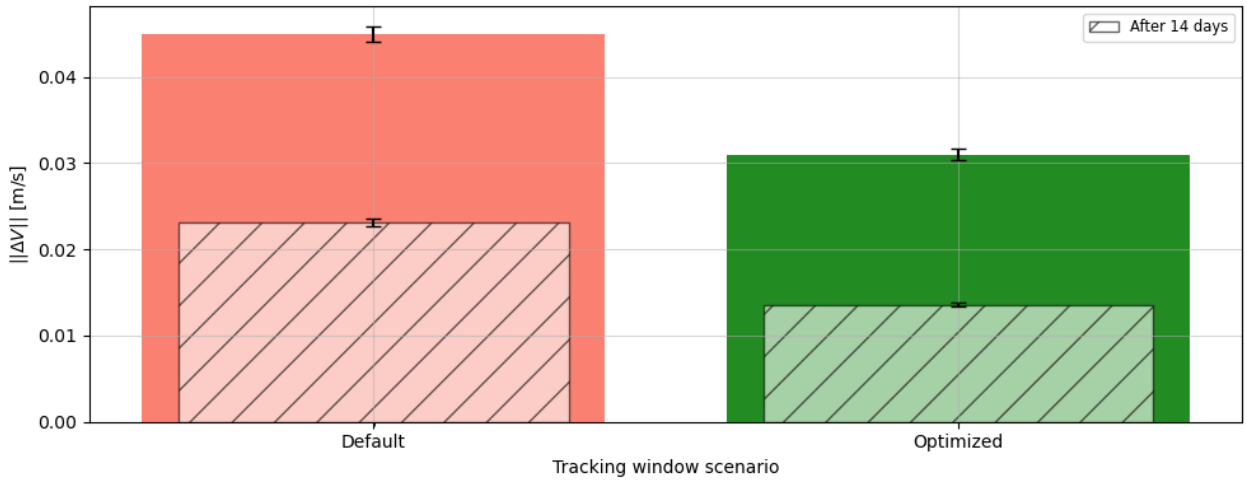

Figure 5.41: Default and optimized station keeping costs resulting from the PSO optimization method for 28 days with SHSRP instead of PMSRP dynamic model (run 1 of 5)

5.4.4. Summary

The main goal is to approximate the cost for the full 1-year operations. This section aims to provide the final values for the annual cost approximation for the different optimization cases shown above. As mentioned in the introduction of this section, there are a total of 5 MC runs per case that lead to different optimization results and those details are found in Appendix C. Figure 5.42 shows the approximated annual costs associated with the three cases for each of the 5 runs. Clearly, all results show that there is an improvement compared to the default scenario. An important aspect to notice is that simulating for 56 days instead of 28 days always yields a larger cost. Also, simulating with a PMSRP model instead of a SHSRP model does not yield drastic differences in the cost approximation. As such, it could be sufficient to use the PMSRP model for the analysis.

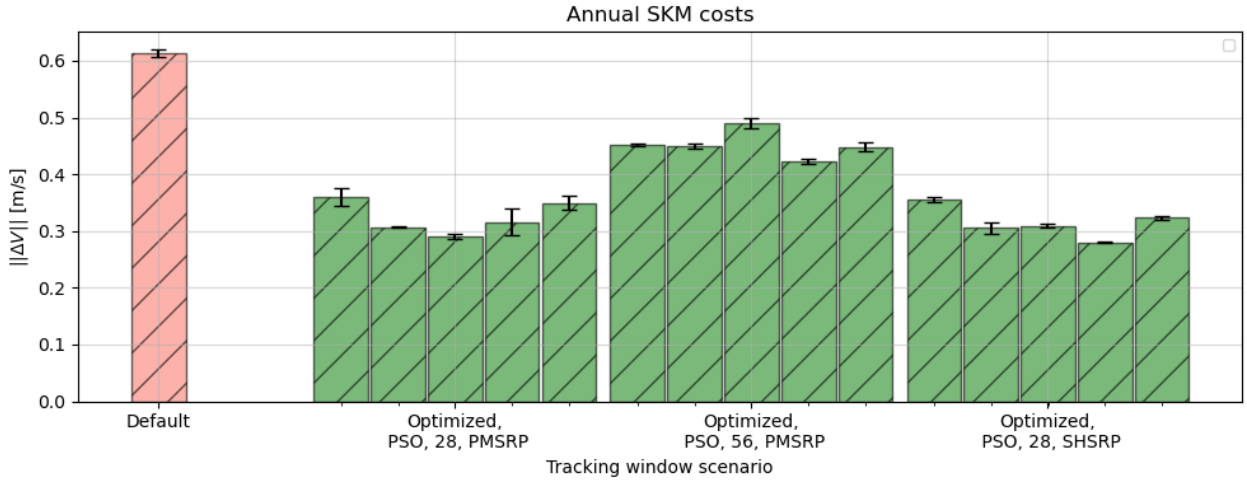

Figure 5.42: Overview of annual station keeping costs for various optimization cases using the PSO method

All in all, the optimization analysis shows that there are improvements with respect to not only the default scenario, but also all other solutions shown in Table 5.2. For example, the first optimized solution in Figure 5.42 for the 28 days case shows that an annual cost below 0.3 m/s can be reached or a reduction more than 50% with respect to the default scenario. However, it should be mentioned that the 28 days case might not provide the most trustworthy result, as modeling for 56 days seems to increase the annual ΔV to the 0.4 m/s to 0.5 m/s range.

	Configuration	Annual ΔV [m/s]	Reduction [%]
Constant arcs			
Default	Arc length: 1.0 day Arc interval: 3.0 day	0.613 $\pm$ 0.0066 1σ	-00.000 $\pm$ 1.077 1σ
Best	Arc length: 0.5 day Arc interval: 0.5 day	0.375 $\pm$ 0.0020 1σ	-38.597 $\pm$ 0.228 1σ
Orbit based			
Perilune	Arc length: 0.15 day Arc interval: Every 6 passes	0.505 $\pm$ 0.0124 1σ	-17.618 $\pm$ 2.023 1σ
Apolune	Arc length: 0.15 day Arc interval: Every 4 passes	0.498 $\pm$ 0.0082 1σ	-18.760 $\pm$ 1.337 1σ
Optimized	[1.62, 1.13, 1.17, 0.10, ...0.23, 0.10, 0.10] and other See Appendix C for more	0.280 $\pm$ 0.0134 1σ	-54.323 $\pm$ 2.186 1σ

Table 5.6: Final overview of the best annual total station keeping cost per tracking window configuration case

5.5. Operational implications

This chapter has shown that adjusting tracking arcs allows for a significant reduction of the total annual maneuver cost. This section explains the positive implications that this has on the operational considerations of the LUMIO mission. Section 5.5.1 elaborates on the constraints related to the propulsion subsystems, in particular about the feasibility of using the currently proposed propulsion subsystems in the optimized tracking scenarios found in this thesis work. Section 5.5.2 looks further than ΔV by looking at another design budget: power. Section 5.5.3 explains the key operational notes that can be derived from the optimized tracking scenario.

5.5.1. Subsystem feasibility

The capabilities of a spacecraft propulsion subsystem are crucial for determining the performance of the correction maneuvers. Typically, this involves understanding the design requirements related to both the minimum and maximum thrust levels as well as the burn time associated with the corrections. The LUMIO phase A study suggested two COTS candidates for the main propulsion system [4]:

- The EPSS system produced by NanoAvionics [133]
- Propulsion system produced by Bradford-ECAPS, specifically the flight-proven HPGP 1N thruster [134].

Based on the publicly available product specifications, the range of possible ΔV can be approximated to validate the feasibility of performing the corrections resulting from the simulations in a real setting. Total impulse I is defined as the product of thrust T and burn time t.

$$I = Tt \tag{5.1}$$

The value of ΔV is derived by dividing the total impulse by the spacecraft's mass m.

$$\Delta V = \frac{I}{m} \tag{5.2}$$

Both subsystems have the same thrust capabilities. The burn time will typically be a requirement depending on the details of all trajectories occurring throughout the entire mission. The data sheets did not provide sufficient information to derive the burn time limits, so assumed values are derived from the thrust and impulse information found in data sheets. For the given subsystems, either only the minimum or maximum impulse are provided in the data sheets. The same thing is true for the burn time. Although it is a rough assumption, the maximum of the one is considered for the other and vice versa for the minimum impulse. The assumed values are indicated by means of an asterisk. Table 5.7 shows the resulting ΔV envelope.

	Subsystem	
Parameter	**NanoAvionics**	**Bradford-ECAPS**
Thrust		
Min	0.25 N	0.25 N
Max	1 N	1 N
Inpulse		
Min	0.070 Ns*	0.070 Ns
Max	1700 Ns	1700 Ns*
Burn time		
Min	0.07 s*	0.07 s
Max	6800 s	6800 s*
Correction		
Min	0.003 m/s*	0.003 m/s
Max	74.56 m/s	74.56 m/s*

Table 5.7: LUMIO propulsion subsystem characteristics envelope

The most important take-away from this work is that the respective propulsion products can perform most of the corrections that will be required in the optimized tracking window scenarios. This is because the majority of the magnitudes of the required individual corrections reside within the upper and lower bounds of possible ΔV as shown in Table 5.7. Due to the lower ΔV limit, the mission design is constrained by this. A sensitivity analysis based on this *minimal* ΔV *threshold* was done in Section 5.3, but with arbitrary values. With the lower bound value of 0.003 m/s of Table 5.7, a similar analysis can be done.

While some corrections might be skipped due to the lower technical limit of the propulsion systems, Figure 5.44 shows that there is still an improvement in ΔV over the default configuration of Figure 5.43. Red resembles the minimal threshold associated with the currently used propulsion system of LUMIO. Note how the red annual ΔV remains smaller in Figure 5.44 than in Figure 5.43. Regardless, it shows that the optimized solution cost goes from 0.291 m/s to 0.5474 m/s. This means that it is still yielding improved costs over the default case, but the optimization effect has reduced substantially.

Regarding burn times, considering the fact that this work assumes instantaneous corrections, since the individual corrections correspond with small burn times in Table 5.7 it can be concluded that this assumption is valid.

Regarding the upper limit of ΔV, note that while theoretically possible, such long burn durations are impractical due to propellant limitations. The need for ΔV values in this order of magnitude also did not occur in this work. Therefore, the maximum total impulse is largely theoretical and not considered relevant.

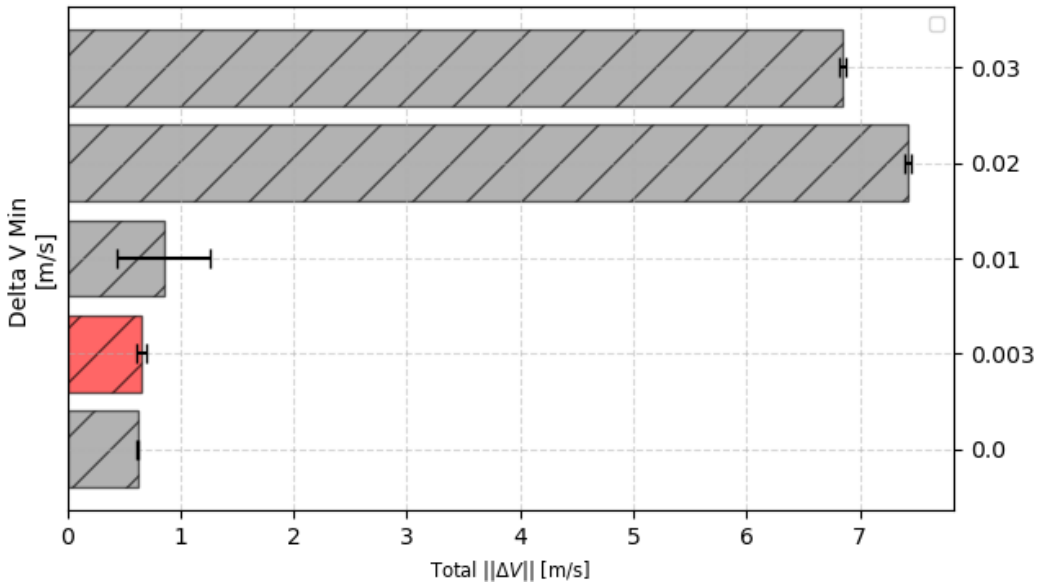

Figure 5.43: Comparison of annual SKM costs for different ΔV thresholds for the default tracking arc configuration

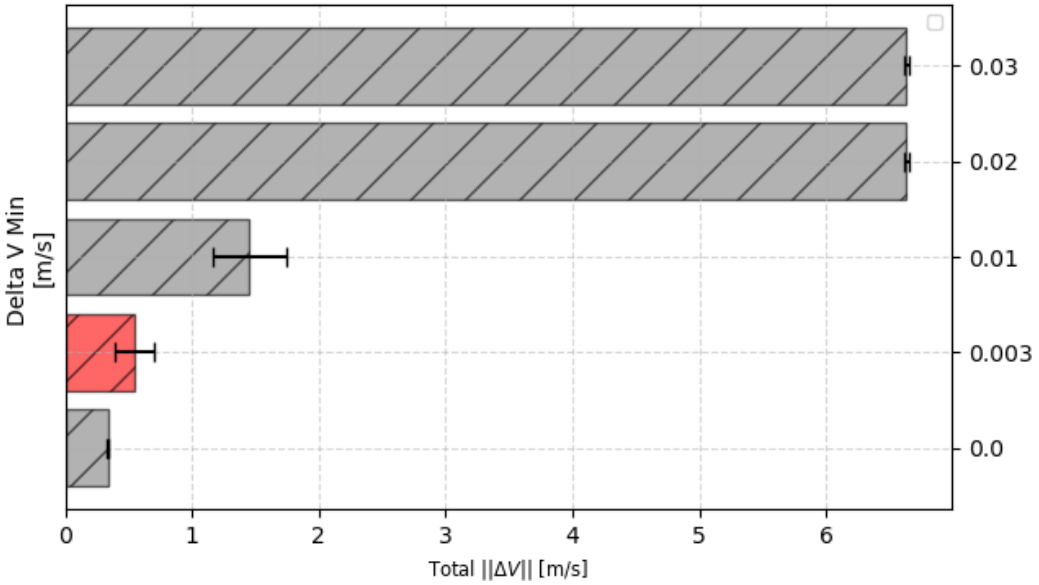

Figure 5.44: Comparison of annual SKM costs for different ΔV thresholds for an optimized tracking arc configuration (PSO, 28 days, PMSRP run 1 of 5)

An important aspect to note is that Figure 5.44 shows what happens when a threshold is applied to a tracking window configuration that is the result of an optimization routine that was performed with a threshold of 0 m/s. Running the same optimization algorithm (PSO) while including the newly defined threshold of 0.003 m/s can introduce other solutions for the window configurations. Figure 5.45 compares the annual cost associated with optimized solutions for excluding and including these thresholds. Additionally, another case is included that aims to show what happens when a longer simulation duration is chosen to investigate to what extend this might affect the annual ΔV results.

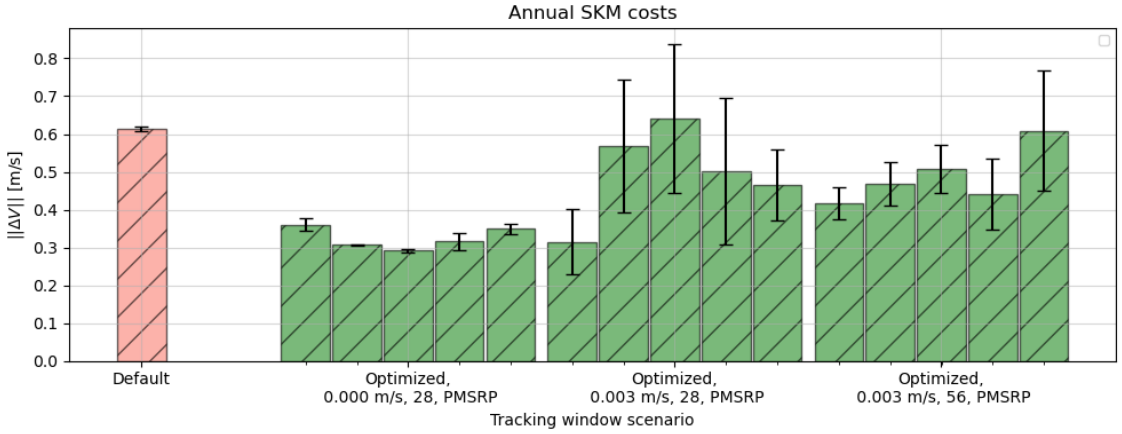

Figure 5.45: Comparison of annual SKM costs of PSO optimization results for different ΔV thresholds and simulation duration

Clearly, the threshold results in overall larger costs. Additionally, a threshold includes more uncertainty in the costs approximations. This is expected since a 28-day simulation only includes a representable period of 14 days for the calculations, which means that differences between Monte Carlo runs are larger as skipping tracking sessions has a relatively larger effect on the total cost. Considering a longer duration of 56 days reduces variation in the means cost value but also the spread in costs for a given case. This confirms that simulating over a longer time frame provides more stable solutions in a more realistic mission scenario.

5.5.2. Effects on power budget

There are also effects on the required power as a result of the changes in the configurations of tracking timing. Three main subsystems are highlighted with regards to power that are considered relevant in the context of orbit determination and navigation: transponder, thruster and on-board computer.

Subsystem	Model	Power requirements	Comments
Transponder	IMT X-BAND Transponder	STBY: 7.4 W RX: 12.8W RX & TX: 94.4W @ 15W P_{out}	STBY when not tracking RX&TX when tracking 19W @ 3dbW (2W) P_{out}
Thruster	1N HPGP Thruster	10W	During 2 hours of tank heating
OBC	SIRIUS-OBC-LEON3FT	1.3W	Runs during entire mission

Table 5.8: Power specifications of subsystems relevant for orbit determination and navigation

From Table 5.8 is it clear that the transponder uses multiple power modes that depend on whether tracking is performed or not. While using two-way ranging, it should be noted that the output power will not be 15W. According to T. Tanis [29], a transmission output power of 3dBW, or approximately 2W, is deemed sufficient for autonomous navigation operations. Because of this, the total power can be reduced by scaling to this power output. First one finds the transponder efficiency by:

$$\eta = \frac{P_{out}}{P_{in}} = \frac{15}{94.4 - 7.4} = 0.172 \tag{5.3}$$

With a power of 2W, this equates to a required input power of

$$P_{in} = \frac{2}{0.172} = 11.6W \tag{5.4}$$

Combine this with the standby power and one gets 19W during the tracking phase. Note that this value remains below the average power of 22 to 27W that is expected to be generated by the Electrical Power System (EPS) of LUMIO [4] which means that it is a legit value. In order to have an indication of the expected power over the mission due to the OD and navigation related tasks, an ”average power” value is used. The required power of the three components are weighted by the time fraction in which they are on or off compared to the total duration. Since different tracking configurations have different total tracking times and different amounts of tracking arcs, their average power is different. As a consequence for the mission design, this difference in power demand can affect how one allocates power on-board. This can lead to design changes and might lead to better scientific yield. From Figure 5.46 and Figure 5.47 it becomes clear that there is a trade-off to be made between ΔV and power consumption. Figure 5.46 shows the best costs as a visual representation of what is shown in Table 5.6 and explained extensively throughout Section 5.2.2 and Section 5.4.

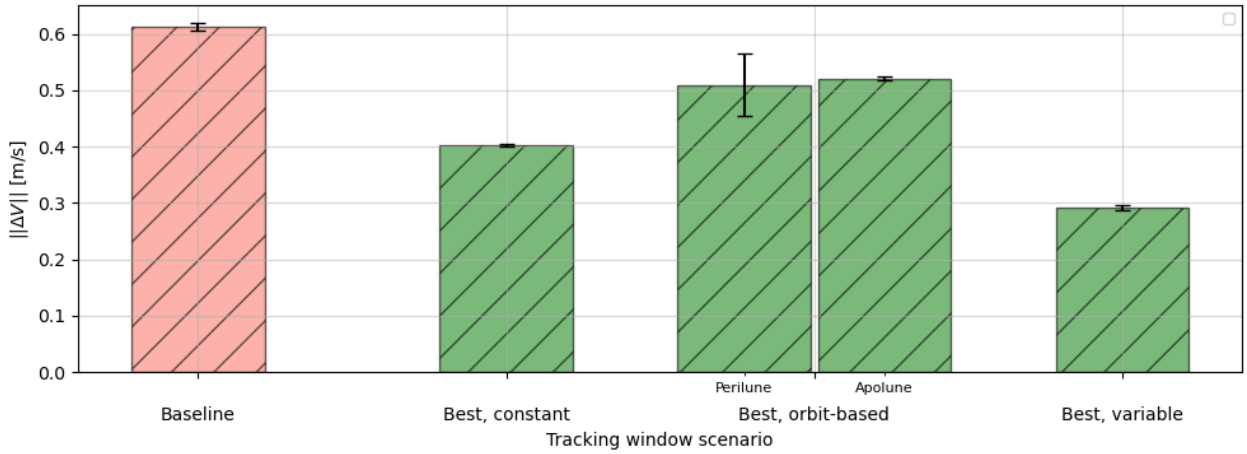

Figure 5.46: Annual station keeping costs for the best solution of each timing configuration type

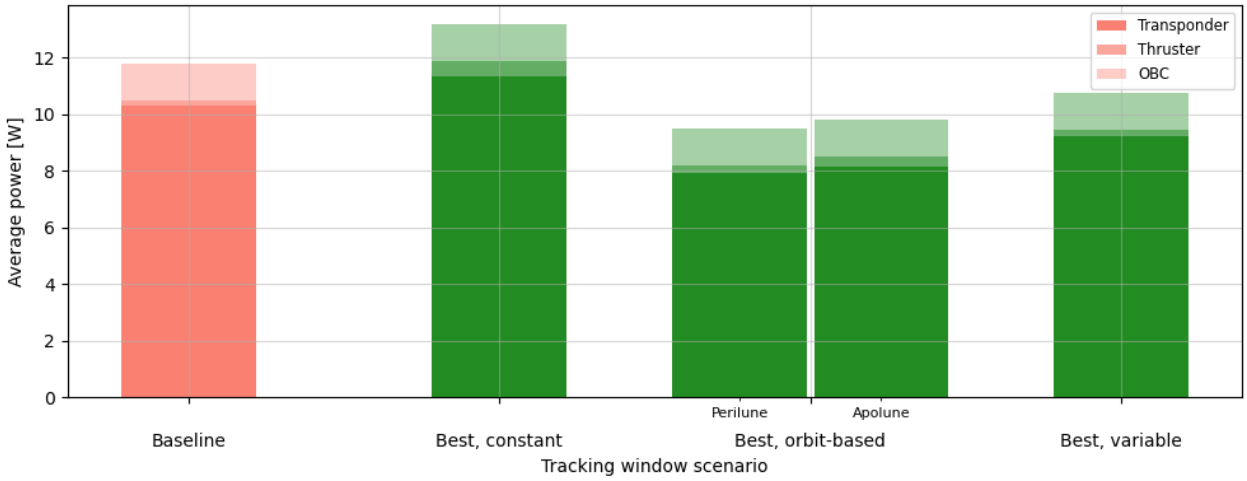

Figure 5.47: Averaged power consumption for subsystems for the best solution of each timing configuration type

Note how better options for ΔV do not necessarily lead to better power consumption. Tracking with a constant configuration shows to be better than the orbit-based tracking in terms of ΔV, but is worse in terms of power, also compared to the baseline. The worse result for the constant-type configuration is the result of the relatively large tracking time for this configuration. This shows that the use of less complex configurations comes at the cost of high tracking time and higher power requirements. A result with variable arcs, originating from the PSO optimization routine, shows that improvements are made in both ΔV and power, which are both smaller than the baseline and constant-type configuration. The orbit-based configurations score better on the power, but the variable configuration is still better in terms of ΔV. The details on the SKM and power budgets for all optimized results of this chapter can be found in Section C.1.

5.5.3. Consequential benefits of the optimization

The reduction of annual ΔV yields various operational benefits as a consequence. The main benefits are listed below:

- **More availability for scientific goals**
  It was shown for the optimized tracking window configurations that the tracking duration can be significantly reduced, such as shown in the last two arcs in Figure 5.34 and some other cases from Appendix C. One of the benefits of this is that the spacecraft can save on-board power as less signals have to be sent, which means that power savings can be reallocated to enhance the performance of scientific instruments, allowing for more accurate measurements, higher data transmission rates, or improved maneuverability.

- **Extended mission duration**
  Additionally, the spacecraft can operate for a longer period, extending the mission's duration and allowing for more data collection and exploration. This is more sustainable from both a financial and environmental perspective if new spacecraft have to be launched that serve as a continuation of the mission. Since one deals with two spacecraft tracking at the same time, these benefits exist for both spacecraft.

- **Applicability with existing propulsion systems**
  As was mentioned in Section 5.5.1, it is still possible to use the propulsion subsystems that are current used for LUMIO, albeit with a reduction in ΔV with respect to an ideal threshold of 0 m/s. All in all, from this analysis it can be concluded that the simulation results fall within the region where COTS products can be used.

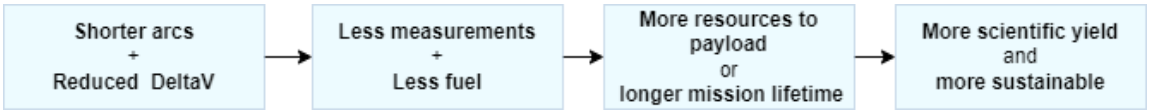

Figure 5.48: Benefits as a result of tracking timing optimization

Part III

Closing Remarks

6

Conclusions and Recommendations

6.1. Conclusions

This study focused on orbit determination and navigation analysis with the goal to explore the options to reduce the station keeping costs, defined by annual ΔV, through adjusting the timing of inter-satellite tracking windows. The analysis in this work was based on a case study in which a L_2 LPO (LUMIO) - ELO (LPF) satellite pair performs orbit determination and navigation based on inter-satellite two-way ranging in a simplified scenario with no dynamic model errors or noise bias. The orbit corrections are assumed to occur at the end of an estimation arc that uses the Batch-Least Squares estimator. Initial observation windows were defined as a set of tracking arcs of 1.0 day with a 3.0-day interval between each arc, based a 4-day correction maneuver interval that is suggested in literature as being the best for station keeping in LPOs. This scenario formed the baseline for a comparative analysis on tracking window configurations and auxiliary model parameters to evaluate the influence of those parameters on the optimization objective of reduced ΔV for one year of operations of LUMIO. Additionally, other mission and design aspects were identified that can aid in the design and operations of future missions. The research question was defined as the following:

"What is an optimal satellite-to-satellite tracking timing configuration for cislunar orbiters?"

A methodology was set up that aimed to compare three different timing strategy categories for which tracking can be performed with varying levels of complexity: tracking based on constant tracking duration and interval, tracking around the perilune or apolune of the LPF satellite, and tracking based on the solution of a heuristic optimization routine that adjusts each tracking arc individually. The best of each case was compared with the baseline scenario. For this baseline, the predicted annual navigation cost equated to a ΔV of 0.613$\pm$0.0066 1σ m/s. The overarching conclusion of this work is that improvements can be made compared to this value in each of the three strategy categories, but with varying levels of ΔV. From this analysis, the main conclusions are as follows:

- Firstly, for the constant-based tracking configuration the best ΔV comes from a scenario with an arc length-interval combination of 0.5-0.5 days, yielding an annual ΔV of 0.375$\pm$0.0020 1σ m/s or a reduction of 38.597$\pm$0.228 1σ % with respect to the baseline scenario. The benefit of this configuration is that it is simple to implement for its predictability. However, the fraction of tracking time to the total mission duration is quite large at 50%. As a result, the averaged power consumption, mostly driven by the transponder, is the largest of all categories due to the longer total tracking fraction with a average power consumption of 13.19W (baseline of 11.80W).

- Secondly, the orbit-based category showed that ΔV depends strongly on the amount of apolune or perilune passes between arcs. The best result was found when tracking every 6 and 4 passes, for perilune and apolune respectively, using a 0.15-day arc. Both of these configurations yield a mean annual ΔV near 0.5 m/s. While this reduction is smaller than for the constant-type category, a benefit is that, given

the short arcs, the power is reduced much more to both around 9.47W for the perilune case and and 9.82W for the apolune case.

- Lastly, multiple timing configurations with individually adjusted arcs were generated. Of these, it was shown that a ΔV down to 0.280$\pm$0.0134 1σ m/s can be realized, using the PSO algorithm. With a 54.323$\pm$2.186 1σ % reduction with respect to the baseline, this is a substantial improvement not just over the baseline, but also compared to the other two timing categories. Additionally, and conveniently, this configuration showed to contain short arcs down to the lower limit of 0.1 days, which, as a result, also reduced the average required power to 10.74W and thus yielded an improvement over the baseline in terms of the power budget as well.

For the exact numbers on costs, see Table 5.2. For an overview of the relevant subsystem power values, see Table 5.8. Besides the main research question, the answers to the sub questions below aim to further solidify the choices and conclusions of this work.

What are the working principles of inter-satellite based autonomous navigation?

In the context of the case study, the purpose of navigation is to follow an externally provided reference trajectory of the LUMIO spacecraft. Due to the unstable nature of LUMIO's orbit, station keeping is required. The accuracy of the station keeping maneuvers depends on two main principles: estimation error and dispersion.

Firstly, the estimation error depends on how well observations lead to a unique solution for the state vector that defines the two-satellite system. Two types of estimators exist: sequential and batch. Their main difference lies in the frequency at which the state estimates are updated. For sequential estimators, it is updated with each observation while the batch estimator first samples a set of observations and then performs Least-Squares operations to find the best estimate. A benefit of batch estimation with respect to sequential estimation is that the former is less susceptible to initial estimation errors than the latter and that the former is better at handling observation outliers. For those reasons, this batch estimation type was chosen for this work.

The second principle, dispersion, defines the difference between the true trajectory and the reference trajectory that a spacecraft should follow. This means that the corrections required for sustained navigation relies on proper orbit determination-which relies on the observational geometry-to obtain the best dispersion knowledge as possible to maintain on-course because insufficient state estimates wrongly define the true dispersion. This can lead to corrections that steer LUMIO in the wrong direction that diverts it from the reference trajectory. Another important factor is simply the shape of the orbit and the strength of the perturbation forces. In the context of LUMIO, as the annual ΔV increases with decreasing size of an LPO. Finally, for a given LPO, increasing the frequency of correction maneuvers can have a positive effect on the total ΔV, but this prevention of dispersion growth comes at the cost of more tracking and less time spent of the scientific targets of a mission.

How is the geometry of autonomous navigation observations related to improved system performance?

How well the estimator is able to solve the system states is determined by the degree of state observability that exists during tracking. For a system to be observable, at least one of the satellite orbits has to have a unique size, shape, and orientation due to an asymmetric gravity field. The degree of asymmetry strength can be quantified by comparing the acceleration magnitude caused by a perturbing force with the magnitude of the total of all accelerations acting on a satellite. This metric indicated that LPOs are good candidates for inter-satellite based orbit determination, because of the strong relative strength of the third body (Earth) in the region where those orbits reside.

However, it should be noted that constellations with similar orbits, such as two L_2 LPOs, are not always sufficient. This is due to the fact that, besides relatively large perturbation forces, there should also be sufficient variation in observational geometry, or vantage points, between the two satellites. Halo-Moon constellations are able to retrieve orbit information more quickly than Halo-Halo constellations because the dynamics of a

Moon orbit allows the system to acquire observations from many vantage points quickly. A constellation that consists of an elliptical lunar orbiter and a L_2 Lagrange point orbiter has proven to provide extended variation in observational geometry which made the scenario of LUMIO and LPF a good example to use in the context of inter-satellite autonomous navigation.

How does the fidelity of the on-board dynamic model influence the system performance?

The fidelity of the on-board model affects the estimation error and dispersion and consequentially the annual ΔV. Since this work does not consider dynamic model errors, the only observation error comes from observation noise and therefore the estimation error is not affected by the model fidelity. Simulations showed that after 14 days, the 3D RSS position error remains in the region around 10m (bound by a noise level of 2.98m 1σ) while the 3D RSS position dispersion resides around 800m. This means that the dispersion plays a much more significant role in the correction calculations than the estimation error because the dispersion proved to be orders of magnitude larger.

This work considered various fidelities, with models representing combinations of point masses of various planets, solar radiation pressure and various degrees and orders of spherical harmonics. The study identified that using a point mass model for the Earth, Moon, and Sun, combined with cannonball solar radiation pressure, called PMSRP01, offers the best balance between run time and the dispersion RMSE value of 14 days with respect to the LUMIO reference trajectory. The dispersion of a PM-type and SH-type model have the same RMSE values around $1 \cdot 10^5$, while including SRP decreases the RMSE value an order of magnitude to $8 \cdot 10^3$.

The fidelity also influences the run time required to propagate orbits used in estimation and correction calculations. The total time to calculate a maneuver with one target point of 3 days downstream with the PMSRP01 model, using LUMIO's current on-board computer equated to approximately 528s. It is still small compared to the period of LUMIO, tracking arc or the cut-off duration of 12h that is currently considered for LUMIO. The total run time value shows that this 12h time window is not required in the scenario of AOD, making corrections more accurate due to limited delays. Additionally, it shows that the on-board processor itself will not be a limitation for performing the calculations associated with AOD due to its relatively low power consumption of and processor capabilities that can calculate a correction sufficiently fast. Thus, no design change has to be made in this regard. More details were discussed in Section 5.1.

What parameters have a noticeable influence on the improvement of inter-satellite based autonomous navigation?

A sensitivity analysis was done which looked at the effects that various simulation parameters have on the annual ΔV. Results show that this parameter can be sensitive to the mission start epoch, suggesting that the cost results vary slightly depending on when the simulation starts. However, the variation in the sensitivity cases is three times smaller than the variation due to the choice of tracking arcs and intervals (0.1117 m/s versus 0.339 m/s and 0.5274 m/s respectively). A similar analysis over a longer simulation duration of 56 days showed that the dependency of start epoch is even smaller, which means that cost analyses are not strictly tied to simulations that start at a specific start condition only. There is a strong trend that shows that a shorter arc interval yields lower costs with means of annual ΔV ranging from 0.4518 to 0.9784 m/s in the range of 1.0-4.0 days. For different arc durations (0.1-2.0 days), using a duration of 0.5 days proved to be best in combination with the default interval of 3 days at 0.5290 m/s.

Regarding auxiliary parameters, the sensitivity analysis also showed that the annual ΔV is quite sensitive to the choice of a minimal ΔV threshold used to define whether an individual correction is done or not. This is an important factor related to the design of a mission because it connects the simulation results to the technical specifications of an actual propulsion subsystem that may be used on-board. The thrust and burn time characteristics of such subsystem should be such that the maneuvers that were calculated in the simulation can actually be performed. Given the capabilities of the current propulsion system chosen for LUMIO with a lower limit of 0.003 m/s, it was found that optimization solutions for the tracking configuration shows contain more variation in the annual ΔV. However, this variation is smaller when a longer simulation time

is chosen and improvements can still be made over the baseline configuration. The sensitivity analysis also showed that the selection of target points is a crucial part of the mission design because aiming too short or too far downstream leads to excessive over correction. While 3 days downstream offer a mean annual ΔV of 0.6131 m/s (the default setting), this increases to 2.2105 m/s for 5 days. Initial orbit insertion and estimation errors do not alter the long-term costs approximation as these effects stabilize after 14 days, further confirming that considering corrections only after 14 days provides a representative navigation scenario with stable conditions.

What are operational limitations and benefits associated with improved autonomous navigation performance?

Regarding the consequential benefits of the reduced station keeping costs as a result of the adjustment to the tracking scheduling, benefits were identified that positively impact the power and fuel budget considerations in spacecraft design. First of all, the ΔV budget is logically connected to a reduction on fuel, which means that one is able to operate the mission for a longer mission lifetime. Additionally, when one compares power consumption, improvements were also found in terms of a reduction in the total tracking time, as the optimized tracking configurations showed that one can track for an overall shorter amount of time compared to the baseline. This reduction in tracking time suggests that less energy could be spent on sending tracking signals by the transponder and, as a consequence, more power can be budgeted to the payload or allocated to other subsystems. Due to the longer mission lifetime, this can improve the scientific contribution of a mission as more scientific data can be generated. Lastly, this work has shown that the currently used subsystems of LUMIO can be used in the optimized settings as well. While the lower limit of the propulsion system has some effect on the total ΔV, improvements over a baseline can still be made. In other words, no major design alterations have to be made to ensure the station keep cost improvements.

The outcomes of this work did come with some caveats. The optimization algorithms used to obtain the solutions were sensitive to state estimate variations caused by measurement noise. This stochastic nature made it challenging to identify one single optimal tracking solution in the optimization process, resulting in rather a set of solutions than one globally best solution. The study also showed that short simulation periods might not adequately represent the full operational lifetime, suggesting that simulating the navigation process for a longer period of time is beneficial for accurate annual cost approximations. Rather than the technical feasibility, operationally there is also an aspect to be taken into account. While an improved tracking window solution is theoretically possible, it should be applicable with realistic operational considerations. For example, while a more complex tracking scheme could theoretically reduce costs, close cooperation is required between two spacecraft, which individually might be bound by constraints related to antenna pointing and science objectives. This study found that cost contributions stem more from dispersion growth than estimation errors, indicating that the focus of ΔV reduction is mostly a control problem than an orbit determination problem in the long term. Additionally, note that all findings are limited to the use case given in this study and can lead to different results for other orbit constellation configurations as this can affect state observability.

6.2. Recommendations for future research

This thesis work has made plenty of assumptions. Below, a set of suggestions are given for future analysis.

1. **Increase model realism**

   Include mission planning aspects
   This work assumed that LPF is essentially always at standby, ready to perform SST at any time. Future work should evaluate what the optimal tracking windows would be when one considers the effects of LPF's correction maneuvers. Additionally, both spacecraft have their own science objectives such as object observation or providing positioning or relay services for surface assets, which means that it might not always be possible to perform tracking as needs availability of both at the same time.

   Simulate over longer durations
   This work has shown that in some cases, the uncertainty in cost approximation growths as the representable period to base the annual cost on becomes smaller. This also has an effect on the solutions found using optimization algorithm, which leads to more variation in timing solutions as the objective space is more susceptible to larger variations with smaller simulation duration. It is therefore advised to perform the estimation with larger simulation durations, preferable for the full 1 year operations if computational resources allow for this. A similar statement can be made regarding the sensitivity analyses.

   Include spacecraft budget limitations
   Minimizing on-board power required for navigation improves the scientific goals of LUMIO as more power could be allocated towards the payload. An element related to this is considering a constraint on the maximum allowable inter satellite distance, which is related to the power limitations on the on-board antenna systems and subsequent signal quality, affecting the estimation and station-keeping process. Such distance upper limit restricts the orbit regions in which the tracking can be performed. Additionally, multi-objective optimization can be done in which more multiple budgets are looked at simultaneously. An example of such optimization would be to consider the station keeping costs combined with an objective of total tracking time. Another interesting aspect could be to optimize the sum of the station keeping costs or track duration of all satellites simultaneously, which minimizes those objectives over the constellation instead of just one satellite. This can be beneficial as it can reduce operational conflicts when one satellites cost objective is prioritized over the other.

   Include more constraints defined by mission design aspects
   This work assumed that LPF is essentially always at standby, ready to perform SST at any time. Future work should evaluate what the optimal tracking windows would be when one considers the effects of LPF's correction maneuvers. Additionally, both spacecraft have their own science objectives such as object observation or providing positioning or relay services for surface assets, which means that it might not always be possible to perform tracking as needs availability of both at the same time. Rather than the operational considerations, realism can be added from the perspective of the specifications of a spacecraft as well. For example, this study that the spacecraft are assumed to always be perfectly pointed towards each other. This simplifies the problem, but it is not realistic as correct antenna pointing is not always there. Ideally, the optimization problem should be extended by considering variables related to the ACDS and TT&C subsystems, yielding results on the effect of the delayed or in other way sub-optimal establishment of inter satellite connection. Coupled rotational-translational dynamics are possible within Tudatpy. For the CAPSTONE mission, constraints on the maximum antenna offset angle are set [31]. This is also the case for other missions performing SST. This is a logical design requirement to consider and would provide additional realism to the simulation.

   Include more advanced estimation model
   Regarding estimation, this work considered the BLS filter where the only estimated parameters are the initial states and it uses two-way range without measurement bias. In reality, there are inherent differences in the on-board model and reality. Additionally, effects related to clock synchronization, transmission and line delays add to bias [11]. Clock drift and aging can also accumulate over longer periods of time [11]. The estimator should incorporate these terms to estimate alongside the initial states. The

noise and bias could even be made adaptive, based on location in orbit as it could be a function of the pointing accuracy and object distance [59]. Another option could be to include consider parameters. Dynamic model parameters such as the SRP coefficient is currently considered without any uncertainty.

2. **Evaluate other orbit geometries**
   This work only considered the LPF and LUMIO study case. The orbit constellation geometries in this work was already known to work with range-only SST (albeit not with the BLS estimator). Other geometries might not work as efficiently, not at all and/or would have to be aided by means of additional (absolute) observables such as GNSS or lunar equivalent [45]. The objective of station-keeping cost in this context is not commonly researched, therefore allowing for the discovery of potential improvements.

3. **Include automatic on-board decision making**
   The methods described above entail an ”offline” method, the timing is planned before the navigation routine starts. Instead, timing could be done in real-time, adapting to unforeseen events. In this case, the latest state information known on-board is used to plan the next set of windows and SKMs. For example, events such as wrong satellite alignment or sudden malfunctions of any spacecraft's systems, could lead to a missed or shorted estimation arc. This might lead to larger deviation to the reference orbit as the SKM is conducted with a large error or canceled, shifting the characteristics of the future timing.

References

[1] M. Sweeting, "Modern Small Satellites-Changing the Economics of Space," *Proceedings of the IEEE*, vol. 106, no. 3, pp. 343–361, Mar. 2018, ISSN: 1558-2256. DOI: 10.1109/JPROC.2018.2806218.

[2] R. Botelho *et al.*, "A Unified Satellite Taxonomy Proposal Based on Mass and Size," vol. 04, pp. 57–73, Oct. 2019. DOI: 10.4236/aast.2019.44005.

[3] F. Pereira *et al.*, "Multi-Objective Design of a Lunar GNSS," en, *NAVIGATION: Journal of the Institute of Navigation*, vol. 69, no. 1, Mar. 2022, ISSN: 0028-1522, 2161-4296. DOI: 10.33012/navi.504.

[4] A. Cervone *et al.*, "LUMIO: A CubeSat for observing and characterizing micro-meteoroid impacts on the Lunar far side," en, *Acta Astronautica*, vol. 195, pp. 309–317, Jun. 2022, ISSN: 0094-5765. DOI: 10.1016/j.actaastro.2022.03.032.

[5] K. Kota *et al.*, "EQUULEUS Mission Analysis: Design of the Science Orbit Phase," in *International Symposium on Space Technology and Science 2017*, 2017.

[6] B. Cheetham *et al.*, "CAPSTONE: A Unique CubeSat Platform for a Navigation Demonstration in Cislunar Space," in *Ascend 2022*, American Institute of Aeronautics and Astronautics, 2022. DOI: 10.2514/6.2022-4382.

[7] Z. Towfic *et al.*, "Simulation and analysis of opportunistic MSPA for multiple cubesat deployments," in *SpaceOps Conference 2018*, American Institute of Aeronautics and Astronautics, May 2018. DOI: 10.2514/6.2018-2396.

[8] S. G. Hesar *et al.*, "Lunar far side surface navigation using Linked Autonomous Interplanetary Satellite Orbit Navigation (LiAISON)," en, *Acta Astronautica*, vol. 117, pp. 116–129, Dec. 2015, ISSN: 0094-5765. DOI: 10.1016/j.actaastro.2015.07.027.

[9] D. S. Abraham *et al.*, "Recommendations Emerging from an Analysis of NASA's Deep Space Communications Capacity," in ser. SpaceOps Conferences, American Institute of Aeronautics and Astronautics, May 2018. DOI: 10.2514/6.2018-2528.

[10] E. Turan *et al.*, "Autonomous navigation for deep space small satellites: Scientific and technological advances," en, *Acta Astronautica*, vol. 193, pp. 56–74, Apr. 2022, ISSN: 0094-5765. DOI: 10.1016/j.actaastro.2021.12.030.

[11] E. Turan *et al.*, "Autonomous Crosslink Radionavigation for a Lunar CubeSat Mission," *Frontiers in Space Technologies*, vol. 3, 2022, ISSN: 2673-5075. DOI: https://doi.org/10.3389/frspt.2022.919311.

[12] G. Sirbu *et al.*, "Fully Autonomous Orbit Determination and Synchronization for Satellite Navigation and Communication Systems in Halo Orbits," en, *Remote Sensing*, vol. 15, no. 5, p. 1173, Jan. 2023, ISSN: 2072-4292. DOI: 10.3390/rs15051173.

[13] T. Qin *et al.*, "Relative Orbit Determination Using Only Intersatellite Range Measurements," *Journal of Guidance, Control, and Dynamics*, vol. 42, no. 3, pp. 703–710, Mar. 2019, ISSN: 0731-5090. DOI: 10.2514/1.G003819.

[14] E. Turan *et al.*, "Autonomous Navigation Performance of Cislunar Orbits considering High Crosslink Measurement Errors," in *IEEE Aerospace Conference 2022*, ISSN: 1095-323X, Mar. 2022, pp. 1–11. DOI: 10.1109/AERO53065.2022.9843772.

[15] R. M. McGranaghan *et al.*, "Interplanetary Departure Stage Navigation by Means of Liaison Orbit Determination Architecture," NTRS Author Affiliations: Colorado Univ., Jet Propulsion Lab., California Inst. of Tech. NTRS Document ID: 20150007228 NTRS Research Center: Jet Propulsion Laboratory (JPL), Kauai, HI, Feb. 2013.

[16] J. A. Greaves *et al.*, "Autonomous Optical-Only Spacecraft-to-Spacecraft Absolute Tracking and Maneuver Classification in Cislunar Space," *Journal of Guidance, Control, and Dynamics*, vol. 46, no. 11, pp. 2092–2109, Nov. 2023, ISSN: 0731-5090. DOI: 10.2514/1.G007223.

[17] A. Grenier *et al.*, "Positioning and Velocity Performance Levels for a Lunar Lander using a Dedicated Lunar Communication and Navigation System," en, *NAVIGATION: Journal of the Institute of Navigation*, vol. 69, no. 2, Jun. 2022, ISSN: 0028-1522, 2161-4296. DOI: 10.33012/navi.513.

[18] A. Pasquale *et al.*, "Cislunar distributed architectures for communication and navigation services of lunar assets," *Acta Astronautica*, vol. 199, pp. 345–354, Oct. 2022, ISSN: 0094-5765. DOI: 10.1016/j.actaastro.2022.06.004.

[19] X. Zhang *et al.*, "Summary of Lunar Constellation Navigation and Orbit Determination Technology," en, *Aerospace*, vol. 11, no. 6, p. 497, Jun. 2024, ISSN: 2226-4310. DOI: 10.3390/aerospace11060497.

[20] K. A. Hill *et al.*, "Autonomous Orbit Determination from Lunar Halo Orbits Using Crosslink Range," *Journal of Spacecraft and Rockets*, vol. 45, no. 3, pp. 548–553, May 2008, ISSN: 0022-4650. DOI: 10.2514/1.32316.

[21] K. A. Hill, "Autonomous navigation in libration point orbits," Ph.D. dissertation, University of Colorado Boulder, Jan. 2007.

[22] E. Turan *et al.*, "Performance analysis of crosslink radiometric measurement based autonomous orbit determination for cislunar small satellite formations," en, *Advances in Space Research*, Nov. 2022, ISSN: 0273-1177. DOI: 10.1016/j.asr.2022.11.032.

[23] *Lunar Pathfinder*, en.

[24] M. Gupta, "Analysis of the Representation of Orbital Errors and Improvement of their Modelling," M.S. thesis, Luleå University of Technology, Sep. 2018.

[25] E. Turan *et al.*, "Particle Swarm Optimization Based Tracking Window Planning for Cislunar Orbiters Performing Autonomous Radiometric Navigation: 74th International Astronautical Congress (IAC)," *Proceedings of the 74th International Astronautical Congress (IAC)*, 2023.

[26] A. Bani Younes *et al.*, "High-order uncertainity propagation using state transition tensor series," *Advances in the Astronautical Sciences*, vol. 147, Jan. 2013.

[27] L. Zhang *et al.*, "A Universe Light House — Candidate Architectures of the Libration Point Satellite Navigation System," en, *The Journal of Navigation*, vol. 67, no. 5, pp. 737–752, Sep. 2014, ISSN: 0373-4633, 1469-7785. DOI: 10.1017/S0373463314000137.

[28] Q. Moon, "Cislunar Navigation Techniques and Navigation Performance Optimization," *All Graduate Theses and Dissertations, Spring 1920 to Summer 2023*, Aug. 2023. DOI: https://doi.org/10.26076/ec6f-9ef6.

[29] T. Tanis, "Autonomous Orbit Determination in Cislunar Space," en, M.S. thesis, Delft University of Technology, Aug. 2022.

[30] C. Giordano *et al.*, "Analysis, Design, and Optimization of Robust Trajectories in Cislunar Environment for Limited-Capability Spacecraft," en, *The Journal of the Astronautical Sciences*, vol. 70, no. 6, p. 53, Nov. 2023, ISSN: 2195-0571. DOI: 10.1007/s40295-023-00413-8.

[31] M. Thompson *et al.*, "Cislunar Navigation Technology Demonstrations on the CAPSTONE Mission," Jan. 2022. DOI: 10.33012/2022.18208.

[32] Y. Jin *et al.*, "A Modified Targeting Strategy for Station-Keeping of Libration Point Orbits in the Real Earth-Moon System," en, *International Journal of Aerospace Engineering*, vol. 2019, e3257514, Sep. 2019, ISSN: 1687-5966. DOI: 10.1155/2019/3257514.

[33] D. Davis *et al.*, "Orbit Maintenance and Navigation of Human Spacecraft at Cislunar Near Rectilinear Halo Orbits," in *27th AAS/AIAA Space Flight Mechanics Meeting*, Feb. 2017.

[34] S. Speretta *et al.*, "Designing the Radio Link for a Lunar CubeSat: The LUMIO Case," en, *72nd International Astronautical Conference*, 2021.

[35] Z.-Y. Gao *et al.*, "Comparison of Autonomous Orbit Determination for Satellite Pairs in Lunar Halo and Distant Retrograde Orbits," en, *NAVIGATION: Journal of the Institute of Navigation*, vol. 69, no. 2, Jun. 2022, ISSN: 0028-1522, 2161-4296. DOI: 10.33012/navi.522.

[36] M. T. Caudill, "A Relative Orbit Determination and Navigation Strategy for Lunar Gateway," en, M.S. thesis, University of Colorado Boulder, Jul. 2021.

[37] L. Deng *et al.*, "Analysis and Comparison on UKF and BLS for Orbit Determination," Aug. 2015.

[38] O. Montenbruck *et al.*, *Satellite Orbits: Methods, Models and Applications*. Springer, Jan. 2000, vol. 1, ISBN: 9783540672807. DOI: 10.1007/978-3-642-58351-3.

[39] A. Freeman, "Deep Space NanoSats - positioned for exponential growth," en, Tech. Rep., May 2016, Type: dataset.

[40] B. Tapley *et al.*, *Statistical Orbit Determination*. Elsevier, Jan. 2004, ISBN: ISBN: 0-12-683630-2.

[41] A. M. Al-Saegh *et al.*, "Atmospheric Propagation Model for Satellite Communications," en, in *MATLAB Applications for the Practical Engineer*, IntechOpen, Sep. 2014, ISBN: 9789535117193. DOI: 10.5772/58238.

[42] N. O. Harle *et al.*, "Lunar comms and nav infrastructure – first data relay orbiter Lunar Pathfinder, operational in 2024, paves the way for full constellation by 2030s," in *ASCEND 2021*, American Institute of Aeronautics and Astronautics. DOI: 10.2514/6.2021-4132.

[43] R. A. Carvalho, "Optimizing the Communication Capacity of a Ground Station Network," en, *Journal of Aerospace Technology and Management*, vol. 11, e2319, May 2019, ISSN: 2175-9146. DOI: 10.5028/jatm.v11.1026.

[44] P. Giordano *et al.*, "The Lunar Pathfinder PNT Experiment and Moonlight Navigation Service: The Future of Lunar Position, Navigation and Timing," en, Jan. 2022, pp. 632–642. DOI: 10.33012/2022.18225.

[45] J. J. R. Critchley-Marrows *et al.*, "Autonomous and Earth-Independent Orbit Determination for a Lunar Navigation Satellite System," en, *Aerospace*, vol. 11, no. 2, p. 153, Feb. 2024, ISSN: 2226-4310. DOI: 10.3390/aerospace11020153.

[46] A. M. Cipriano *et al.*, "Orbit Design for LUMIO: The Lunar Meteoroid Impacts Observer," *Frontiers in Astronomy and Space Sciences*, vol. 5, Sep. 2018, ISSN: 2296-987X. DOI: https://doi.org/10.3389/fspas.2018.00029.

[47] R. M. Suggs *et al.*, "The flux of kilogram-sized meteoroids from lunar impact monitoring," en, *Icarus*, vol. 238, pp. 23–36, Aug. 2014, ISSN: 0019-1035. DOI: 10.1016/j.icarus.2014.04.032.

[48] K. De Smaele, "Design of an Unsupervised Machine Learning Approach to Fault Detection for CubeSat AOCS: Applied to LUMIO: Lunar Meteoroid Impact Observer," en, M.S. thesis, Delft University of Technology, May 2023.

[49] S. Gelmi, "Fault Detection Isolation and Recovery for LUMIO mission: Algorithm and Methodology," en, M.S. thesis, Delft University of Technology, Sep. 2019.

[50] F. Nett, "On the Design of a Propulsion System for the Lunar Meteoroid Impact Observer (LUMIO)," en, M.S. thesis, Delft University of Technology, Oct. 2021.

[51] Y. Hu *et al.*, "Three-spacecraft autonomous orbit determination and observability analysis with inertial angles-only measurements," en, *Acta Astronautica*, vol. 170, pp. 106–121, May 2020, ISSN: 0094-5765. DOI: 10.1016/j.actaastro.2020.01.005.

[52] Y. Li *et al.*, "Observability analysis and autonomous navigation for two satellites with relative position measurements," en, *Acta Astronautica*, Fourth IAA Conference on Dynamics and Control of Space Systems (DYCOSS2018), vol. 163, pp. 77–86, Oct. 2019, ISSN: 0094-5765. DOI: 10.1016/j.actaastro.2019.02.030.

[53] S. Damico *et al.*, "Autonomous formation flying based on GPS - PRISMA flight results," English, *Acta Astronautica*, vol. 82, no. 1, pp. 69–79, 2013, ISSN: 0094-5765. DOI: 10.1016/j.actaastro.2012.04.033.

[54] K. Xiong *et al.*, "Autonomous navigation for a group of satellites with star sensors and inter-satellite links," English, *Acta Astronautica*, vol. 86, pp. 10–23, 2013, ISSN: 0094-5765. DOI: 10.1016/j.actaastro.2012.12.001.

[55] S. Hur-Diaz *et al.*, "Autonomous lunar orbit navigation using optical sensors," *Astrodynamics 2007 - Advances in the Astronautical Sciences, Proceedings of the AAS/AIAA Astrodynamics Specialist Conference*, Advances in the Astronautical Sciences, pp. 997–1014, 2008, ISSN: 9780877035435.

[56] M. B. Hinga *et al.*, "Autonomous Lunar L1 Halo Orbit Navigation Using Optical Measurements to a Lunar Landmark," en, *NAVIGATION: Journal of the Institute of Navigation*, vol. 70, no. 3, Sep. 2023, ISSN: 0028-1522, 2161-4296. DOI: 10.33012/navi.586.

[57] N. Bradley *et al.*, "Cislunar Navigation Accuracy Using Optical Observations of Natural and Artificial Targets," *Journal of Spacecraft and Rockets*, vol. 57, no. 4, pp. 777–792, Jul. 2020, ISSN: 0022-4650. DOI: 10.2514/1.A34694.

[58] P. Rocha Cachim *et al.*, "Autonomous orbit determination for satellite formations using relative sensing: Observability analysis and optimization," *Acta Astronautica*, vol. 200, pp. 301–315, Nov. 2022, ISSN: 0094-5765. DOI: 10.1016/j.actaastro.2022.08.009.

[59] W. Wang *et al.*, "Joint navigation performance of distant retrograde orbits and cislunar orbits via LiAlSON considering dynamic and clock model errors," en, *Navigation: Journal of the Institute of Navigation*, vol. 66, no. 4, pp. 781–802, 2019, ISSN: 2161-4296. DOI: 10.1002/navi.340.

[60] C. D. Murray *et al.*, *Solar System Dynamics*. Cambridge: Cambridge University Press, 2000, ISBN: 9780521575973. DOI: 10.1017/CBO9781139174817.

[61] E. Turan *et al.*, "Performance Analysis of Radiometric Autonomous Navigation for Lunar Satellite Network Topologies: 11th International Workshop on Satellite Constellations and Formation Flying," English, 11th International Workshop on Satellite Constellations and Formation Flying„ IWSCFF2022 ; Conference date: 07-06-2022 Through 08-06-2022, 2022.

[62] S. Mo *et al.*, "Multi-Satellite Relative Navigation Scheme for Microsatellites Using Inter-Satellite Radio Frequency Measurements," *Sensors (Basel, Switzerland)*, vol. 21, no. 11, p. 3725, May 2021, ISSN: 1424-8220. DOI: 10.3390/s21113725.

[63] A. Genova *et al.*, "Deep-Space Navigation with Intersatellite Radio Tracking," *Journal of Guidance, Control, and Dynamics*, vol. 44, no. 5, pp. 1068–1079, May 2021, ISSN: 0731-5090. DOI: 10.2514/1.G005610.

[64] Q. Su *et al.*, "Observability Analysis and Navigation Algorithm for Distributed Satellites System Using Relative Range Measurements," en, *Journal of Systems Science and Complexity*, vol. 31, no. 5, pp. 1206–1226, Oct. 2018, ISSN: 1559-7067. DOI: 10.1007/s11424-018-6096-1.

[65] M. Smith *et al.*, "The Artemis Program: An Overview of NASA's Activities to Return Humans to the Moon," in *2020 IEEE Aerospace Conference*, ISSN: 1095-323X, Mar. 2020, pp. 1–10. DOI: 10.1109/AERO47225.2020.9172323.

[66] L. Zhang *et al.*, "Navigation Performance of the Libration Point Satellite Navigation System in Cislunar Space," en, *The Journal of Navigation*, vol. 68, no. 2, pp. 367–382, Mar. 2015, ISSN: 0373-4633, 1469-7785. DOI: 10.1017/S0373463314000617.

[67] J. Parker *et al.*, "Navigation Between Geosynchronous and Lunar L1 Orbiters," in *AIAA/AAS Astrodynamics Specialist Conference*, American Institute of Aeronautics and Astronautics. DOI: 10.2514/6.2012-4878.

[68] J. S. Parker *et al.*, "Liaison-Supplemented Navigation of a Crewed Vehicle in a Lunar Halo Orbit," NTRS Author Affiliations: Colorado Univ., Jet Propulsion Lab., California Inst. of Tech. NTRS Report/Patent Number: AAS 13-776 NTRS Document ID: 20150008052 NTRS Research Center: Jet Propulsion Laboratory (JPL), Hilton Head, SC, Aug. 2013.

[69] A. G. Gad, "Particle Swarm Optimization Algorithm and Its Applications: A Systematic Review," en, *Archives of Computational Methods in Engineering*, vol. 29, no. 5, pp. 2531–2561, Aug. 2022, ISSN: 1886-1784. DOI: 10.1007/s11831-021-09694-4.

[70] N. Ré *et al.*, *Near Rectilinear Halo Orbit Determination with Simulated DSN Observations*. Jan. 2020. DOI: 10.2514/6.2020-1700.

[71] D. Lujan *et al.*, "Earth–Moon L2 Quasi-Halo Orbit Family: Characteristics and Manifold Applications," *Journal of Guidance, Control, and Dynamics*, vol. 45, no. 11, pp. 2029–2045, Nov. 2022, ISSN: 0731-5090. DOI: 10.2514/1.G006681.

[72] K. Hamera *et al.*, "An Evolvable Lunar Communication and Navigation Constellation Concept," in *IEEE Aerospace Conference 2008*, ISSN: 1095-323X, Mar. 2008, pp. 1–20. DOI: 10.1109/AERO.2008.4526326.

[73] K. Oshima, "The use of vertical instability of l1 and l2 planar Lyapunov orbits for transfers from near rectilinear halo orbits to planar distant retrograde orbits in the Earth–Moon system," en, *Celestial Mechanics and Dynamical Astronomy*, vol. 131, no. 3, p. 14, Mar. 2019, ISSN: 1572-9478. DOI: 10.1007/s10569-019-9892-6.

[74] D. A. Dei Tos *et al.*, "On the Advantages of Using a Strict Hierarchy to Model Astrodynamical Problems," Oct. 2015.

[75] Y. Gao *et al.*, "Research on the Effectiveness of Different Estimation Algorithm on the Autonomous Orbit Determination of Lagrangian Navigation Constellation," en, *International Journal of Aerospace Engineering*, vol. 2016, e8392148, Oct. 2016, ISSN: 1687-5966. DOI: 10.1155/2016/8392148.

[76] K. Bokelmann *et al.*, "Optimization of Impulsive Europa Capture Trajectories using Primer Vector Theory," *The Journal of the Astronautical Sciences*, vol. 67, May 2019. DOI: 10.1007/s40295-018-00146-z.

[77] J. S. Parker *et al.*, *Low-Energy Lunar Trajectory Design*, en. John Wiley & Sons, Jun. 2014, Google-Books-ID: KlrwAwAAQBAJ, ISBN: 9781118853870.

[78] Y. Tang *et al.*, "Effect of orbital shadow at an Earth-Moon Lagrange point on relay communication mission," en, *Science China Information Sciences*, vol. 60, no. 11, p. 112 301, Sep. 2017, ISSN: 1869-1919. DOI: 10.1007/s11432-016-9069-9.

[79] E. E. Fowler *et al.*, "Observability Metrics for Space-Based Cislunar Domain Awareness," en, *The Journal of the Astronautical Sciences*, vol. 70, no. 2, p. 10, Mar. 2023, ISSN: 2195-0571. DOI: 10.1007/s40295-023-00368-w.

[80] T. A. Pavlak *et al.*, "Evolution of the out-of-plane amplitude for quasi-periodic trajectories in the Earth–Moon system," *Acta Astronautica*, vol. 81, no. 2, pp. 456–465, Dec. 2012, ISSN: 0094-5765. DOI: 10.1016/j.actaastro.2012.07.025.

[81] J. L. Crassidis *et al.*, "Optimal Estimation of Dynamic Systems," en, in *IEEE Aerospace Conference 2008*, Chapman and Hall/CRC, Apr. 2004, ISBN: 9780203509128. DOI: 10.1201/9780203509128.

[82] A. Cano *et al.*, "Improving Orbital Uncertainty Realism Through Covariance Determination in GEO," en, *The Journal of the Astronautical Sciences*, vol. 69, no. 5, pp. 1394–1420, Oct. 2022, ISSN: 2195-0571. DOI: 10.1007/s40295-022-00343-x.

[83] M. E. Lisano, "Comparing Consider-Covariance Analysis with Sigma-Point Consider Filter and Linear-Theory Consider Filter Formulations," NTRS Author Affiliations: Jet Propulsion Lab., California Inst. of Tech. NTRS Document ID: 20080012709 NTRS Research Center: Goddard Space Flight Center (GSFC), Sep. 2007.

[84] D. Dirkx *et al.*, "The open-source astrodynamics Tudatpy software - overview for planetary mission design and science analysis," in *Europlanet Science Congress 2022*, Sep. 2022, EPSC2022–253. DOI: 10.5194/epsc2022-253.

[85] R. S. Park *et al.*, "Nonlinear Mapping of Gaussian Statistics: Theory and Applications to Spacecraft Trajectory Design," en, *Journal of Guidance, Control, and Dynamics*, vol. 29, no. 6, pp. 1367–1375, Nov. 2006, ISSN: 0731-5090, 1533-3884. DOI: 10.2514/1.20177.

[86] M. P. Ramachandran, "Approximate State Transition Matrix and Secular Orbit Model," en, *International Journal of Aerospace Engineering*, vol. 2015, no. 1, p. 475 742, 2015, ISSN: 1687-5974. DOI: 10.1155/2015/475742.

[87] J. L. Read *et al.*, "State Transition Matrix for Perturbed Orbital Motion Using Modified Chebyshev Picard Iteration," en, *The Journal of the Astronautical Sciences*, vol. 62, no. 2, pp. 148–167, Jun. 2015, ISSN: 2195-0571. DOI: 10.1007/s40295-015-0051-3.

[88] Y. Tsuda *et al.*, "State Transition Matrix Approximation Using a Generalized Averaging Method," *Journal of Guidance, Control, and Dynamics*, vol. 32, no. 6, pp. 1781–1794, 2009, ISSN: 0731-5090. DOI: 10.2514/1.44142.

[89] Y. Tsuda *et al.*, "Series Expansion Form of an Approximate State Transition Matrix for Fully Perturbed Orbits," *Transactions of the Japanese Society for Artificial Intelligence, Aerospace Technology Japan*, vol. 8, Oct. 2011. DOI: 10.2322/tastj.8.Pd_53.

[90] A. D. Dianetti *et al.*, "Application of Observability Analysis to Space Object Tracking," *AIAA Guidance, Navigation, and Control Conference*, AIAA SciTech Forum, Jan. 2017. DOI: 10.2514/6.2017-1258.

[91] T. A. Pavlak, "Trajectory design and orbit maintenance strategies in multi-body dynamical regimes," en, Ph.D. dissertation, Purdue University, Jan. 2013.

[92] D. Guzzetti *et al.*, "Rapid trajectory design in the Earth–Moon ephemeris system via an interactive catalog of periodic and quasi-periodic orbits," en, *Acta Astronautica*, Space Flight Safety, vol. 126, pp. 439–455, Sep. 2016, ISSN: 0094-5765. DOI: 10.1016/j.actaastro.2016.06.029.

[93] A. M. Friedman *et al.*, "Determining Debris Characteristics from Observability Analysis of Artificial Near-Earth Objects," de, 2017.

[94] D. Folta *et al.*, "Earth–Moon libration point orbit stationkeeping -Theory modeling, and operations," *Acta Astronautica*, vol. 94, Jan. 2013. DOI: 10.1016/j.actaastro.2013.01.022.

[95] J. Yim *et al.*, "1 AAS 04-257 autonomous orbit determination for two spacecraft from relative position measurements," 2004.

[96] Y. Luo *et al.*, "Observability Analysis and Improvement Approach for Cooperative Optical Orbit Determination," en, *Aerospace*, vol. 9, no. 3, p. 166, Mar. 2022, ISSN: 2226-4310. DOI: 10.3390/aerospace9030166.

[97] X. Zhou *et al.*, "Observability analysis of cooperative orbit determination using inertial inter-spacecraft angle measurements," *Acta Astronautica*, vol. 210, pp. 289–302, Sep. 2023, ISSN: 0094-5765. DOI: 10.1016/j.actaastro.2023.05.019.

[98] J. Kruger *et al.*, "Observability analysis and optimization for angles-only navigation of distributed space systems," *Advances in Space Research*, Sep. 2023, ISSN: 0273-1177. DOI: 10.1016/j.asr.2023.08.055.

[99] M. L. Psiaki, "Absolute Orbit and Gravity Determination Using Relative Position Measurements Between Two Satellites," *Journal of Guidance, Control, and Dynamics*, vol. 34, no. 5, pp. 1285–1297, Sep. 2011, ISSN: 0731-5090. DOI: 10.2514/1.47560.

[100] J. A. Christian, "Relative Navigation Using Only Intersatellite Range Measurements," en, *Journal of Spacecraft and Rockets*, vol. 54, no. 1, pp. 13–28, Jan. 2017, ISSN: 0022-4650, 1533-6794. DOI: 10.2514/1.A33608.

[101] C. Ott *et al.*, "Range Biases, Measurement Noise, and Perilune Accuracy in Near Rectilinear Halo Orbit Navigation," Jan. 2022. DOI: 10.2514/6.2022-0999.

[102] M. Shirobokov *et al.*, "Survey of Station-Keeping Techniques for Libration Point Orbits," *Journal of Guidance, Control, and Dynamics*, vol. 40, no. 5, pp. 1085–1105, 2017, ISSN: 0731-5090. DOI: 10.2514/1.G001850.

[103] K. C. Howell *et al.*, "Station-keeping method for libration point trajectories," *Journal of Guidance, Control, and Dynamics*, vol. 16, no. 1, pp. 151–159, Jan. 1993, ISSN: 0731-5090. DOI: 10.2514/3.11440.

[104] X. Fu *et al.*, "Stochastic optimization for stationkeeping of periodic orbits using a high-order Target Point Approach," en, *Advances in Space Research*, vol. 70, no. 1, pp. 96–111, Jul. 2022, ISSN: 0273-1177. DOI: 10.1016/j.asr.2022.04.039.

[105] K. Howell *et al.*, "Aas 98-168 Station-Keeping Strategies For Translunar Libration Point Orbits," Apr. 1999.

[106] Y. Luo *et al.*, "A review of uncertainty propagation in orbital mechanics," *Progress in Aerospace Sciences*, vol. 89, pp. 23–39, Feb. 2017, ADS Bibcode: 2017PrAeS..89...23L, ISSN: 0376-0421. DOI: 10.1016/j.paerosci.2016.12.002.

[107] A. Nugmanov *et al.*, "Computer Simulation of Station Keeping Costs of Halo Orbits in Sun-Earth system," en, *Journal of Physics: Conference Series*, vol. 1740, no. 1, p. 012 020, Jan. 2021, ISSN: 1742-6596. DOI: 10.1088/1742-6596/1740/1/012020.

[108] R. W. Farquhar *et al.*, "Quasi-periodic orbits about the translunar libration point," en, *Celestial mechanics*, vol. 7, no. 4, pp. 458–473, Jun. 1973, ISSN: 1572-9478. DOI: 10.1007/BF01227511.

[109] E. Geipel, "Halo orbit determination, integration, and station keeping," Apr. 2019.

[110] F. O. Hoffman *et al.*, "Propagation of Uncertainty in Risk Assessments: The Need to Distinguish Between Uncertainty Due to Lack of Knowledge and Uncertainty Due to Variability," en, *Risk Analysis*, vol. 14, no. 5, pp. 707–712, 1994, ISSN: 1539-6924. DOI: 10.1111/j.1539-6924.1994.tb00281.x.

[111] S. K. Flegel *et al.*, "State Uncertainty Normality Detection," en, *The Journal of the Astronautical Sciences*, vol. 67, no. 3, pp. 1044–1062, Sep. 2020, ISSN: 2195-0571. DOI: 10.1007/s40295-019-00201-3.

[112] D. K. Geller, "Linear Covariance Techniques for Orbital Rendezvous Analysis and Autonomous Onboard Mission Planning," *Journal of Guidance, Control, and Dynamics*, vol. 29, no. 6, pp. 1404–1414, Nov. 2006, ISSN: 0731-5090. DOI: 10.2514/1.19447.

[113] D. K. Geller *et al.*, "Event Triggers in Linear Covariance Analysis with Applications to Orbital Rendezvous," *Journal of Guidance, Control, and Dynamics*, vol. 32, no. 1, pp. 102–111, Jan. 2009, ISSN: 0731-5090. DOI: 10.2514/1.36834.

[114] C. McLeod, "Effect of nonlinearities on orbit covariance propagation," M.S. thesis, Naval Postgraduate School, Sep. 2013.

[115] R. S. Park *et al.*, "Nonlinear Semi-Analytic Methods for Trajectory Estimation," *Journal of Guidance, Control, and Dynamics*, vol. 30, no. 6, pp. 1668–1676, Nov. 2007, ISSN: 0731-5090. DOI: 10.2514/1.29106.

[116] Z. Yang *et al.*, "Nonlinear Analytical Uncertainty Propagation for Relative Motion near J2-Perturbed Elliptic Orbits," en, *Journal of Guidance, Control, and Dynamics*, vol. 41, no. 4, pp. 888–903, Apr. 2018, ISSN: 0731-5090, 1533-3884. DOI: 10.2514/1.G003071.

[117] Z. Yang *et al.*, "Nonlinear semi-analytical uncertainty propagation of trajectory under impulsive maneuvers," en, *Astrodynamics*, vol. 3, no. 1, pp. 61–77, Mar. 2019, ISSN: 2522-0098. DOI: 10.1007/s42064-018-0036-7.

[118] S. Boone *et al.*, "Orbital Guidance Using Higher-Order State Transition Tensors," *Journal of Guidance, Control, and Dynamics*, vol. 44, no. 3, pp. 493–504, Mar. 2021, ISSN: 0731-5090. DOI: 10.2514/1.G005493.

[119] S. Boone *et al.*, "Directional State Transition Tensors for Capturing Dominant Nonlinear Effects in Orbital Dynamics," *Journal of Guidance, Control, and Dynamics*, vol. 46, no. 3, pp. 431–442, 2023, ISSN: 0731-5090. DOI: 10.2514/1.G006910.

[120] M. Mahooti, *JPL Development Ephemerides (DE405)_MATLAB code*. Nov. 2020. DOI: 10.13140/RG.2.2.24955.95520.

[121] M. Scotti *et al.*, "NaviMoon-Ultra-High Sensitivity GNSS Receiver for Lunar Navigation," *NAVITEC 2022*, vol. 1, 2022.

[122] D. Stiller, "Short-term orbital effects of radiation pressure on the Lunar Reconnaissance Orbiter," en, 2023.

[123] R. Floberghagen *et al.*, "Lunar albedo force modeling and its effect on low lunar orbit and gravity field determination," en-US, *Advances in Space Research*, vol. 23, no. 4, pp. 733–738, Jan. 1999, ISSN: 0273-1177. DOI: 10.1016/S0273-1177(99)00155-6.

[124] R. Jain *et al.*, "Inter-satellite tracking methods and applications: A comprehensive survey," *Advances in Space Research*, vol. 74, no. 8, pp. 3877–3901, Oct. 2024, ISSN: 0273-1177. DOI: 10.1016/j.asr.2024.08.022.

[125] C. Duncan *et al.*, "Low Mass Radio Science Transponder - Satellite TRL Raising Mission for LMRST Solar System Navigation and Radio Science," NTRS Author Affiliations: Jet Propulsion Lab., California Inst. of Tech. NTRS Document ID: 20150004591 NTRS Research Center: Jet Propulsion Laboratory (JPL), Jet Propulsion Laboratory, California Institute of Technology, Pasadena, California, Aug. 2012.

[126] M. Lombardo *et al.*, "Design and Analysis of the Cis-Lunar Navigation for the ArgoMoon CubeSat Mission," en, *Aerospace*, vol. 9, no. 11, p. 659, Nov. 2022, ISSN: 2226-4310. DOI: 10.3390/aerospace9110659.

[127] F. Gao *et al.*, "Implementing the Nelder-Mead simplex algorithm with adaptive parameters," en, *Computational Optimization and Applications*, vol. 51, no. 1, pp. 259–277, Jan. 2012, ISSN: 1573-2894. DOI: 10.1007/s10589-010-9329-3.

[128] S. Takenaga *et al.*, "Practical initialization of the Nelder–Mead method for computationally expensive optimization problems," en, *Optimization Letters*, vol. 17, no. 2, pp. 283–297, Mar. 2023, ISSN: 1862-4480. DOI: 10.1007/s11590-022-01953-y.

[129] L. Han *et al.*, "Effect of dimensionality on the Nelder–Mead simplex method," *Optimization Methods and Software*, vol. 21, no. 1, pp. 1–16, Feb. 2006, ISSN: 1055-6788. DOI: 10.1080/10556780512331318290.

[130] ClydeSpace, *SMALLSAT SIRIUS-OBC-LEON3FT - Satellite Command & Data Handling | AAC Clyde Space*, en-GB.

[131] IMT, *X-band transponder*, en-gb.

[132] K. Das, "A Brief Review of Tests for Normality," *American Journal of Theoretical and Applied Statistics*, vol. 5, p. 5, Jan. 2016. DOI: 10.11648/j.ajtas.20160501.12.

[133] NanoAvionics, *Cubesat propulsion system epss | nanoavionics*, https://nanoavionics.com/cubesat-components/cubesat-propulsion-system-epss/, [Accessed 19-06-2024].

[134] SatSearch, *1n hpgp thruster | satsearch*, https://satsearch.co/products/ecaps-1n-hpgp-thruster, [Accessed 19-06-2024].

A

Simulation details

	E	M	S	Me	V	Ma	J	S	U	N
Low Fidelity (LF)										
CRTBP	*	*								
High Fidelity (HF)										
Point Mass (PM)										
1	*	*	*							
2	*	*	*	*						
3	*	*	*	*	*					
4	*	*	*	*	*	*				
5	*	*	*	*	*	*	*			
6	*	*	*	*	*	*	*	*		
7	*	*	*	*	*	*	*	*	*	
8	*	*	*	*	*	*	*	*	*	*
Point Mass SRP (PMSRP)										
1	*	*	*^							
2	*	*	*^	*						
3	*	*	*^	*	*					
4	*	*	*^	*	*	*				
5	*	*	*^	*	*	*	*			
6	*	*	*^	*	*	*	*	*		
7	*	*	*^	*	*	*	*	*	*	
8	*	*	*^	*	*	*	*	*	*	*
Spherical Harmonics (SH)										
1	(2,2)	(2,2)	*							
2	(2,2)	(5,5)	*	*						
3	(2,2)	(10,10)	*	*	*					
4	(2,2)	(20,20)	*	*	*	*				
5	(5,5)	(2,2)	*	*	*	*	*			
6	(5,5)	(5,5)	*	*	*	*	*	*		
7	(5,5)	(10,10)	*	*	*	*	*	*	*	
8	(5,5)	(20,20)	*	*	*	*	*	*	*	*
Spherical Harmonics SRP (SHSRP)										
1	(2,2)	(2,2)	*^							
2	(2,2)	(5,5)	*^	*						
3	(2,2)	(10,10)	*^	*	*					
4	(2,2)	(20,20)	*^	*	*	*				
5	(5,5)	(2,2)	*^	*	*	*	*			
6	(5,5)	(5,5)	*^	*	*	*	*	*		
7	(5,5)	(10,10)	*^	*	*	*	*	*	*	
8	(5,5)	(20,20)	*^	*	*	*	*	*	*	*
Full Fidelity (FF)										
Full Fidelity (FF)	(20,20)^+	(20,20)^+	*^+	*+	*+	*+	*+	*+	*+	*+

Clarifications
1. bodies = ”Earth”, ”Moon”, ”Sun”, ”Mercury”, ”Venus”, ”Mars”, ”Jupiter”, ”Saturn”, ”Uranus”, ”Neptune”
2. ”(n, m)” = order, m= degrees, ”*” = point mass, ”^” = radiation pressure, ”+” = relativistic correction

Table A.1: Acceleration terms used in each dynamic model

Parameter	Details		Unit
Dynamic model			
	Initial states		
Initial epoch	60390		MJD
States	See Table 4.1 and Table 4.2		
	Satellite properties		
	LPF	*LUMIO*	
Mass	280	22.8	kg
Effective area	3.0	0.41	m^2
Reflectivity	1.8	1.08	$-$
	Environment properties		
Gravitational parameter	$6.6726 \cdot 10^{-11}$		m^3/s^2
Mass Primaries	$5.9737 \cdot 10^{24}$	$7.3477 \cdot 10^{22}$	kg
Solar radiation	Occultation shadow:	Conical	
	Body approximation:	Connonball	
Integration	Type:	Runge-Kutta-Fehlberg 45	
	Relative tolerance	$1 \cdot 10^{-10}$	$-$
	Absolute tolerance	$1 \cdot 10^{-10}$	$-$
	Initial step	10	s
	Reference frames		
Inertial frame	ECI J2000		
Ephemerides	JPL DE405		
Time scales	IAU 2006		
Measurement model			
Observable	Type:	Two-way range	
	Noise:	2.98 1σ	m
	Bias:	0	m
	Observation interval	300	s
Estimation model			
Type	Batch Least Squares		
Initial estimation error	*LPF*	*LUMIO*	
Position	500	500	m
Velocity	1	1	mm/s
Initial estimation uncertainty			
Position	500 1σ	500 1σ	m
Velocity	1 1σ	1 1σ	mm/s
Convergence threshold	10 iterations per arc		-
Correction model			
Type	Target Point Method		
Target points	1: 3 days after cut-off epoch		$days$
Navigation model			
Correction threshold	0.00		m/s
Correction error	Magnitude:	0.00	%
	Direction:	0.00	%
Insertion error	*LPF*	*LUMIO*	
Position	0	0	m
Velocity	0	0	m/s
Duration		28	$days$
Observation window	See Table 4.3		
Optimization model			
Problem scheme	See Equation 4.2		

Table A.2: Overview of the default simulation settings

B

Navigation model flowchart

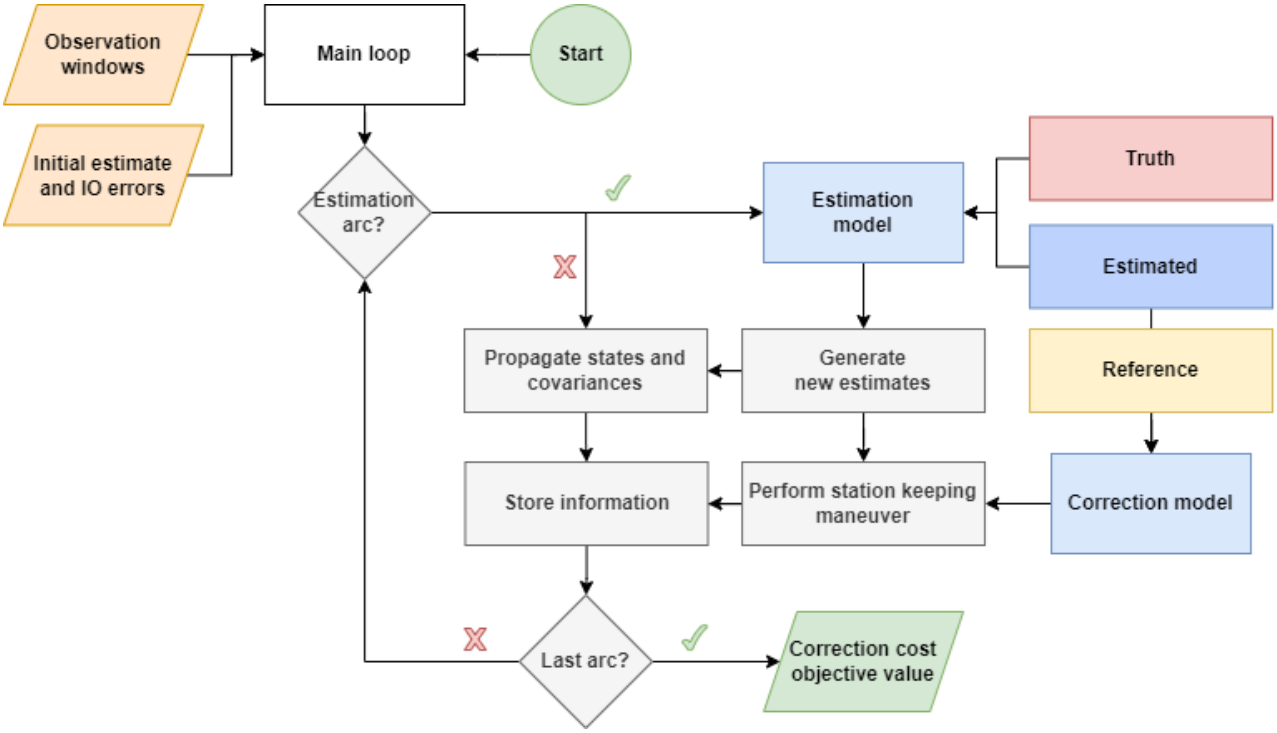

Figure B.1: Schematic overview of the navigation model

C

Optimization Analysis

C.1. Tables of optimization cases

This section shows the values of the design vectors for the results of the optimization cases discussed in Section 5.4 and relates it to the annual ΔV and the average power that is expected for different subsystems related to the orbit determination and correction process. Note how the power levels for the OBC and thrusters are the same. The OBC always runs regardless whether tracking is done and the thrusters are heated equally as long for each solution because each solution has the same amount of tracking arcs.

C.1.1. Nelder-Mead, 28 days, PMSRP dynamic model

	Vectors					
Entry	**Initial**	**Run 1**	**Run 2**	**Run 3**	**Run 4**	**Run 5**
T_1	1.0000	0.9511	1.1345	1.0946	0.8733	1.1723
T_2	1.0000	1.0720	1.0132	0.9875	1.0593	1.0220
T_3	1.0000	0.9158	0.8966	0.9829	0.8653	0.8877
T_4	1.0000	0.9177	0.8085	0.7866	1.0651	1.1066
T_5	1.0000	0.9962	0.9344	0.9975	0.9283	0.8476
T_6	1.0000	0.9676	0.8889	0.9436	0.9750	0.8476
T_7	1.0000	0.7406	0.8332	0.7297	0.6613	0.7150
Annual ΔV (m/s)	0.6116	0.4276	0.4224	0.4221	0.4236	0.4339
% Change	00.00%	-30.08%	-30.93%	-30.99%	-30.74%	-29.05%
Tracking time (days)	7.0000	6.5609	6.5093	6.5223	6.4277	6.5989
% Change	00.00%	-6.27%	-7.01%	-6.82%	-8.18%	-5.73%
Average Power (W)	11.8015	11.6200	11.5987	11.6040	11.5649	11.6357
Transponder	10.2931	10.1116	10.0903	10.0957	10.0566	10.1273
Thruster	0.2083	0.2083	0.2083	0.2083	0.2083	0.2083
OBC	1.3000	1.3000	1.3000	1.3000	1.3000	1.3000
% Change	00.00%	-1.54%	-1.72%	-1.67%	-2.00%	-1.40%

Table C.1: Design vector entries

C.1.2. PSO, 28 days, PMSRP dynamic model

	Vectors					
Entry	**Initial**	**Run 1**	**Run 2**	**Run 3**	**Run 4**	**Run 5**
T_1	1.0000	0.7622	1.6186	0.5423	0.5804	0.9492
T_2	1.0000	1.1677	1.1374	0.9218	1.9610	1.7369
T_3	1.0000	0.8522	1.1665	1.4092	0.1151	0.2163
T_4	1.0000	1.0477	0.1000	0.9373	1.1529	0.9822
T_5	1.0000	1.8572	0.2270	0.8899	0.9638	0.1000
T_6	1.0000	0.1000	0.1000	0.1000	0.1000	0.1000
T_7	1.0000	0.1000	0.1000	0.4454	0.1000	0.1000
Annual ΔV (m/s)	0.6116	0.3213	0.2802	0.3214	0.2959	0.2999
% Change	00.00%	-47.46%	-54.18%	-47.45%	-51.62%	-50.97%
Tracking time (days)	7.0000	5.8870	4.4495	5.2459	4.9732	4.1847
% Change	00.00%	-15.90%	-36.44%	-25.06%	-28.95%	-40.22%
Average Power (W)	11.8015	11.3415	10.7473	11.0765	10.9638	10.6379
Transponder	10.2931	9.8331	9.2390	9.5682	9.4554	9.1296
Thruster	0.2083	0.2083	0.2083	0.2083	0.2083	0.2083
OBC	1.3000	1.3000	1.3000	1.3000	1.3000	1.3000
% Change	00.00%	-3.90%	-8.93%	-6.14%	-7.10%	-9.86%

Table C.2: Design vector entries

C.1.3. PSO, 28 days, SHSRP dynamic model

	Vectors					
Entry	**Initial**	**Run 1**	**Run 2**	**Run 3**	**Run 4**	**Run 5**
T_1	1.0000	0.6891	1.4729	1.0528	0.1000	1.4739
T_2	1.0000	1.0073	0.8399	0.8927	2.0000	2.0000
T_3	1.0000	0.9859	1.0549	1.1197	0.6739	0.3100
T_4	1.0000	1.1129	0.4307	0.7432	1.0211	0.2390
T_5	1.0000	1.6191	0.2040	0.9713	0.2205	1.0334
T_6	1.0000	0.5653	0.1000	0.2371	0.1000	0.1000
T_7	1.0000	0.1000	0.1000	0.4378	0.1000	0.2643
Annual ΔV (m/s)	0.6188	0.3485	0.2805	0.3165	0.2880	0.3024
% Change	00.00%	-43.69%	-54.67%	-48.86%	-53.46%	-51.13%
Tracking time (days)	7.0000	6.0794	4.2024	5.4546	4.2155	5.4205
% Change	00.00%	-13.15%	-39.97%	-22.08%	-39.78%	-22.56%
Average Power (W)	11.8015	11.4210	10.6452	11.1627	10.6506	11.1487
Transponder	10.2931	9.9127	9.1369	9.6544	9.1423	9.6403
Thruster	0.2083	0.2083	0.2083	0.2083	0.2083	0.2083
OBC	1.3000	1.3000	1.3000	1.3000	1.3000	1.3000
% Change	00.00%	-3.22%	-9.80%	-5.41%	-9.75%	-5.53%

Table C.3: Design vector entries

C.1.4. PSO, 56 days, PMSRP dynamic model

	Vectors					
Entry	**Initial**	**Run 1**	**Run 2**	**Run 3**	**Run 4**	**Run 5**
T_1	1.0000	1.0407	1.4203	0.8645	0.3859	0.7746
T_2	1.0000	1.1549	0.3999	1.4020	0.2920	0.7179
T_3	1.0000	1.4806	1.5037	1.1470	0.4261	0.8281
T_4	1.0000	0.5078	0.8653	0.4119	0.2024	1.5631
T_5	1.0000	1.1531	0.8420	1.2009	2.0000	0.3545
T_6	1.0000	0.7169	0.7000	0.6339	0.9404	0.9205
T_7	1.0000	1.1428	1.4782	0.8037	1.2448	1.1469
T_8	1.0000	0.7111	1.4704	0.9455	1.5680	0.5908
T_9	1.0000	1.1313	0.9193	0.9280	0.7594	0.4945
T_{10}	1.0000	0.9630	0.5479	0.1000	0.1728	0.7633
T_{11}	1.0000	0.8079	0.6880	0.1000	0.8315	1.5876
T_{12}	1.0000	0.8721	0.8708	1.2233	1.9213	1.3096
T_{13}	1.0000	0.9203	0.1922	0.1000	0.1964	0.3839
T_{14}	1.0000	0.1090	0.6562	1.4338	1.0203	0.3595
Annual ΔV (m/s)	0.6240	0.4513	0.4352	0.4168	0.5050	0.4383
% Change	00.00%	-27.67%	-30.26%	-33.20%	-19.08%	-29.76%
Tracking time (days)	14.0000	12.7115	12.5545	11.2946	11.9611	11.7950
% Change	00.00%	-9.20%	-10.33%	-19.32%	-14.56%	-15.75%
Average Power (W)	11.8015	11.5352	11.5027	11.2424	11.3801	11.3458
Transponder	10.2931	10.0269	9.9944	9.7341	9.8718	9.8375
Thruster	0.2083	0.2083	0.2083	0.2083	0.2083	0.2083
OBC	1.3000	1.3000	1.3000	1.3000	1.3000	1.3000
% Change	00.00%	-2.26%	-2.53%	-4.74%	-3.57%	-3.86%

Table C.4: Design vector entries

C.1.5. PSO, 28 days, PMSRP dynamic model, with 0.003 m/s threshold

	Vectors					
Entry	**Initial**	**Run 1**	**Run 2**	**Run 3**	**Run 4**	**Run 5**
T_1	1.0000	1.1318	2.0000	0.7237	0.1861	1.2050
T_2	1.0000	1.1813	0.8856	0.5581	0.8009	1.5947
T_3	1.0000	0.6829	2.0000	0.2861	0.5644	0.7294
T_4	1.0000	0.8296	0.3362	0.2731	0.1000	0.7364
T_5	1.0000	1.2968	0.6273	0.1913	0.5694	0.5851
T_6	1.0000	0.3224	0.1000	0.1380	0.4906	0.8648
T_7	1.0000	0.4605	0.1719	0.1789	0.9860	0.2442
Annual ΔV (m/s)	0.6121	0.3263	0.1820	0.0000	0.1202	0.2802
% Change	00.00%	-46.68%	-70.26%	-100.00%	-80.37%	-54.23%
Tracking time (days)	7.0000	5.9053	6.1210	2.3492	3.6975	5.9596
% Change	00.00%	-15.64%	-12.56%	-66.44%	-47.18%	-14.86%
Average Power (W)	11.8015	11.3490	11.4382	9.8793	10.4365	11.3715
Transponder	10.2931	9.8407	9.9298	8.3709	8.9282	9.8631
Thruster	0.2083	0.2083	0.2083	0.2083	0.2083	0.2083
OBC	1.3000	1.3000	1.3000	1.3000	1.3000	1.3000
% Change	00.00%	-3.83%	-3.08%	-16.29%	-11.57%	-3.64%

Table C.5: Design vector entries

C.1.6. PSO, 56 days, PMSRP dynamic model, with 0.003 m/s threshold

	Vectors					
Entry	**Initial**	**Run 1**	**Run 2**	**Run 3**	**Run 4**	**Run 5**
T_1	1.0000	0.8567	1.3308	1.8853	0.5168	1.0644
T_2	1.0000	0.7090	0.4349	0.1961	0.6077	0.5539
T_3	1.0000	2.0000	1.5158	1.3062	0.7254	0.1614
T_4	1.0000	0.3168	0.9154	0.6350	0.3407	0.7213
T_5	1.0000	0.7282	0.9440	0.1000	1.7640	1.1188
T_6	1.0000	0.1000	0.6867	0.1000	0.8346	0.4984
T_7	1.0000	1.2493	1.3668	0.4053	1.0320	1.3044
T_8	1.0000	0.9531	1.3191	2.0000	1.5341	1.1961
T_9	1.0000	1.0619	0.8873	0.7183	0.7193	1.3817
T_{10}	1.0000	0.2268	0.7297	0.4561	0.3082	0.6049
T_{11}	1.0000	0.6391	0.6956	1.0094	0.8170	0.8980
T_{12}	1.0000	2.0000	0.7861	1.3808	1.0272	0.7105
T_{13}	1.0000	2.0000	0.1000	0.4413	0.6028	0.8803
T_{14}	1.0000	1.1456	0.5829	1.0456	0.8761	0.6273
Annual ΔV (m/s)	0.7621	0.4009	0.3832	0.4026	0.3817	0.3634
% Change	00.00%	-47.39%	-49.71%	-47.17%	-49.92%	-52.32%
Tracking time (days)	14.0000	13.9867	12.2950	11.6795	11.7058	11.7213
% Change	00.00%	-0.10%	-12.18%	-16.57%	-16.39%	-16.28%
Average Power (W)	11.8015	11.7987	11.4491	11.3219	11.3274	11.3306
Transponder	10.2931	10.2904	9.9408	9.8136	9.8190	9.8222
Thruster	0.2083	0.2083	0.2083	0.2083	0.2083	0.2083
OBC	1.3000	1.3000	1.3000	1.3000	1.3000	1.3000
% Change	00.00%	-0.02%	-2.99%	-4.06%	-4.02%	-3.99%

Table C.6: Design vector entries

C.2. Relationship between SKM cost, estimation error and dispersion

This section compares the relationship between SKM cost, estimation error and dispersion for two example cases. Figure 5.33 and Figure C.2 show it for one run of the Nelder-Mead and PSO scenario. However, the exactly values for all 5 runs, as explained in Section 5.4, are show in detail in **??**.

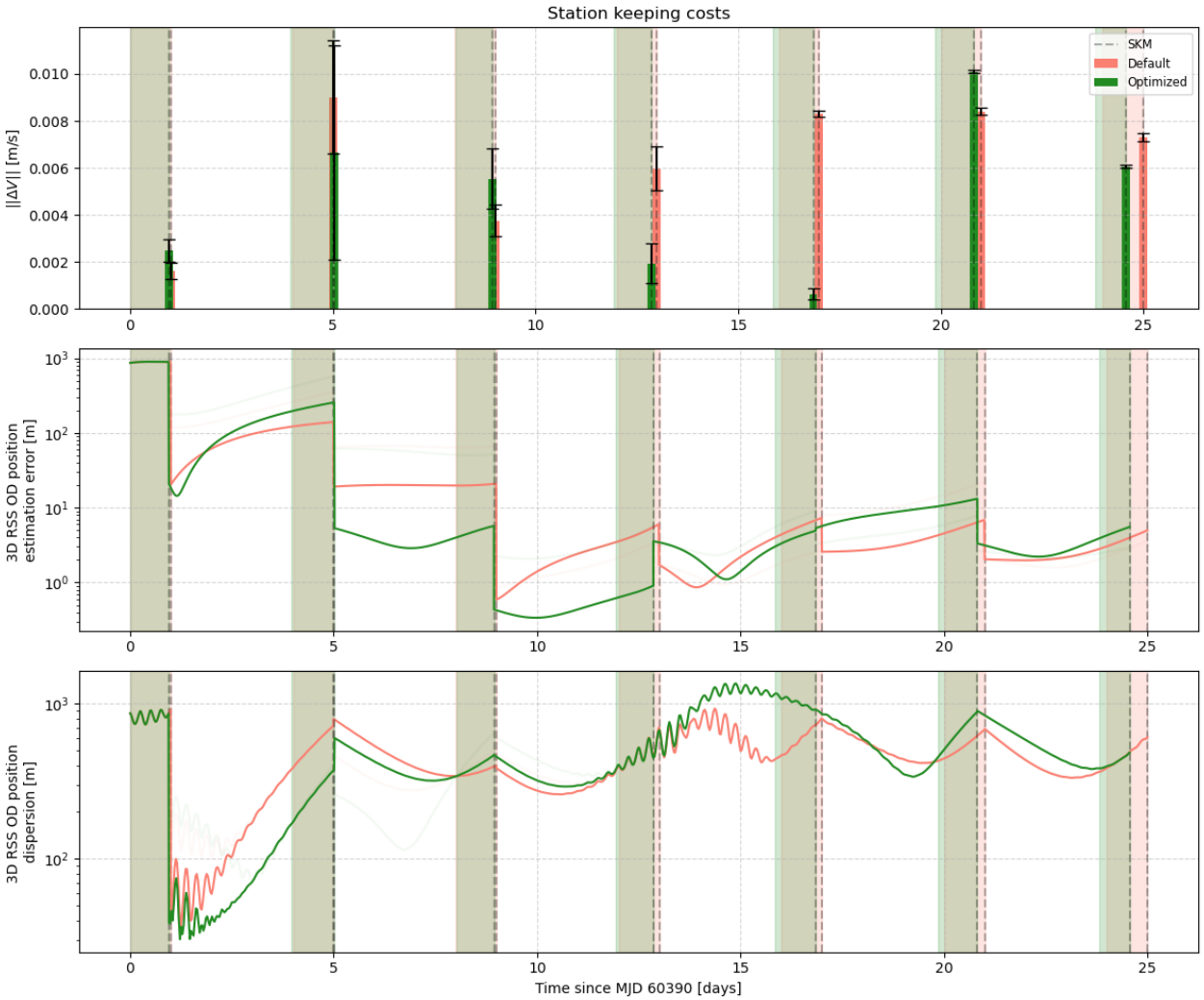

Figure C.1: Default and optimized tracking configuration resulting from the Nelder-Mead optimization method with corresponding contributors to correction costs (28 days, PMSRP, run 1 of 5)

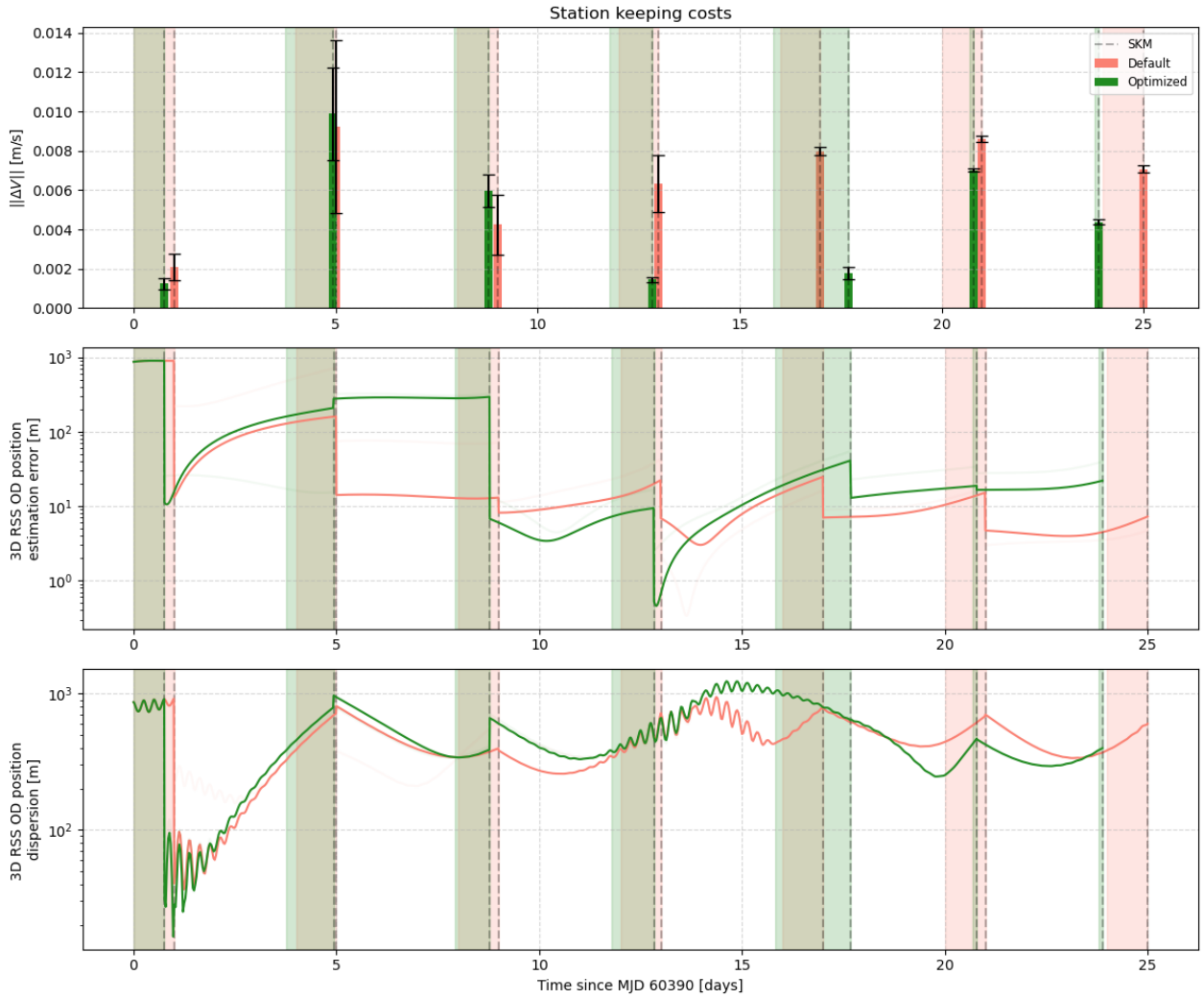

Figure C.2: Default and optimized tracking configuration resulting from the PSO optimization method with corresponding contributors to correction costs (28 days, PMSRP, run 1 of 5)

D

Sensitivity analysis

D.1. Analysis with 28 days simulation

The annual approximation of ΔV associated with a simulation of 28 days, as explained in Section 5.3, are shown in Figure D.1 and Figure D.2.

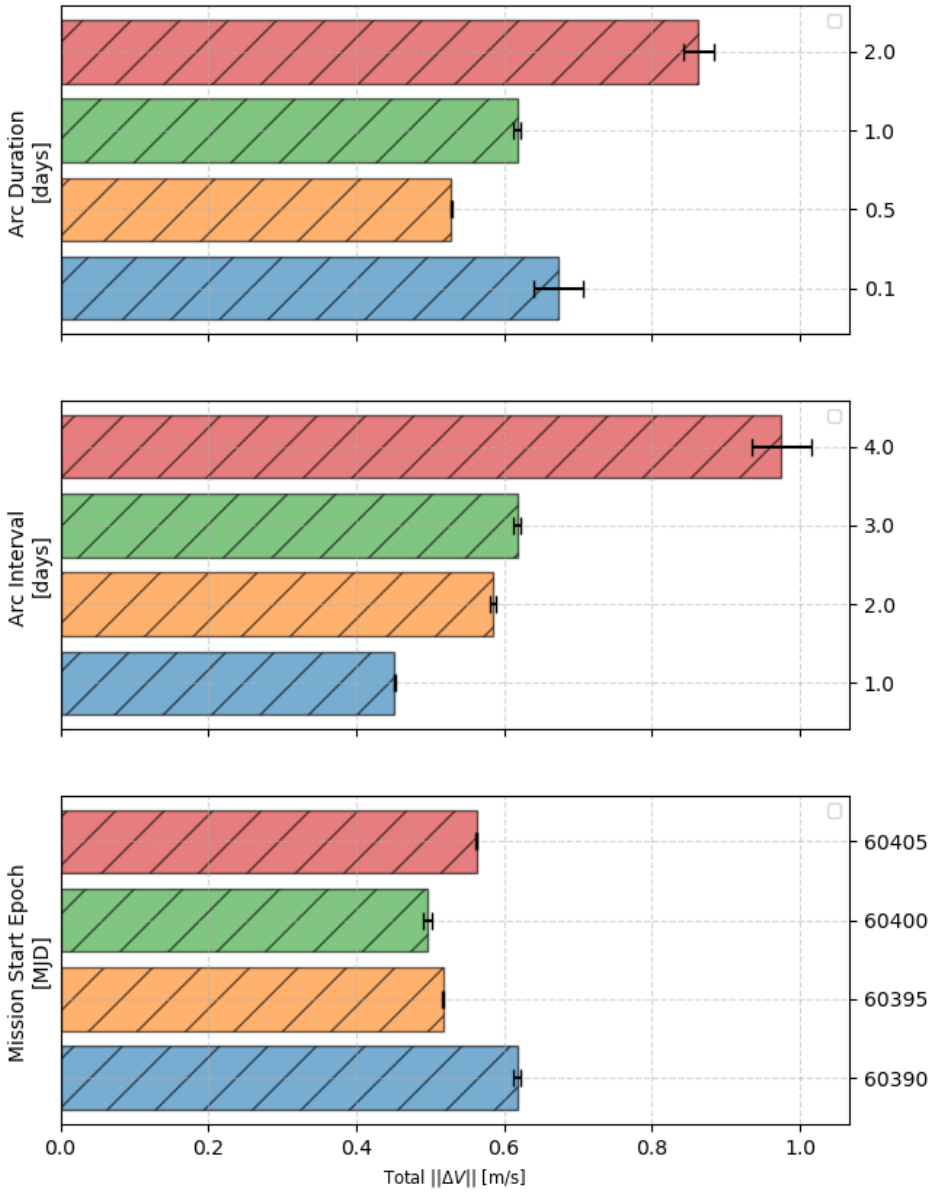

Figure D.1: Annual ΔV for sensitivity analysis results for observation window parameters (28 days)

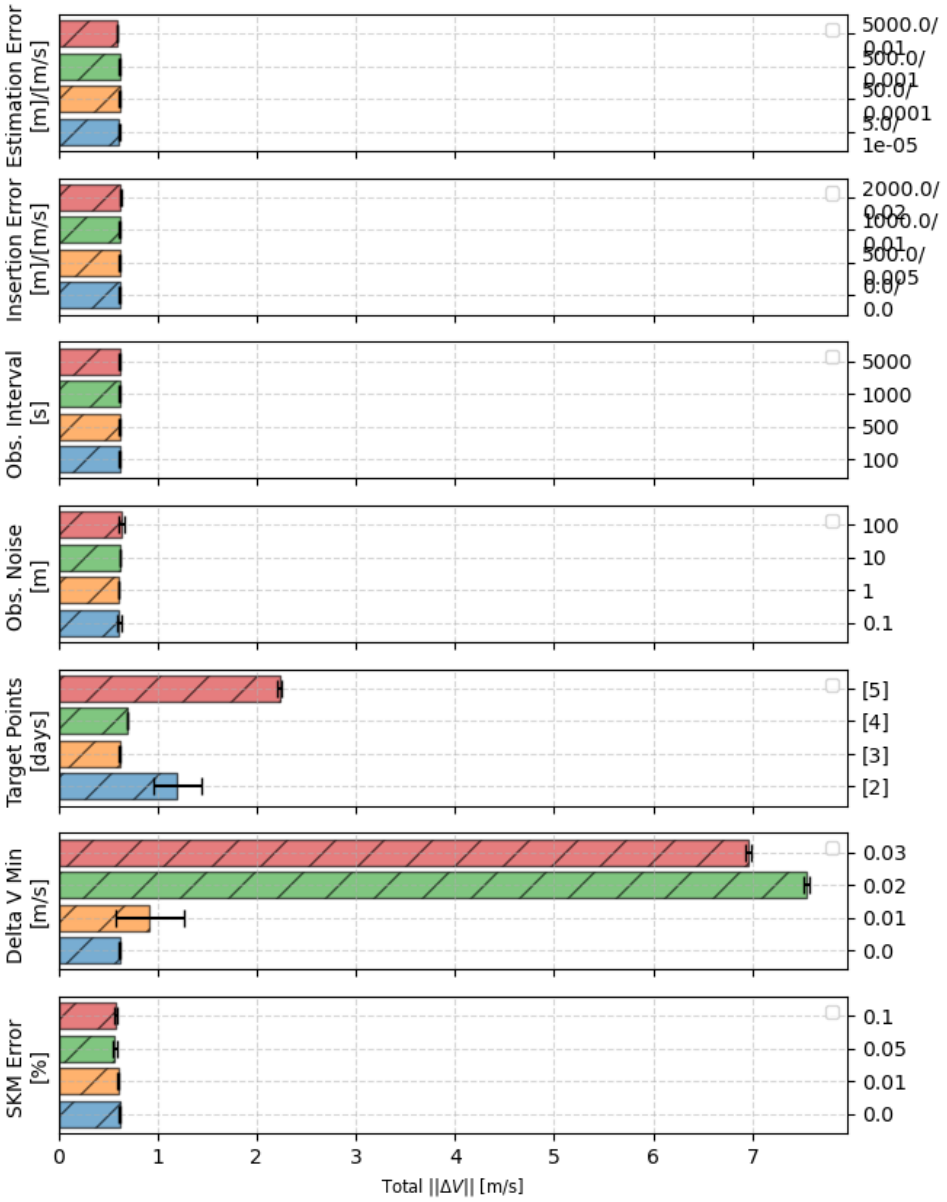

Figure D.2: Annual ΔV for sensitivity analysis results for auxiliary parameters (28 days)

D.2. Analysis with 56 days simulation

Figure D.3 and Figure D.4 show the raw ΔV associated with a simulation of 56 days. The annual approximation using those results are shown in Figure D.5 and Figure D.6.

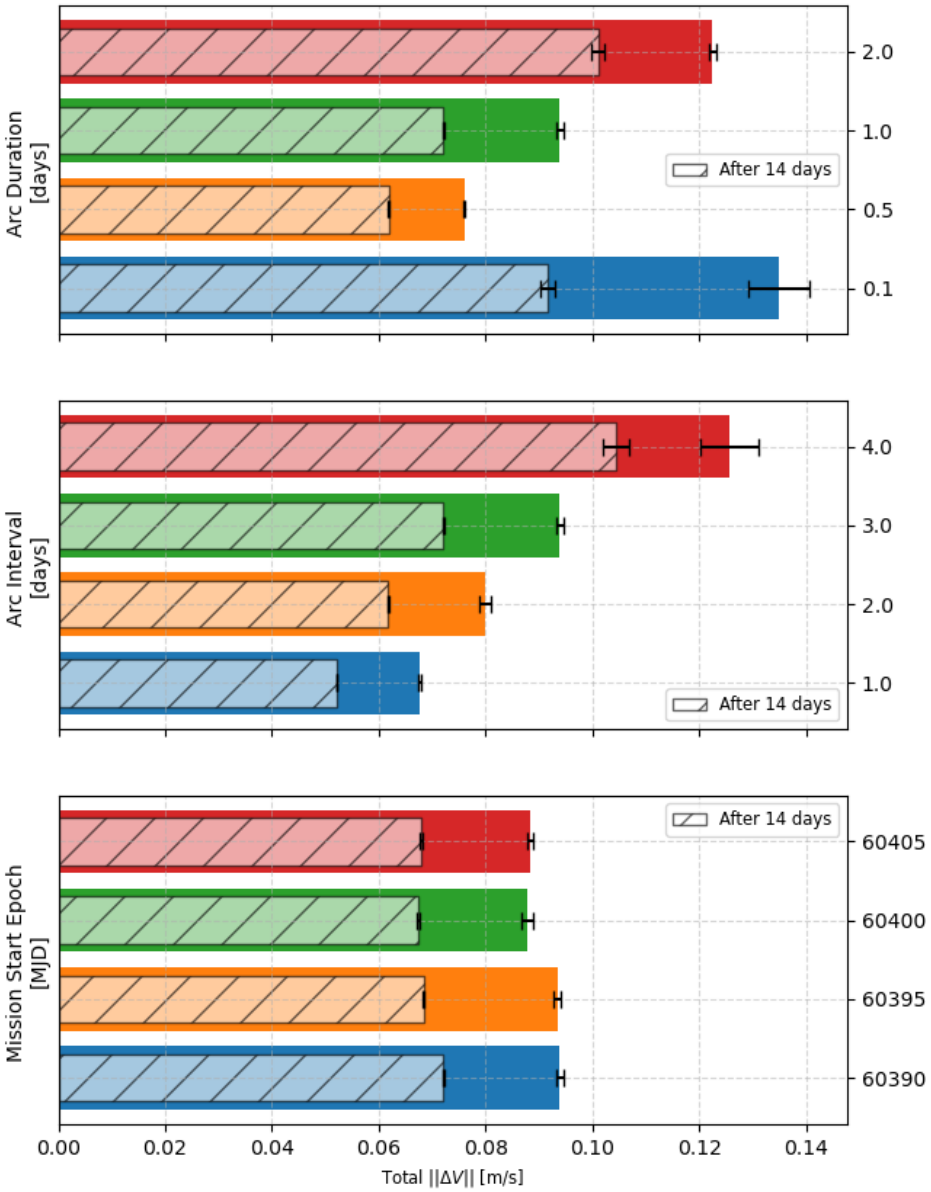

Figure D.3: Sensitivity analysis results for observation window parameters (56 days)

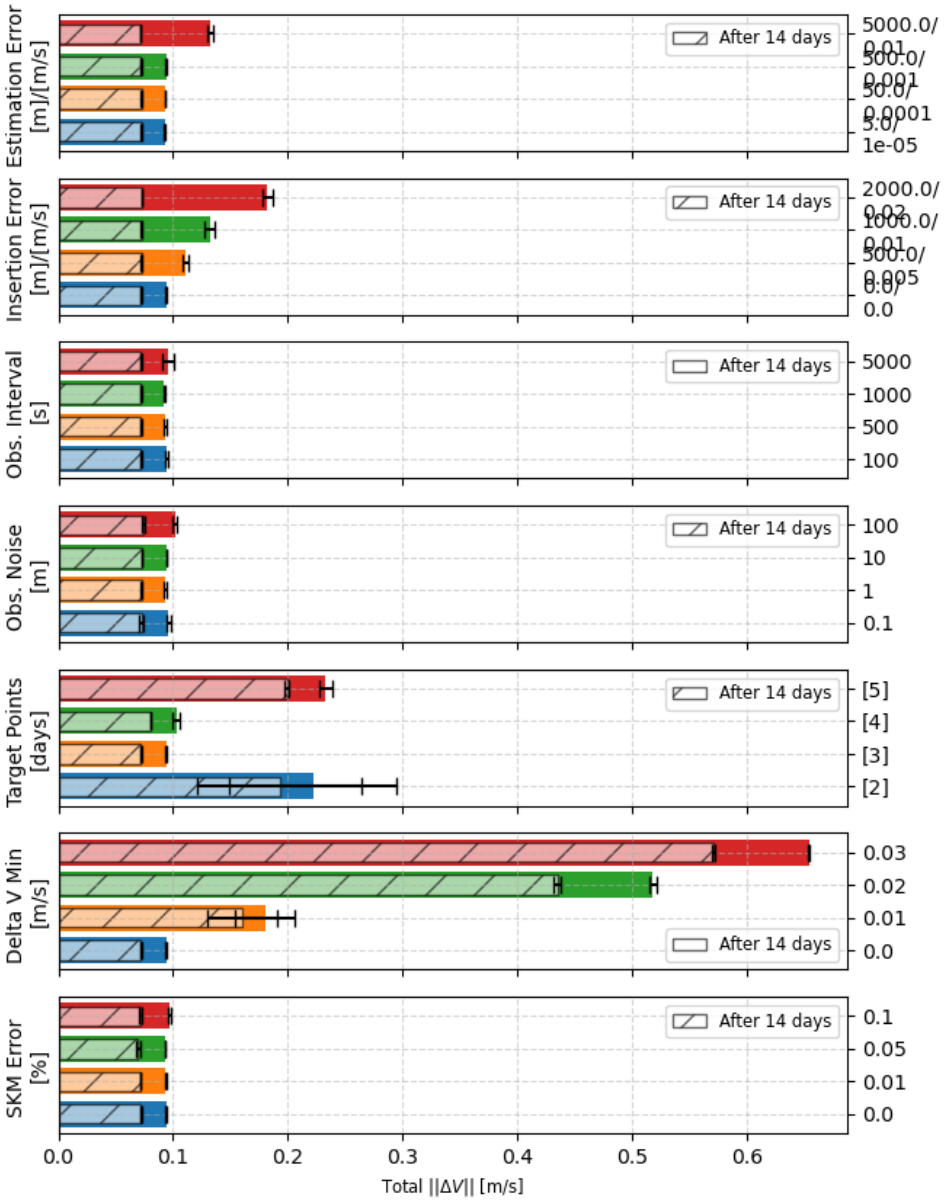

Figure D.4: Sensitivity analysis results for auxiliary parameters (56 days)

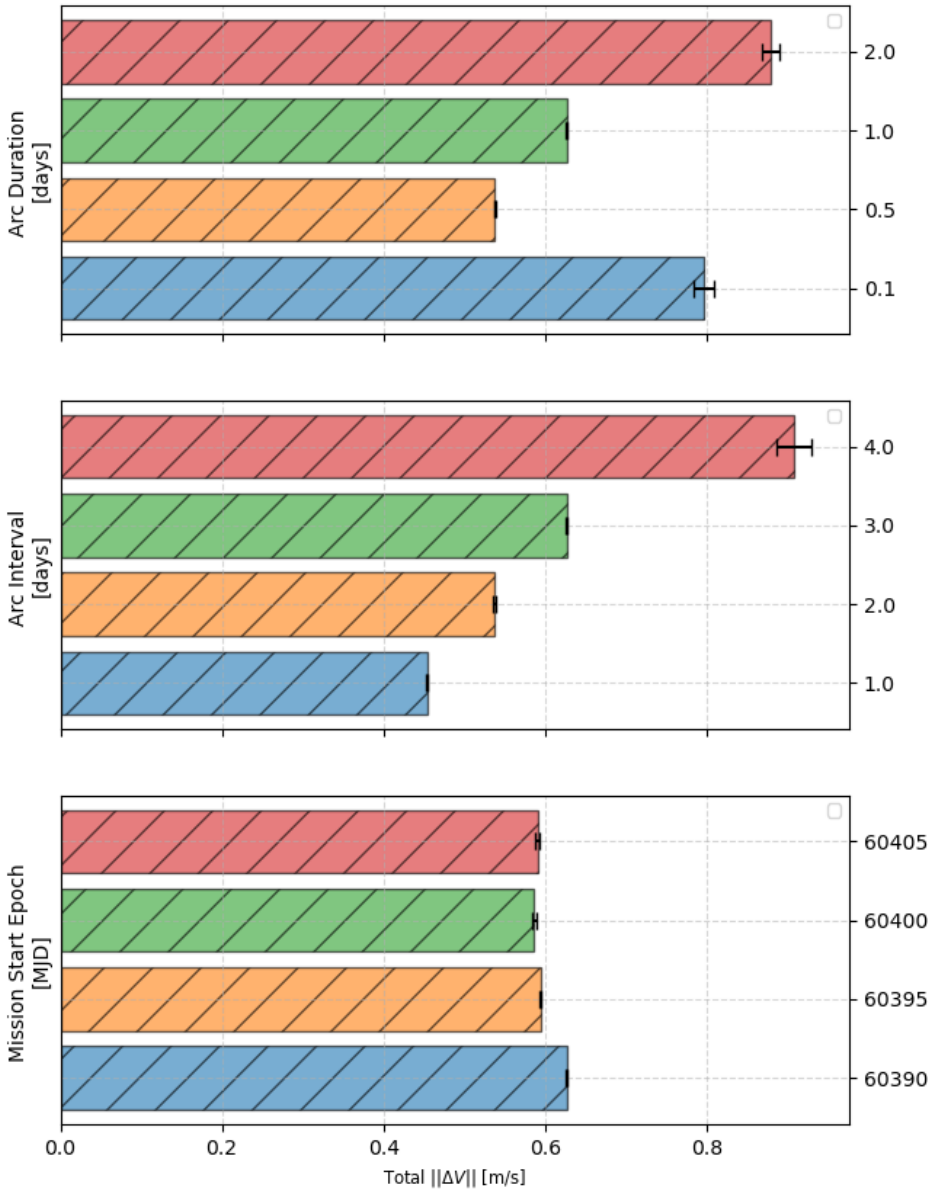

Figure D.5: Annual ΔV for sensitivity analysis results for observation window parameters (56 days)

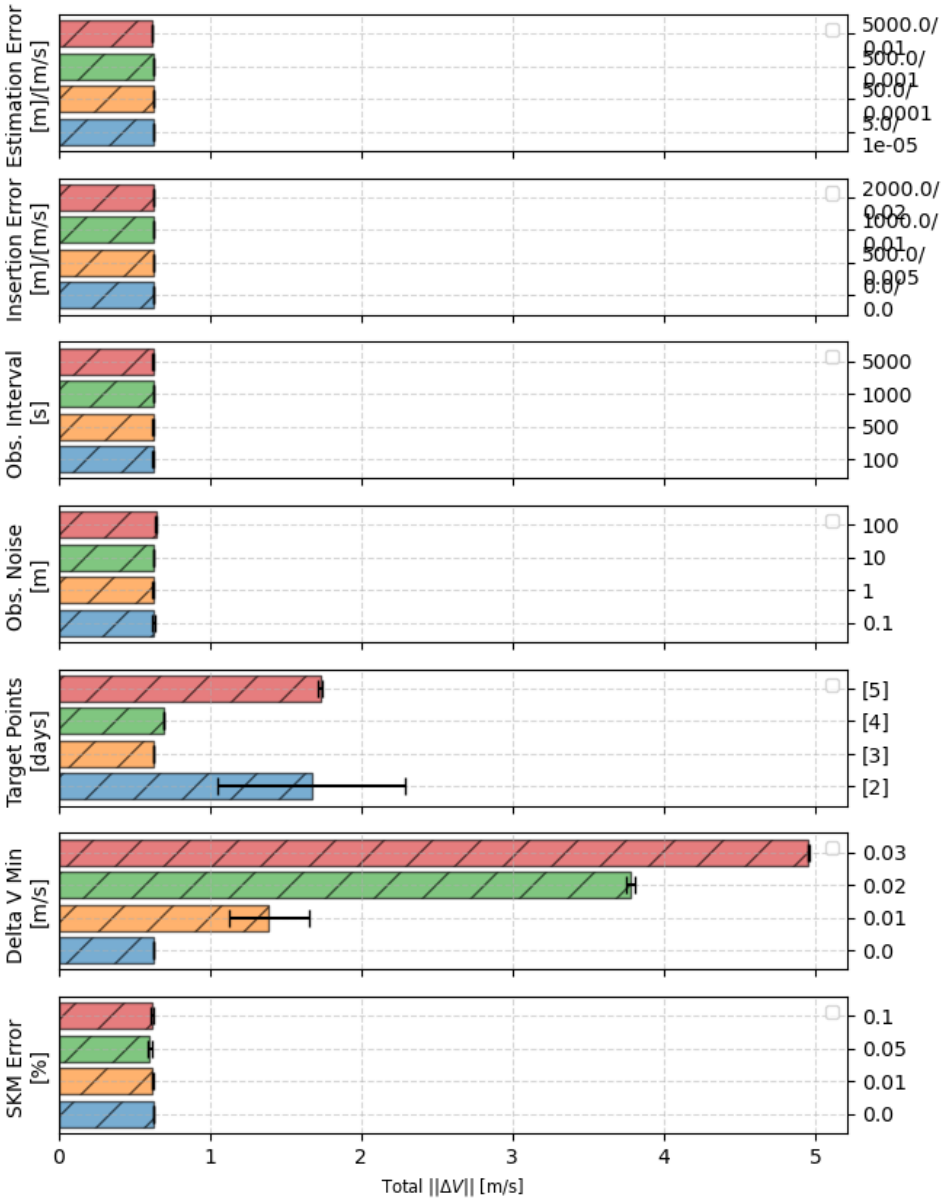

Figure D.6: Annual ΔV for sensitivity analysis results for auxiliary parameters (56 days)